Dissertation zur Erlangung des Doktorgrades

der Fakultät für Chemie und Pharmazie

der Ludwig-Maximilians-Universität München

Investigation of nucleosome remodeling by the chromatin remodeler INO80 with a combination of biochemical and single-molecule approaches

Marianne Ursula Schwarz

aus

München, Deutschland

2018

This thesis has been prepared from January 2013 to June 2018 in the laboratories of Prof. Dr. Karl-Peter Hopfner (Gene Center and Department of Biochemistry, Ludwig-Maximilians-Universität München) and of Prof. Dr. Jens Michaelis (Institute of Biophysics, Ulm University).

TABLE OF CONTENTS

1. Summary

The degree of compaction and the structure of chromatin, the protein-deoxyribonucleic acid (DNA) complex in the nucleus of eukaryotic cells, is vital to regulate the access to DNA by all factors involved in DNA-templated processes. Nucleosomes constitute the smallest packing unit of chromatin (Kornberg, 1974; Luger et al., 1997a) and molecular machines and enzymes that act on nucleosomes are extremely versatile. Amongst them, so-called adenosine triphosphate (ATP)-dependent chromatin remodelers ensure proper nucleosome organization on DNA (Krietenstein et al., 2016; Narlikar et al., 2013).

The present thesis investigates *in vitro* nucleosome remodeling by the multi-subunit chromatin remodeler INO80 from *Saccharomyces cerevisiae* (*Sc*); 'INO80' recalls its identification through inositol auxotroph yeast mutants (Ebbert et al., 1999). So far, only a limited number of mechanistic studies are available for the INO80 complex. This thesis brings together biochemical and single-molecule approaches to advance the current understanding of INO80 mediated catalysis on single nucleosomes. Such insights have been missing, especially in the light of thorough investigations of different chromatin remodeler subfamilies and homologues *in vivo* and *in vitro* during the last decades.

This study establishes a platform for experiments with a minimal functional catalytic system of purified components, that is, the 19 subunit INO80 complex and single nucleosomes, to enable concomitant characterization with well-established *ensemble* biochemical methods and single-molecule Förster resonance energy transfer (smFRET). The first part of this thesis focuses on biochemical approaches to reconstitute homogenous nucleosome samples and to characterize the *Sc*INO80 complex, mostly with respect to effective nucleosome repositioning. I developed these results further to enable smFRET applications that overcome *ensemble* averaging and that provide unprecedented mechanistic insights into the INO80-nucleosome interplay. First, the INO80 complex is a processive enzyme that performs a number of mechano-chemical cycles before releasing the nucleosome. Second, the results presented in this work are in favor of a regulatory impact of histone tails on INO80 nucleosome remodeling. Histone tails constitute terminal extensions of histones with tremendous effects on chromatin organization (Jenuwein and Allis, 2001; Strahl and Allis, 2000). The approaches developed in this thesis are expanded to mutant nucleosome substrates that are lacking all histone tails and that reflect an altered nucleosome recognition step by INO80.

2. Introduction

2.1 Genome organization in the course of evolution

Life is encoded by the genetic blueprint of every cell and organism. All processes of life rely on transcription of the genetic information to RNA by polymerases and subsequent translation of this information to proteins by ribosomes. This is also known as the central dogma of molecular biology, devised in Crick (1958) and in Crick (1970) (Cobb, 2017). As an immediate consequence, cell metabolism and homeostasis fundamentally depend on the accessibility of DNA for factors that regulate transcription. Analogously, accessibility of DNA is a prerequisite for factors that ensure genome integrity (in response to DNA damage) and for factors that accomplish genome replication (prior to cell division). However, genome organization partially counteracts DNA accessibility.

2.1.1 Genome organization in eukaryotes

In eukaryotes, chromosomes are compact structures found in the nucleus of cells. Early studies described interphase nuclei to be composed of decondensed regions of the genome (euchromatin, loose DNA packing) and of regions containing tightly packed DNA (heterochromatin), where DNA condensation is comparable to mitotic cells (Allshire and Madhani, 2018; Heitz, 1928; Straub, 2003; Zacharias, 1995). Much later, the packing of eukaryotic chromatin was suggested to be mediated by its repeating unit that consists of the histone protein octamer and DNA (Kornberg, 1974), termed nucleosome (McGhee and Felsenfeld, 1980; Olins and Olins, 2003; Oudet et al., 1975). The nucleosome core particle (NCP) contains 145-147 bp DNA that wrap the protein complex of two copies of each H2A, H2B and H3, H4 approximately 1.7 fold (Luger et al., 1997a; Makde et al., 2010; Richmond and Davey, 2003) (section 2.3). Indeed, chromatin's primary compaction has been described as "particles on a string" with the advent of chromatin research (Olins and Olins, 1974), now known as 10 nm fiber composed of NCPs that are interconnected by linker DNA (Maeshima et al., 2014).

Work by Roger Kornberg (Lorch et al., 1987) and others (Almer et al., 1986; Han and Grunstein, 1988) established the nucleosome as general transcriptional repressor (Hughes and Rando, 2014; Kornberg, 1999, 2007). This led to the paradigm that DNA access is universally restricted in eukaryotes (Kornberg, 1999, 2007). So-called chromatin remodelers have originally been identified as *trans*-acting factors with pleiotropic effects on the transcriptional activation of a number of unrelated genes in yeast genetic screens

(Neigeborn and Carlson, 1984; Peterson and Herskowitz, 1992; Winston and Carlson, 1992); yeast denotes *Saccharomyces cerevisiae, Sc*, if not specified otherwise. This was established for the switch/sucrose non-fermentable (SWI/SNF) complex, that influences mating type switch genes and sucrose metabolism genes amongst others (Korber and Barbaric, 2014; Neigeborn and Carlson, 1984; Peterson and Herskowitz, 1992; Winston and Carlson, 1992). Likewise, the INO80 complex alters expression of, for example, phospholipid biosynthesis genes and phosphate metabolism genes (Ebbert et al., 1999; Korber and Barbaric, 2014). ATP-dependent chromatin remodelers in general play an important role in moving nucleosomes on DNA, in repositioning them in the context of nucleosomal arrays and in reconfiguring nucleosomes, in terms of histone variant exchange or nucleosome disassembly (Clapier et al., 2017; Narlikar et al., 2013).

Bona fide transcriptionally repressed chromatin domains, designated as heterochromatin nowadays, pose a yet more compact barrier to transcription (Allshire and Madhani, 2018). Heterochromatin can be designated by specific nucleosome modifications (such as epigenetic marks, that is for example posttranslational methylation of histone H3) or by additional recruitment of silencing systems (such as the silent information regulator (SIR) in yeast or Polycomb in metazoans) that together convey different degrees of chromatin folding (Allshire and Madhani, 2018).

On a molecular level, hindrance by compaction is exemplified for the tetranucleosome structure, a more compact organization of arrays of nucleosomes, in the presence or absence of the linker histone H1 (Schalch et al., 2005; Song et al., 2014). Still, dynamic exchange of the tetranucleosome stacking register observed on a single-molecule level *in vitro* might favor accessibility for regulatory factors to some extent (Kilic et al., 2018).

The assumption that further DNA compaction requires chromatin fibers with a diameter of around 30 nm is challenged nowadays (Fussner et al., 2011; Krzemien et al., 2017; Maeshima et al., 2014; Travers, 2014) although motivated by early experimental evidence that put forward a periodic chromatin fold beyond the 10 nm fiber (Finch and Klug, 1976; McGhee and Felsenfeld, 1980; Woodcock et al., 1984). Rather, large-scale chromatin interactions within the whole nucleus form regions of chromatin that are found in close proximity in 3D (topologically associated domains, TADs), as identified by various chromosome conformation capture methods (Gonzalez-Sandoval and Gasser, 2016; Maeshima et al., 2014) in metazoan interphase cells (Lieberman-Aiden et al., 2009; Nora et al., 2012; Rao et al., 2014; Sexton et al., 2012) and recently also in yeast (Eser et al., 2017). Many TADs have been associated with both actively transcribed genes and early

replication timing or, in contrast, silent genes and late replication timing (Gonzalez-Sandoval and Gasser, 2016; Maeshima et al., 2014; Nora et al., 2013).

Another layer of control for the initiation of transcription in eukaryotes directly acts on the transcription machinery, that is the recruitment of a set of general transcription factors that associate with RNA polymerases as well as the integration of regulatory cues encoded by enhancer elements (Kornberg, 1999, 2007).

2.1.2 The regulatory impact of genome organization

Genome organization differs greatly in bacteria, archaea and eukaryotes. The circular bacterial genome forms a supercoiled nucleoid that is further topologically constrained by nucleoid-associated proteins (Dame, 2005; Travers and Muskhelishvili, 2005, 2007). Bacterial genes are generally poised for transcription (Dame, 2005). Archaea are prokaryotes, still their circular genome features some characteristics of eukaryotic genome organization (Reeve, 2003). Most archaea have simple histones that share their histone fold domain with their eukaryotic homologues and are involved in the regulation of gene expression, likely due to organizing DNA similar to canonical eukaryotic nucleosomes (with the notable difference that a variable number of archaeal histone dimers oligomerize to scaffold DNA) (Henikoff and Smith, 2015; Mattiroli et al., 2017). Considering transcription, the archaeal transcription machinery is mostly homologue to its eukaryotic counterpart (Gehring et al., 2016). Its regulation is however simpler, as for example transcription initiation does not rely on a general transcription factor that consumes ATP for DNA unwinding (Nagy et al., 2015).

Taken together, gene regulation in eukaryotes has the highest level of complexity within the three domains of life and reaches beyond the regulatory mechanisms conferred by the transcription machinery *per se*. The trade off between DNA compaction and DNA accessibility is balanced by a sophisticated network of processes. The degree of compaction of nucleosomal arrays and the position of nucleosomes substantially restrict all DNA-templated cellular processes in eukaryotes.

2.2 Chromatin remodelers as organizers of eukaryotic genes

Genome wide maps for nucleosomes that represent the nucleosome positions and occupancies of cell populations with reference to a genomic locus such as the transcriptional start site (TSS) revealed that genic nucleosomes mostly reside at distinct

positions (Jiang and Pugh, 2009b; Lai and Pugh, 2017). In particular, a distinct nucleosome spacing and pattern is found at the vicinity of TSSs and at the nearby part of gene bodies in yeast (Jansen and Verstrepen, 2011; Mavrich et al., 2008; Yuan et al., 2005) and in higher eukaryotes (Hughes and Rando, 2014; Jiang and Pugh, 2009b) *in vivo*.

In yeast, a characteristic <u>n</u>ucleosome <u>f</u>ree <u>r</u>egion (NFR), bounded by a well-positioned -1 and +1 nucleosome, forms upstream of the nucleosome array at the beginning of gene bodies and the +1 nucleosome partially occludes the TSS (Albert et al., 2007; Jansen and Verstrepen, 2011; Jiang and Pugh, 2009a; Yuan et al., 2005). Likewise, histone variants or histone modifications have been associated with distinct regions of transcribed genes (Jiang and Pugh, 2009b; Liu et al., 2005; Narlikar et al., 2013); a prominent example is the enrichment of histone variant H2A.Z at -1 and +1 nucleosomes (Albert et al., 2007; Raisner et al., 2005).

Chromatin remodelers are major players organizing nucleosomes across eukaryotic genes (Lai and Pugh, 2017). Their universal role in nucleosome array formation was demonstrated in two seminal studies, establishing that *in vitro* reconstituted yeast chromatin reflects the *in vivo* nucleosome pattern only after addition of cellular factors and ATP, on the level of a single gene (Korber and Hörz, 2004) as well as in a genome-wide assessment (Hughes and Rando, 2014; Zhang et al., 2011). Still, DNA sequence can favor or disfavor the bending constraints imposed by nucleosomes (Hughes and Rando, 2014; Lai and Pugh, 2017; Segal et al., 2006; Segal and Widom, 2009) and also general regulatory factors such as Reb1 or Abf1 in yeast or CTCF in mammals influence the position of nucleosomes (Hughes and Rando, 2014; Krietenstein et al., 2016; Lai and Pugh, 2017; Wiechens et al., 2016).

2.2.1 Phylogenetic classification of chromatin remodelers

Chromatin remodelers share a Swi2/Snf2-type ATPase that belongs to the superfamily 2 (SF2) of 'helicase and NTP driven nucleic acid translocase' (Bartholomew, 2014; Flaus et al., 2006; Hopfner et al., 2012; Singleton et al., 2007). The ATPase features a catalytic domain, composed of two RecA-like domains (ATPase lobe 1 and ATPase lobe 2), and subfamily-specific additional motifs and/or domains (Bartholomew, 2014; Clapier et al., 2017; Hopfner et al., 2012) and is also referred to as 'main ATPase' in this work. The CHD subfamily (<u>c</u>hromodomain <u>h</u>elicase <u>D</u>NA binding protein 1, Chd1, in yeast) or ISWI subfamily (<u>i</u>mitation <u>sw</u>i<u>t</u>ch, ISW1a, ISW1b and ISW2 in yeast) of chromatin

remodelers consist of the main ATPase, or of the main ATPase and only few accessory subunits, respectively (Clapier and Cairns, 2009; Clapier et al., 2017). In contrast, chromatin remodelers that belong to the SWI/SNF subfamily (SWI/SNF and remodels the structure of chromatin, RSC, in yeast) or to the INO80 subfamily (INO80 and SWR1 in yeast) are large multisubunit molecular machines (Clapier and Cairns, 2009; Clapier et al., 2017; Flaus et al., 2006).

2.2.2 Functions of INO80 and of other chromatin remodelers

Different chromatin remodelers have specific functions, albeit partially redundant (Krietenstein et al., 2016). RSC (SWI/SNF subfamily) and INO80 have key functions in promoter architecture, but only INO80 is able to properly establish +1 nucleosome positioning in genome-wide *in vitro* assays *de novo* in the absence of other factors (Krietenstein et al., 2016). In turn, RSC establishes the NFR with physiological width *in vitro* (Krietenstein et al., 2016). Such remodeler specializations relate back to the ability of INO80 to evenly space tri-nucleosome substrates *in vitro* (Udugama et al., 2011), in contrast to RSC that both slides and disassembles/ejects nucleosomes (Clapier et al., 2016; Lorch et al., 2006). ISWI subfamily members and Chd1, however, are crucial for the formation of regularly spaced nucleosome arrays in genome wide studies (Gkikopoulos et al., 2011; Krietenstein et al., 2016; Lieleg et al., 2015; Ocampo et al., 2016). The Chd1 chromatin remodeler contributes to nucleosome stability and/or reassembly in the wake of transcription, likely in the presence of histone chaperones (Lee et al., 2012; Simic et al., 2003; Torigoe et al., 2013). Of note, *bona fide* histone chaperones assure proper nucleosome formation during DNA replication (Akey and Luger, 2003; Hammond et al., 2017).

The previously described periodic nucleosome arrangement at the beginning of genic regions was verified across species, exploiting technologic advances in high-throughput genomics (Hughes and Rando, 2014; Jiang and Pugh, 2009b). Chromatin remodelers that are conserved from fungi to mammals (Flaus et al., 2006) have a key role in establishing and maintaining this nucleosome organization (Figure 1).
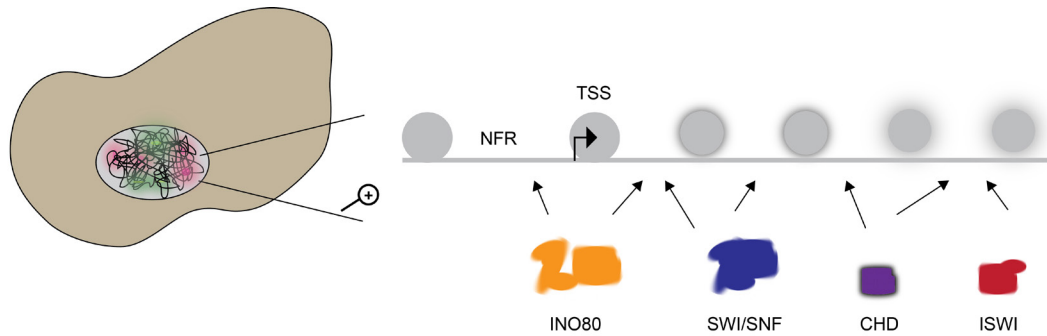
Figure 1. Impact of chromatin remodelers on the organization of nucleosomes in eukaryotes.
(left) Simplified scheme of a eukaryotic cell with its nucleus that contains chromatin. Chromatin forms TADs with different properties (see text) illustrated by the red and green shadings. (right) Simplified scheme of a regular nucleosome pattern at the 5'-end of a eukaryotic gene, exemplified here for yeast, with nucleosomes that are well positioned across genes in a population of yeast cells (solid grey balls), or less well positioned (shaded grey balls). The four chromatin remodeler subfamilies that contribute to nucleosome organization are indicated. For details see text. The representation is motivated by concepts outlined in Gonzalez-Sandoval and Gasser (2016), Krietenstein et al. (2016), Clapier et al. (2017) and in Jansen and Verstrepen (2011).

2.2.3   Implication of the INO80 subfamily in cellular functions

The SWR1 complex (INO80 subfamily) is a histone variant exchange factor that promotes the incorporation of histone variant H2A.Z (Hong et al., 2014; Lin et al., 2017; Luk et al., 2010; Ranjan et al., 2015). It is currently under debate whether the INO80 complex catalyzes the reverse reaction, which is removing H2A.Z/H2B from nucleosomes while introducing H2A/H2B (Brahma et al., 2017; Wang et al., 2016; Watanabe and Peterson, 2016; Watanabe et al., 2013). INO80's contribution to H2A.Z removal at yeast promoters *in vivo* might be marginal, as in this case transcription initiation is sufficient for H2A.Z turnover (Tramantano et al., 2016). In metazoans, the histone chaperone YL1 is an integral part of SWR1-homologues that assist H2A.Z incorporation (Latrick et al., 2016; Liang et al., 2016) and the H2A.Z specific histone chaperone ANP32E has a dominant role in H2A.Z eviction and redistribution in metazoans (Mao et al., 2014; Obri et al., 2014). The general impact of INO80 on H2A.Z turnover *in vivo* therefore remains elusive, given the described redundant pathways. Still, INO80 clearly has functional significance in removing H2A.Z as prearrangements for DNA repair and homologous recombination, both in yeast and human cells (Alatwi and Downs, 2015; Lademann et al., 2017).

INO80 has been associated to DNA double-strand (ds)-break repair in yeast because it is enriched in the vicinity of ds-breaks (Morrison et al., 2004; van Attikum et al., 2004).

INO80 localizes to the same genomic regions as phosphorylated H2A (which marks ds-breaks and signals DNA damage) (Morrison et al., 2004; van Attikum et al., 2004).

INO80 has also been implicated in assisting DNA replication in yeast and human cells, in particular with respect to the recovery of halted replication forks (Papamichos-Chronakis and Peterson, 2008; Shimada et al., 2008; Vassileva et al., 2014). One possibility for hindered DNA replication, ultimately leading to cell-cycle checkpoint activation, is the interference of the transcription and the replication machinery, on the same DNA molecule (Poli et al., 2017; Poli et al., 2016). The observation that INO80 contributes to efficient release of ultimately stalled <u>R</u>NA polymerase <u>II</u> (RNAPII) from chromatin (Lafon et al., 2015) is therefore an intriguing idea of how INO80 could be involved in DNA replication recovery *in vivo* (Lafon et al., 2015; Poli et al., 2017; Poli et al., 2016).

Beyond its roles in DNA replication and repair, INO80 has originally been identified as transcriptional co-regulator in yeast (Ebbert et al., 1999; Shen et al., 2000) (section 2.1.1). As such, INO80 has both activating as well as repressing impact on gene expression and is involved in the suppression of non-coding transcripts (Alcid and Tsukiyama, 2014; Conaway and Conaway, 2009; Ebbert et al., 1999; Klopf et al., 2017; Poli et al., 2017; van Attikum et al., 2004). Intriguingly, most +1 nucleosomes in a population of yeast cells recruit INO80 (Yen et al., 2013). INO80 is the only known chromatin remodeler that, as such, is sufficient to actively organize gene promoter regions *in vitro* (section 2.2.2) (Krietenstein et al., 2016). These observations reflect INO80's ability to influence transcription, in all likelihood by means of nucleosome remodeling (Krietenstein et al., 2016; Yen et al., 2013).

2.3   The nucleosome core particle as packing unit

High-resolution structures of the nucleosome revealed the symmetric arrangement of histones and the periodic arrangement of DNA around the octamer core (Davey et al., 2002; Luger et al., 1997a) (section 2.1.1). Briefly, DNA-protein contacts stabilize the DNA bent at each minor groove that faces the octamer, denoted <u>superh</u>elical <u>l</u>ocations (SHLs) 0.5, 1.5, 2.5 (contacts with the H3/4 tetramer), SHLs 3.5, 4.5, 5.5 (contacts with the H2A/B dimers) and SHL 6.5 (contacts with H3) (Bowman, 2010; Davey et al., 2002; Luger et al., 1997a; McGinty and Tan, 2015); unless specified further, SHLs denoted in this work refer to any side of the nucleosome. In this nomenclature, SHL0 denotes the base pair that aligns with the nucleosome dyad (Bowman, 2010; Davey et al., 2002; Luger et al., 1997a; McGinty and Tan, 2015). Minor grooves pointing away from the

octamer are located at integer SHLs and are positioned ideally to accommodate a chromatin remodeler, as Swi2/Snf2-type ATPases are assumed to track along the DNA minor groove (Dürr et al., 2005; Hopfner et al., 2012; Hopfner and Michaelis, 2007).

Histone proteins are well conserved among eukaryotes and crystal structures of nucleosomes composed of yeast, fly, frog, mouse or human histones overall do not depart from the basic scheme described above (Clapier et al., 2008; Luger et al., 1997a; McGinty and Tan, 2015; Tsunaka et al., 2005; Ueda et al., 2017; White et al., 2001). However, DNA stretching that compensates one base pair less, for example around SHL2 or around SHL5 on one or on both sides of the nucleosome, has been described for nucleosome structures in the context of different DNA sequences, indicating that 145-147 bp wrap the octamer core (Chua et al., 2012; Davey et al., 2002; Luger et al., 1997a; Makde et al., 2010; McGinty and Tan, 2015; Richmond and Davey, 2003; Tan and Davey, 2011; Tsunaka et al., 2005; Vasudevan et al., 2010).

2.3.1 Modes of nucleosome core particle dynamics

Due to their key regulating functions *in vivo*, nucleosomes are not expected to be static building blocks. Indeed, it was demonstrated that transcription factors could bind to a primarily wrapped part of DNA, which was attributed to inherent thermally driven conformational changes of nucleosomes that allow for DNA access (Anderson and Widom, 2000; Li et al., 2005; Li and Widom, 2004). Later, smFRET studies confirmed partial DNA unwrapping near the entry or exit site termed DNA breathing (Buning and van Noort, 2010; Koopmans et al., 2007; Koopmans et al., 2009). Such assays also revealed reversible, partial H2A/B dimer splitting off the H3/4 tetramer (Böhm et al., 2011) (section 2.4.3) and DNA gaping between both DNA gyres (one DNA gyre being defined as the DNA between either DNA entry/exit site and the dyad, respectively) (Ngo and Ha, 2015) as alternative modes of the intrinsic nucleosome dynamics (Fierz, 2016; Ordu et al., 2016). The compilation of the studies described below consolidates the nucleosome as dynamic packing unit, in particular with respect to thermal fluctuations of the DNA at the nucleosome entry or exit sites.

2.3.2 Nucleosome modifications associated with altered nucleosome plasticity

Many physiological relevant substrates show altered nucleosome stability. This suggests that the plasticity of the nucleosome is itself an important aspect to influence DNA accessibility. In that respect, smFRET assays that probe DNA release (e.g. at elevated salt concentrations, ultimately resulting in nucleosome disassembly) (Bönisch et al., 2012; Di

Cerbo et al., 2014; Gansen et al., 2009a; Gansen et al., 2009b; Neumann et al., 2009) and/or DNA conformational changes (Kim et al., 2015; Lee et al., 2011; Neumann et al., 2009) revealed that specific histone tail acetylation (Lee et al., 2011), specific acetylation of the compact histone fold (Di Cerbo et al., 2014; Kim et al., 2015; Neumann et al., 2009), unspecific stochastic histone acetylation (Gansen et al., 2009a) or incorporation of histone variants (Bönisch et al., 2012) either decrease nucleosome stability or increase the conformational heterogeneity with respect to nucleosomal DNA.

In particular, force spectroscopy experiments unambiguously related DNA unpeeling to nucleosome destabilization (Hall et al., 2009; Mihardja et al., 2006). For example, the DNA wrap that forms contacts with the H2A/B dimers represents a region of strong protein-DNA interactions, while such interactions are stronger close to the dyad, but very weak at the DNA entry/exit site (Hall et al., 2009; Killian et al., 2012). Further, the energy barrier that kinetically traps the outer DNA wrap (DNA that contacts the entry/exit sites and histones H2A/B) is on the order of thermal energy (Mihardja et al., 2006), as expected from the equilibrium accessibility assessments of nucleosomal DNA described above (Anderson and Widom, 2000; Li et al., 2005; Li and Widom, 2004).

A central hub that mediates the versatility of nucleosomes are the histone tails that extend the histone fold domains in eukaryotes (located at the N-terminus of all four core histones and additionally at the C-terminus of H2A) and protrude from the compact NCP with a contour length of up to ca. 10 nm (Davey et al., 2002; Iwasaki et al., 2013; Luger et al., 1997a; Luger et al., 1997b) (Figure 2). Multiple combinations of post-translational modifications on histone tails, introduced by specialized chromatin modifying enzymes, characterize regions of chromatin and prime them for specific 'reader' enzymes (histone code theory) (Jenuwein and Allis, 2001; Strahl and Allis, 2000). Still, histone tails *per se* sustain nucleosome stability, in particular histone tails H3 and H2B (Ferreira et al., 2007b; Iwasaki et al., 2013). Histone tail deletion considerably facilitates DNA unwrapping of the outer DNA wrap as inferred from single-molecule force spectroscopy (Bintu et al., 2012; Brower-Toland et al., 2005). This is in agreement with decreased DNA coordination at the DNA entry/exit sites of nucleosomes in the absence of histone tail H3 (Ferreira et al., 2007b).

2.3.3 Impact of a strong positioning sequence on nucleosome flexibility

Differential nucleosome stability was also observed for histone octamers derived from different species and for varying DNA positioning sequences (Gansen et al., 2009a; Tóth

et al., 2013). The best-studied nucleosome positioning sequence (Figure 2) is the Widom 601-sequence (601-seq) that has been generated by systematic evolution of ligands by exponential enrichment (SELEX, similar to Irvine et al. (1991)) (Lowary and Widom, 1998). For the canonical non-palindromic 601-seq, the gyre containing 10 bp separated TA-steps across the H3/4 surface is energetically more stable than the other side of the nucleosome (Chua et al., 2012; McGinty and Tan, 2015) and also favors hexasome formation (formation of a nucleosome-subcomplex that lacks one H2A/B dimer) with the remaining dimer at this nucleosome side (Levendosky et al., 2016). Interestingly, DNA unwrapping of nucleosomes (outer DNA wrap of one gyre only) in the presence of forces in the pico-Newton range is clearly favored at the opposite gyre (Ngo et al., 2015). An elegant combination of force spectroscopy and smFRET applied to single nucleosomes revealed this asymmetric unwrapping behavior (Ngo et al., 2015). As further derived from cryo-electron microscopy (cryoEM) single particle class averages, this effect has been attributed to subtle conformational changes that are transmitted via the histone octamer core and cause H3-DNA contacts to be tightened on one gyre, when DNA coordination by H3 is partly released around SHL6.5 from the opposite gyre (Bilokapic et al., 2018).
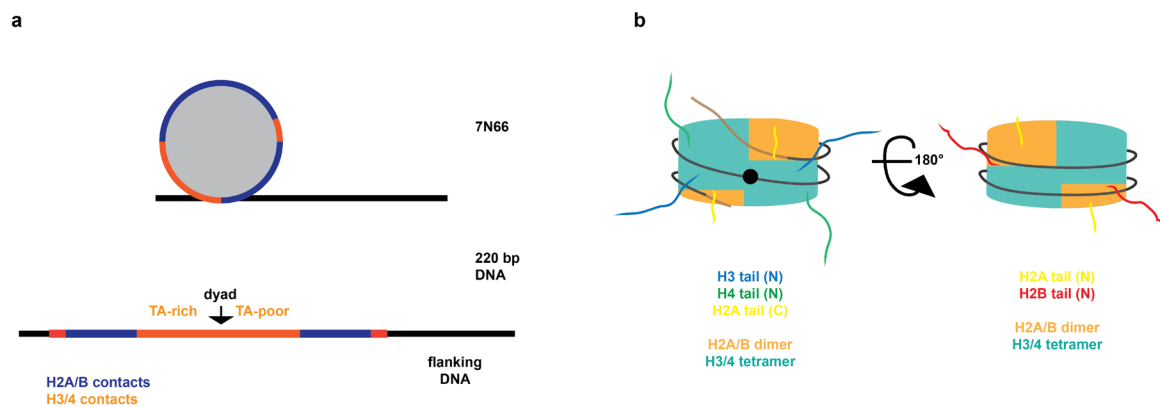
Figure 2. Schematic representation of nucleosomes with flanking DNA and histone tails.
(a) **Histone octamer position on a 220 bp fragment of the 601-seq used in the present study. The histones form distinct contacts to the DNA and a 7 bp exit side linker and a 66 bp entry side linker protrude from the NCP. The exact DNA sequence is summarized in Figure 12. The underlying concepts have been described by Lowary and Widom (1998), Vasudevan et al. (2010) and McGinty and Tan (2015). (b) Schematic overview of the histone tail extensions of the NCP. N-terminal tails of H2B, H3 and H4 are long (≥ 20 residues) and H2A N- and C-terminal tails are shorter (> 10 residues). For clarity, entry and exit side flanking DNA (brown) are included in the left depiction, the NCP DNA is depicted in black. Nucleosome structures that motivated this representation have been described in Davey et al. (2002), Iwasaki et al. (2013), Vasudevan et al. (2010) and Luger et al. (1997a).**

2.4 Models for nucleosome remodeling

Chromatin remodelers are functionally diverse (section 2.2.2) but their Swi2/Snf2-type ATPases might share a common mechanism that guides DNA translocation across the octamer surface (Clapier et al., 2017). Nucleosome remodeling in all likelihood relates back to ATP-dependent translocation of DNA that involves a ratcheting movement of the two lobes of the ATPase domain, when the remodeling enzyme resides at a fixed position relative to the octamer core (Bartholomew, 2014; Bowman, 2010; Clapier et al., 2017; Hopfner and Michaelis, 2007; Mueller-Planitz et al., 2013a; Wigley and Bowman, 2017). Recent structural evidence of substrate-bound remodelers outlined that the nucleosome-bound ATPase of the yeast SWI/SNF complex (Snf2), the nucleosome-bound single-subunit yeast Chd1 remodeler and the nucleosome-bound minimal functional INO80 complex composed of 11 subunits (INO80[conserved], here from *Chaetomium thermophilum, Ct*) pump DNA at SHL2, proximal (Liu et al., 2017) or distal (Farnung et al., 2017; Sundaramoorthy et al., bioRxiv: 10.1101/290874; Sundaramoorthy et al., 2017) to the nucleosome flanking DNA, or at SHL6 near the DNA entry site of the nucleosome (Eustermann et al., 2018), respectively. Assuming DNA minor groove tracking (Dürr et al., 2005; Hopfner et al., 2012; Hopfner and Michaelis, 2007), chromatin remodelers potentially both translocate and transiently twist DNA (Clapier et al., 2017). Still, major variations between remodeler subfamilies could occur, given their different modes of engaging the nucleosome with respect to the translocation site on DNA and with respect to the complementary interactions that anchor the ATPase on the nucleosome (Ayala et al., 2018; Eustermann et al., 2018; Farnung et al., 2017; Liu et al., 2017; Sundaramoorthy et al., bioRxiv: 10.1101/290874; Sundaramoorthy et al., 2017) (section 2.5.2).

Evidence for DNA translocation by remodelers from the CHD, ISWI, SWI/SNF and INO80 subfamily was first derived from bulk *in vitro* investigations that make use of nucleosomes wrapped by DNA with a single gap (Brahma et al., 2017; McKnight et al., 2011; Ranjan et al., 2015; Saha et al., 2005; Schwanbeck et al., 2004; Zofall et al., 2006). Those substrates interrupt translocation and in agreement with complementary crosslinking studies locate the site of translocation to an internal nucleosome site (around SHL2) for the ISWI remodeler subfamily (Dechassa et al., 2012; Schwanbeck et al., 2004; Zofall et al., 2006), for Chd1 (McKnight et al., 2011) and for the SWI/SNF remodeler subfamily (Dechassa et al., 2012; Saha et al., 2005; Zofall et al., 2006). For INO80, elegant crosslinking, footprinting and remodeling assays with nucleosomes

revealed for the first time that the ATPase interacts with DNA close to SHL6 near the DNA entry site (Brahma et al., 2017); still the ATPase of the INO80-subfamily member SWR1 requires interaction with DNA around SHL2 for histone variant exchange (Ranjan et al., 2015).

Some remodelers tolerate single DNA nicks in the nucleosomal DNA that prevent potential twist accumulation and/or twist diffusion (Längst and Becker, 2001; Saha et al., 2005; Zofall et al., 2006), especially if the nick is not introduced in the vicinity of the translocation site initially (Brahma et al., 2017; Zofall et al., 2006). This phenomenon has been described in the context of INO80 and of an ISWI subfamily homologue (Brahma et al., 2017; Zofall et al., 2006). In case of INO80, torsional strain might therefore be required for initiation of remodeling, but probably twist is only marginally contributing to continued nucleosome sliding (that is, when a distant DNA nick is being moved to the translocation site during remodeling without major interferences) (Brahma et al., 2017).

2.4.1 Evidence for incremental sub-steps by chromatin remodelers

Swi2/Snf2-type ATPase mediated incremental movement of DNA with a step-size of ca. 1 bp has been inferred from early structure guided models (Hopfner and Michaelis, 2007) that hold true given recent structural insights into the nucleosome bound Chd1 (in an activated ground state, induced by a nucleotide analogue) and the nucleosome bound Snf2 (Farnung et al., 2017; Liu et al., 2017; Wigley and Bowman, 2017) and in particular agree with DNA translocation snapshots and the DNA translocation behavior of a related SF2 enzyme (Gu and Rice, 2010; Myong et al., 2007; Wigley and Bowman, 2017). Indeed, for chromatin remodelers ISWI and RSC, 1 bp and 1-2 bp elementary steps, respectively, have been identified on a single molecule level (Deindl et al., 2013; Harada et al., 2016; Sirinakis et al., 2011). The elegant smFRET approach applied to this end probes the conformational changes of surface-tethered nucleosomes with a donor-labeled octamer and an acceptor labeled DNA moiety upon remodeling (Deindl et al., 2013; Harada et al., 2016). When the exiting DNA carries the acceptor label, a stepwise increase in label distance (decrease in FRET efficiency) is equivalent to remodeling; alternative relative label positions have been used to increase mechanistic insights (Deindl et al., 2013; Harada et al., 2016).

Any sequential histone-DNA contact release-recapture mechanism, that at the same time stabilizes the histone octamer core, may enable a global shift of the DNA with respect to the octamer core; still, models herein differ systematically but are not mutually exclusive

(Bartholomew, 2014; Bowman, 2010; Clapier et al., 2017; Mueller-Planitz et al., 2013a; Narlikar et al., 2013). The contributions of (i) DNA twisting, (ii) DNA looping and (iii) octamer deformation are outlined in the following.

2.4.2 Relevance of DNA twisting by chromatin remodelers

Intact nucleosomes that feature DNA stretching (section 2.3) accommodate slightly fewer bp/turn in some DNA segment, compared to nucleosomes that have 1 bp more (Richmond and Davey, 2003; Tan and Davey, 2011). This motivated the idea of stable twist-defect intermediates in nucleosome remodeling (Richmond and Davey, 2003). If such a twist-defect is propagated to the next DNA segment and ultimately beyond the outmost histone-DNA contact, net DNA translocation occurs (Bartholomew, 2014; Bowman, 2010; Clapier et al., 2017; Mueller-Planitz et al., 2013a; Narlikar et al., 2013).

The recent Snf2 and Chd1 structures suggest movement of DNA from SHL2 in direction of the nucleosome dyad (SHL0) (Farnung et al., 2017; Liu et al., 2017). This implies transient DNA gain (and possibly undertwisting) ahead of the translocation site (SHL2) in direction of the nucleosome dyad. Interestingly nucleosome-based smFRET experiments revealed that active remodeling by ISWI complexes introduces a chronic DNA deficit of 4-7 bp between the nucleosome entry site and the ATPase translocation site (Deindl et al., 2013). This model implies DNA stretching (and possibly overtwisting) between the translocation site and the nucleosome entry site and DNA compression (and possibly undertwisting) ahead of the ATPase in direction of the dyad. As a rational, including the possibility of DNA bulge formation in the vicinity of the translocation site (section 2.4.4), this has been proposed earlier as 'wave-ratchet-wave' model for the main ATPase of RSC (SWI/SNF subfamily) (Saha et al., 2005) and is in agreement with Snf2 and Chd1 structural models (Farnung et al., 2017; Liu et al., 2017). With respect to the nucleosome remodeling mechanism, the nucleosome-based smFRET data of ISWI remodeling support transient DNA deformation (Deindl et al., 2013) and point out the possibility of octamer rearrangements that could accommodate DNA strain (Clapier et al., 2017; Deindl et al., 2013; Mueller-Planitz et al., 2013a).

2.4.3 Relevance of octamer plasticity for chromatin remodelers

While nucleosome crystal structures did not indicate histone octamer plasticity, this mechanistic option for chromatin remodeling receives growing attention owing to studies based on smFRET (Böhm et al., 2011), nuclear magnetic resonance (NMR) (Sinha et al., 2017) and single-particle cryoEM (Bilokapic et al., 2018) that do not impose structural

rigidity. In case of nucleosome dimer splitting, DNA opening actually reflects a reversible release of DNA-bound H2A/B dimers from the tetramer-dimer interface (Böhm et al., 2011) (section 2.3.1). Likewise, the H3/4 tetramer might asymmetrically rearrange within the octamer to respond to DNA unwrapping (Bilokapic et al., 2018) (section 2.3.3). Importantly, NMR-data on nucleosomes in the presence of an ATPase of the ISWI subfamily in an activated ground state (induced by a nucleotide analogue) suggest alterations of the H3/4 interface (Sinha et al., 2017). Such H3/H4 interface flexibility has been shown to be a prerequisite for efficient nucleosome remodeling by different ISWI homologues and by RSC (but explicitly not for INO80 nucleosome sliding) (Sinha et al., 2017). Given those insights, histone octamer conformational adaptations certainly need to be considered for remodeling mechanisms (Clapier et al., 2017; Mueller-Planitz et al., 2013a; Narlikar et al., 2013) but a concerted swiveling reorientation of the entire octamer involving the breakage of many histone-DNA contacts at a time (Bowman, 2010) seems unlikely.

2.4.4 Relevance of DNA looping by chromatin remodelers

Translocation-induced DNA loop formation can explain nucleosome remodeling (Bartholomew, 2014; Bowman, 2010; Clapier et al., 2017; Mueller-Planitz et al., 2013a; Narlikar et al., 2013). When linker DNA is enzymatically forced to shift onto the octamer core, a loop or bulge, involving the transient breakage of some histone-DNA contacts, could form (Bartholomew, 2014; Bowman, 2010; Clapier et al., 2017; Mueller-Planitz et al., 2013a; Narlikar et al., 2013). Upon propagation of this loop or bulge through the nucleosome, in this case maybe even without changing the rotational phasing of the DNA *per se*, nucleosomes ultimately end up at a new position when the DNA loop is released at the nucleosome exit site (Bartholomew, 2014; Bowman, 2010; Clapier et al., 2017; Mueller-Planitz et al., 2013a; Narlikar et al., 2013). This model is attractive for the multisubunit SWI/SNF subfamily remodelers, as inferred from biochemical data (Kassabov et al., 2003; Liu et al., 2011) and from single-molecule force spectroscopy experiments that investigate either nucleosomes engaged by SWI/SNF subfamily remodelers (Zhang et al., 2006) or DNA engaged by RSC or a subcomplex thereof (Clapier et al., 2016; Lia et al., 2006; Sirinakis et al., 2011). However, only small DNA loops of 1-2 bp are supported by smFRET data on RSC mediated nucleosome sliding (Harada et al., 2016). Interestingly, looping DNA off the octamer core is now put forward to explain the mechanism of INO80[conserved] due to recent structural insights (Ayala et al., 2018; Eustermann et al., 2018) (section 2.5.2).

Taken together, the ATP-dependent DNA distortions introduced by chromatin remodelers may twist and/or loop DNA on the octamer surface, which might also entail octamer deformations to some extent (Bartholomew, 2014; Bowman, 2010; Clapier et al., 2017; Mueller-Planitz et al., 2013a; Narlikar et al., 2013).

2.5 The modular architecture of the INO80 complex

2.5.1 Conservation of INO80 submodules

The INO80 complex has been described for *Saccharomyces cerevisiae* (*Sc*), *Schizosaccharomyces pombe (Sp)*, *Homo sapiens* (*Hs*) and *Drosophila melanogaster* (*Dm*) (Chen et al., 2011; Conaway and Conaway, 2009; Ebbert et al., 1999; Hogan et al., 2010; Jin et al., 2005; Klymenko et al., 2006; Shen et al., 2000). Its core is composed of a set of highly conserved subunits, but the INO80 complex features also species-specific subunits (Conaway and Conaway, 2009; Hogan et al., 2010). The modular organization of subunits by main ATPase binding regions is similar for *Hs*INO80 and *Sc*INO80 as inferred from biochemical, crosslinking and structural analysis (Chen et al., 2011; Chen et al., 2013; Tosi et al., 2013; Watanabe et al., 2015). Here, the central ATPase is not only the catalytic core, but also has a scaffolding role to arrange the submodules of the complex (Chen et al., 2011; Chen et al., 2013; Schubert et al., 2013; Szerlong et al., 2008; Tosi et al., 2013; Watanabe et al., 2015).

Most actin-related proteins (Arps) and actin associate with the helicase SANT associated domain (HSA-domain) of the main ATPase (ARP-module, Actin, Arp4, Arp8, complemented by TATA-binding protein-associated factor 14, Taf14 and the INO eighty subunit 4, Ies4, in *S. cerevisiae*) (Chen et al., 2011; Gerhold et al., 2012; Shen et al., 2003; Szerlong et al., 2008; Tosi et al., 2013). The RuvB-like 1/2 (Rvb1/2) hexamer associates with the INO80-subfamily specific insertion of the main ATPase and further bridges Arp5 and Ies6 with the main ATPase (Chen et al., 2011; Chen et al., 2013; Jónsson et al., 2004; Tosi et al., 2013; Zhou et al., 2017). Species-specific subunits associate with the N-terminus of the main ATPase (species-specific submodule, or NHP10-module with Ies1, Ies3, Ies5 and non-histone protein 10, Nhp10, in *S. cerevisiae*) (Chen et al., 2011; Tosi et al., 2013; Zhou et al., 2018). Deletion of the NHP10-module, resulting in the loss of subunits Ies1, Ies3, Ies5 and Nhp10 does not impair *in vitro* nucleosome sliding *per se* (Tosi et al., 2013; Zhou et al., 2018). However, this submodule is required for nucleosome binding (Tosi et al., 2013) and is crucial to tune INO80's activity in response to flanking DNA length (section 2.6.3) (Zhou et al., 2018). In that

respect, the yeast species-specific NHP10-module confers the requirement for long overhang DNA (60 bp or more) for efficient INO80 nucleosome sliding (Udugama et al., 2011; Zhou et al., 2018). Potentially the NHP10-module therefore has *in vivo* relevance because INO80 has been mapped near the +1 nucleosome and the NFR, which has approximately the same DNA length (Yen et al., 2012; Yen et al., 2013). Furthermore, efficient recruitment of INO80 to DNA ds-breaks depends on Nhp10 (Morrison et al., 2004).

2.5.2 Features of the conserved INO80 subcomplex

Recent cryo-EM structures provided insights into the conformations of INO80[conserved] in the absence (Aramayo et al., 2018) or presence of the nucleosome (Ayala et al., 2018; Eustermann et al., 2018), comprising the INO80 ATPase, Ies2, Arp5, Ies6, the heterohexameric Rvb1/2 and Actin, Arp4, Arp8 in case of the *Hs*INO80[conserved] (Aramayo et al., 2018; Ayala et al., 2018) and 11 different subunits in case of the fungal *Ct*INO80[conserved] (including additionally the *S. cerevisiae* homologues of Taf14 and Ies4) (Eustermann et al., 2018). The INO80 core complex (comprising the Ino80 main ATPase, Ies2, Arp5, Ies6 and the heterohexameric Rvb1/2, INO80[core]) forms extensive contacts with the DNA gyre proximal to the entry DNA (Ayala et al., 2018; Eustermann et al., 2018). For *Ct*INO80[core] additional contacts have been identified on the molecular level between *Ct*INO80[core] and the octamer disk surface on the same nucleosome side as the entry side DNA gyre, as well as between *Ct*INO80[core] and DNA and histones on the opposite side of the nucleosome (Eustermann et al., 2018) (section 2.6.2). A key finding is the docking of the ATPase onto nucleosomal DNA at SHL6 near the nucleosome entry site (for *Ct*INO80[core]; SHL6-7 for *Hs*INO80[core] in an activated ground state, induced by a nucleotide analogue) and the counter-grip by Arp5 on the same DNA gyre (Ayala et al., 2018; Eustermann et al., 2018). In particular these interactions contributed by the Ino80 main ATPase and Arp5 with nucleosomal DNA point to a putative remodeling mechanisms that relies on transient DNA looping off the octamer surface; this would then disturb the contact sites of the H2A/B dimer with the DNA, on the DNA gyre proximal to the entry DNA (Ayala et al., 2018; Eustermann et al., 2018). This mechanistic model is also supported by earlier observations that the Arp5/Ies6 submodule is absolutely required for productive nucleosome sliding (Ayala et al., 2018; Eustermann et al., 2018; Shen et al., 2003; Tosi et al., 2013; Watanabe et al., 2015; Willhoft et al., 2016; Yao et al., 2015).

The three nucleosome interaction platforms (i) histone tails, (ii) DNA and (iii) the octamer disc surfaces (McGinty and Tan, 2015) contribute to very different extents to the anchoring of the main ATPase of chromatin remodelers, as exemplified when comparing the nucleosome-bound ATPase of the yeast SWI/SNF complex (Snf2), the nucleosome-bound single-subunit yeast Chd1 remodeler, the *Hs*INO80[conserved] and the *Ct*INO80[conserved] (Ayala et al., 2018; Eustermann et al., 2018; Farnung et al., 2017; Liu et al., 2017; Sundaramoorthy et al., bioRxiv: 10.1101/290874; Sundaramoorthy et al., 2017). Anchoring of any remodeler ATPase is a prerequisite for a presumably uniform DNA ratcheting principle (section 2.4) (Clapier et al., 2017) and the multi-facetted interaction of the *Ct*INO80[conserved] complex with DNA and histones on both sides of the nucleosome is unique in that respect (Eustermann et al., 2018).
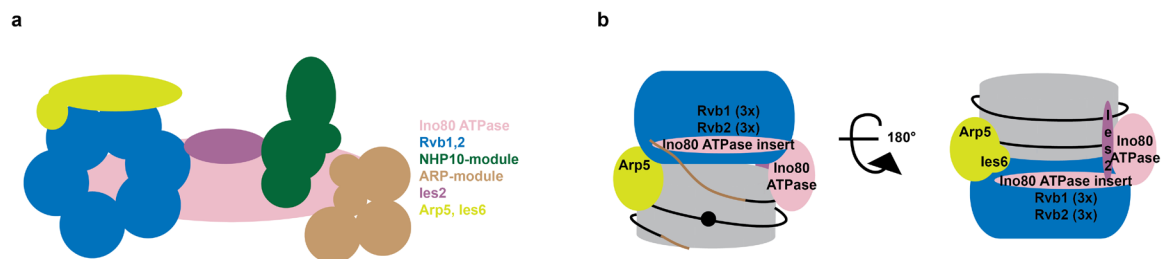
Figure 3. Simplified schemes of the organization of INO80 modules by the Ino80 main ATPase and of the interaction of INO80[core] with the NCP.
(a) The Ino80 main ATPase, the subunits Ies2, Ies6 and Arp5 as well as the heterohexameric Rvb1,2, the ARP-module (5 subunits) and the NHP10-module (4 subunits) form the *Sc*INO80 complex, for details see text. (b) INO80[core] interactions with the NCP and the entry side DNA gyre. The ARP-module is not displayed and the NHP10-module is missing. For details see text. The simplified representation of the INO80 topology in (a) has been motivated by studies from Bao and Shen (2011), Tosi et al. (2013), Watanabe et al. (2015) and Aramayo et al. (2018). The simplified representation of the INO80-nucleosome interaction in (b) has been motivated by studies from Eustermann et al. (2018) and Ayala et al. (2018).

The Rvb1/2 heterohexamer stabilizes the relative orientation of the Arp5/Ies6 module and the INO80 main ATPase upon nucleosome engagement (Ayala et al., 2018; Eustermann et al., 2018). Interestingly, parts of the Ino80 main ATPase are engaged by the Rvb1/2 in a chaperone-like manner, that is, the large INO80-subfamily specific main ATPase insert is enclosed by the cavity in-between the oligonucleotide- and oligosaccharide binding folds (OB-folds) of the Rvb1/2 hexamer (Aramayo et al., 2018; Ayala et al., 2018; Eustermann et al., 2018). Rvb1/2 belong to the family of AAA$^+$ ATPases (ATPases associated with a variety of cellular activities) and have been suggested to promote the assembly of the multisubunit INO80 complex by taking charge of the INO80-subfamily specific ATPase insert (Zhou et al., 2017).

2.5.3   The ARP-module within the conserved INO80 subcomplex

Implications of the ARP-module in INO80 mediated nucleosome remodeling remain enigmatic on the molecular level, since the ARP-module as part of the INO80^{conserved} forms a bulky extension to the nucleosome-bound INO80^{core} that does not qualify for high resolution refinement in the described cryoEM derived structures (Ayala et al., 2018; Eustermann et al., 2018).

Of note, also the INO80-subfamily member SWR1 and the SWI/SNF subfamily complexes contain actin and/or Arps that are nucleated by a homologues HSA domain of the respective main ATPase (Cao et al., 2016; Schubert et al., 2013; Szerlong et al., 2008). The SWR1 ARP-module and the SWI/SNF ARP-module also share their overall architecture on the molecular level (actin and one Arp or two Arps bound to the HSA domain, respectively) (Cao et al., 2016; Schubert et al., 2013), suggesting a similar ARP-module for INO80 (Bartholomew, 2013). Still the INO80 ARP-module features actin and two Arps (Gerhold et al., 2012; Szerlong et al., 2008).

The ARP-module of the SWI/SNF subfamily remodeler RSC is required for efficient nucleosome ejection and to a lesser extent for nucleosome sliding, likely because in the presence of Arps, ATPase activity is coupled to translocation more efficiently than for the isolated main ATPase (Clapier et al., 2016). Genetic evidence suggests that the ARP-module directly affects the main ATPase of RSC and thereby regulates nucleosome sliding and ejection (Clapier et al., 2016; Szerlong et al., 2008). The ARP-module's impact is functionally integrated by two distinct ATPase motifs, namely a small N-terminal post-HSA domain and a subfamily-specific insertion of one ATPase lobe (Clapier et al., 2017; Clapier et al., 2016; Szerlong et al., 2008). Still, a global large-scale conformational rearrangement of the ARP-module may be a prerequisite for the formation of a SWI/SNF conformation that engages the nucleosome in a remodeling competent state (Zhang et al., 2018).

Given the importance of the ARP-module in SWI/SNF-subfamily remodelers, functional implications of the INO80 ARP-module are likely. Indeed, the ARP-module contributes to binding of DNA, nucleosomes and histones (Gerhold et al., 2012; Kapoor et al., 2013). Its deletion impairs both, INO80 ATPase and sliding activity (Tosi et al., 2013; Watanabe et al., 2015).

2.6 Regulation of chromatin remodelers

In order to respond to specific environmental or substrate-associated cues, chromatin remodelers that share homologues of the Swi2/Snf2-ATPase, have evolved auxiliary domains (or elements) or auxiliary subunits (or modules of several subunits) that provide means of regulation and contribute to their functionally distinct roles (Clapier et al., 2017).

2.6.1 Nucleosome-remodeler crosstalk established for ISWI

With respect to regulation, the ISWI subfamily of remodelers has been studied thoroughly. The ISWI subfamily ATPase elements AutoN and NegC inhibit both ATP hydrolysis and coupling to productive translocation, respectively, in the resting state (Clapier and Cairns, 2012; Clapier et al., 2017; Yan et al., 2016). Upon substrate commitment, the histone H4 tail relieves autoinhibition of the ATPase by AutoN in an allosteric manner (Racki et al., 2014), interacting with a binding interface located on the surface of one of the two ATPase lobes (Ludwigsen et al., 2017; Yan et al., 2016). Conversely, the ISWI C-terminal DNA-binding domain H̲AND-S̲ANT-S̲LIDE (HSS) senses nucleosome flanking DNA (Mueller-Planitz et al., 2013b) and influences nucleosome sliding via the adjacent NegC element (Clapier and Cairns, 2012; Hwang et al., 2014; Leonard and Narlikar, 2015). If HSS favorably engages with the nucleosome, this transiently relieves the negative regulatory NegC interaction with the ATPase core (Mueller-Planitz et al., 2013a; Yan et al., 2016). Nucleosome-based single-molecule FRET studies of ISWI subfamily remodelers (introduced in sections 2.4.1 and 2.4.2) convincingly demonstrated that the sensing of nucleosomal epitopes (H4 tail and overhang DNA) by the ISWI homologue A̲TP-dependent c̲hromatin-assembly f̲actor (ACF) occurs during regulatory pauses that stochastically interrupt active nucleosome sliding (Hwang et al., 2014). Both inhibitory elements, AutoN and NegC, have been shown to cooperate with the histone octamer acidic patch motif upon activation of an ATPase homologue of the ISWI subfamily (Gamarra et al., 2018). The so-called acidic patch is formed on either octamer disk surface by H2A/B and features negatively charged residues that qualify as interaction hot-spot (McGinty and Tan, 2015). The importance of the aforementioned regulatory pauses for ISWI mediated nucleosome sliding (Hwang et al., 2014) has been underlined by a follow-up single-molecule FRET study that introduces a weak nucleosome acidic patch mutant (Gamarra et al., 2018). In agreement with the corresponding bulk data, this nucleosome mutant prolongs such regulatory pause

phases of enzymatic nucleosome sliding and also reduces the distance the remodeler can progress in phases of active translocation (Gamarra et al., 2018).

Mono-nucleosome centering by the ISWI homologue ACF likely involves monitoring of nucleosome flanking DNA on both sides of the nucleosome by two remodelers bound to the nucleosome (Blosser et al., 2009; Leonard and Narlikar, 2015; Racki et al., 2009). ACF moves nucleosomes back and forth on DNA in a processive manner as inferred from nucleosome-based smFRET experiments (Blosser et al., 2009). This is probably achieved by two remodelers with opposing directionality (Blosser et al., 2009; Leonard and Narlikar, 2015; Racki et al., 2009). Such a mechanism is supported by structural data on the nucleosome-bound main ATPase of an ACF homologue that cooperatively associates to both sides of the nucleosome (Racki et al., 2009). Nucleosome sliding by one ACF protomer at a time might be gated by the nucleosome flanking DNA that allows for favorable interactions with HSS und thus productive translocation by the remodeler's main ATPase (Leonard and Narlikar, 2015). In that way, both remodelers could take turns in sliding and therefore center nucleosomes (Leonard and Narlikar, 2015; Racki et al., 2009).

2.6.2 Generalization of key principles of the nucleosome-remodeler crosstalk

Motifs of the main ATPase of different remodelers that interact with the H4-tail form a conserved binding patch for the ISWI-subfamily ATPase, for Chd1 and for the SWI/SNF-subfamily ATPase (Farnung et al., 2017; Liu et al., 2017; Yan et al., 2016). Still, the H4-tail's regulatory impacts differ, depending on the remodeler, and are further diversified in the presence of site-specific histone tail modifications (Clapier and Cairns, 2012; Ferreira et al., 2007a; Hauk et al., 2010; Liu et al., 2017; Yan et al., 2016). Of note and in contrast to Chd1 and ISWI subfamily remodelers, histone tails negatively regulate nucleosome sliding by the INO80 complex (Ayala et al., 2018; Clapier and Cairns, 2012; Hauk et al., 2010; Udugama et al., 2011; Yan et al., 2016). Histone tail removal facilitates INO80 nucleosome sliding, an effect observed for histone H2A tail removal (Udugama et al., 2011) (*Sc*INO80) or H3 tail removal (Ayala et al., 2018) (*Hs*INO80[conserved]) and also in the absence of all histone tails (*Sc*INO80) (Udugama et al., 2011). The underlying mechanism for increased ATPase and remodeling rates of *Sc*INO80 in the absence of histone tails (Udugama et al., 2011) needs to be clarified.

A negative influence on remodeling has so far been observed for members of all remodeler subfamilies when mutating the H2A/B acidic patch (Dann et al., 2017;

Eustermann et al., 2018; Gamarra et al., 2018; Levendosky et al., 2016). Strikingly, *Ct*INO80^{conserved} nucleosome sliding is completely abrogated upon octamer acidic patch disruption (Eustermann et al., 2018). This observation has been explained by the perturbation of important interactions of INO80 subunits Arp5 and Ies2 with the acidic patch of the octamer disk surface on the same nucleosome side as the entry side DNA gyre and with the acidic patch on the opposite nucleosome side, respectively (Eustermann et al., 2018).

2.6.3 Comparison of nucleosome centering mechanisms of remodeler subfamilies

Mononucleosome substrates with DNA overhangs are centered on DNA by some chromatin remodelers *in vitro* (Chd1, ISW1a, ISW2, INO80) (McKnight et al., 2011; Schwanbeck et al., 2004; Stockdale et al., 2006; Udugama et al., 2011), while other remodelers move mono-nucleosomes towards the short DNA end (SWI/SNF, RSC, ISW1b) (Kassabov et al., 2003; Liu et al., 2011; Stockdale et al., 2006). Strikingly, so far two contrasting mechanisms for mono-nucleosome centering have been proposed based on smFRET results that show bidirectional movement of a single nucleosome induced by ACF or Chd1, respectively. While ACF probably acts as a dimer (Blosser et al., 2009; Leonard and Narlikar, 2015; Racki et al., 2009) (section 2.6.1), Chd1 probably works as a monomeric remodeler (Nodelman et al., 2017; Qiu et al., 2017). Chd1 may switch between translocation sites (that is, the ATPase interacts in turn with different SHLs) for bidirectional nucleosome sliding, without dissociating from the nucleosome (Qiu et al., 2017). Two of the aforementioned studies rely on nucleosome-based smFRET experiments and provide strong evidence for (i) two ACF remodelers per nucleosome (using a third color for concomitant direct visualization of the labeled remodeler) (Blosser et al., 2009) or (ii) one Chd1 per nucleosome. Chd1 was attached to the surface of the microscope's measurement chamber and binds labeled nucleosome; this reversed tethering strategy assures investigation of one Chd1 per nucleosome (Qiu et al., 2017).

Mono-nucleosome centering by INO80 has been investigated (Udugama et al., 2011; Willhoft et al., 2017; Zhou et al., 2018) and may rely on yet another mechanism. Two recent studies revealed that INO80 and INO80^{conserved} respond to flanking DNA length (Willhoft et al., 2017; Zhou et al., 2018), although different regulatory aspects apply. In case of *Sc*INO80, the species-specific NHP10-module conveys a switch-like response that renders the remodeler almost invariant to nucleosomes with short flanking DNA but highly processive if flanking DNA is long (section 2.5.1) (Zhou et al., 2018). Instead, in case of *Hs*INO80^{conserved} (which is lacking any species-specific submodule), an

unprecedented dimer of remodeler complexes cooperates to move nucleosomes away from either DNA end (Willhoft et al., 2017). Both, *Sc*INO80 and *Hs*INO80[conserved] can also redistribute centered mono-nucleosomes with long flanking DNA on both sides to some extent (Willhoft et al., 2017; Zhou et al., 2018), indicating that the absolute length of flanking DNA on either side independently guides INO80 (Willhoft et al., 2017). Still, how DNA overhang length sensing is integrated by INO80 is not entirely clear. Interestingly, tri-nucleosome spacing and *in vitro* nucleosome positioning has been reported for the *Sc*INO80 (Krietenstein et al., 2016; Udugama et al., 2011) but the underlying mechanism remains enigmatic. Given that the architecture and topology of the *Sc*INO80-nucleosome complex (Tosi et al., 2013) and structures of the *Ct*INO80[conserved]-nucleosome complex (Eustermann et al., 2018) and the *Hs*INO80[conserved]-nucleosome complex (Ayala et al., 2018) show a 1:1 stoichiometry, both, a monomeric INO80 complex as well as a functional dimeric INO80 complex (Willhoft et al., 2017) are conceivable for nucleosome sliding and positioning.

Taken together, the rearrangement of auxiliary domains or auxiliary subunits of chromatin remodelers, mostly in response to specific substrate cues or upon substrate commitment, as well as the efficacy of coupling enzymatic activity to DNA translocation, both diversify the activity of chromatin remodelers (Clapier et al., 2017). With respect to INO80, its modular architecture provides unique means of regulation (sections 2.5.1, 2.5.2 and 2.5.3). As outlined, only a limited number of studies is available for INO80 that address the functional integration of substrate-associated features, such as nucleosome DNA overhang sensing with respect to nucleosome mobilization or the impact of histone tails.

3. Research aim

Significant insights into the mechanism of ISWI-subfamily chromatin remodelers and of the chromatin remodelers RSC and Chd1 have been obtained by single-molecule studies that readout the conformational changes of the nucleosome substrate with FRET and relate FRET efficiency changes back to regulated enzymatic activities (Deindl et al., 2013; Gamarra et al., 2018; Harada et al., 2016; Hwang et al., 2014; Levendosky et al., 2016; Sundaramoorthy et al., 2017; Treutlein, 2012). The overall goal of this thesis is to develop an smFRET assay based on double-labeled nucleosomes to characterize the multi-subunit chromatin remodeler INO80 from *Saccharomyces cerevisiae*.

The first aim of this thesis is to biochemically optimize the catalytic system composed of the 19 subunit *Sc*INO80 complex and the mononucleosome, contributing another 8 proteins and a DNA moiety. With respect to the nucleosome, this includes establishing a reconstitution strategy that yields highly homogenous, labeled nucleosomes. With respect to the *Sc*INO80, an important aspect of this work is to validate its functionality, that is, first, to test nucleosome repositioning (in particular since the purification procedure operated in the group of Prof. Hopfner has been changed to a recombinant expression system) and, second, to optimize the conditions for nucleosome repositioning. A particularly relevant objective is to find appropriate storage conditions for the INO80 complex. In summary, the detailed characterization and optimization of the INO80-nucleosome interplay constitutes a crucial part of this study.

The second aim of this thesis constitutes the establishment of smFRET assays (based on double-labeled nucleosomes) that overcome *ensemble* averaging and therefore infer mechanistic properties of the INO80 complex. In the present thesis, two complementary smFRET techniques are applied to labeled nucleosomes (in the presence or absence of INO80) that monitor either surface-tethered or freely diffusing nucleosomes, respectively. In contrast, previous nucleosome-based smFRET studies of remodelers exclusively rely on near-surface experiments (Deindl et al., 2013; Gamarra et al., 2018; Harada et al., 2016; Hwang et al., 2014; Levendosky et al., 2016; Sundaramoorthy et al., 2017; Treutlein, 2012). Therefore, major parts of this study aim to relate INO80's interplay with tethered nucleosomes (assayed by total internal reflection fluorescence microscopy, TIRFM) to confocal spectroscopy measurements that monitor freely diffusing nucleosomes or nucleosome•INO80 complexes. TIRF microscopy allows observation of a molecule for seconds or tens of seconds, while confocal spectroscopy interrogates a molecule for milliseconds, and a central question is how to exploit both methods best.

The third aim of this thesis is to gain insights into the mechanism of nucleosome remodeling by INO80 with the help of a mutant nucleosome substrate. To this end, nucleosomes that lack all histone tails are compared to wild-type nucleosomes in the context of nucleosome recognition and repositioning. The developed biochemical *ensemble* and smFRET procedures are applied to assay the INO80-nucleosome interplay. This is a promising approach to better understand the function of the INO80 complex on the molecular level, due to the known neat effects of histone tails on nucleosome stability and DNA breathing behavior (Bintu et al., 2012; Brower-Toland et al., 2005; Ferreira et al., 2007b; Iwasaki et al., 2013) and due to their known negative regulatory role in conjunction with INO80 (Udugama et al., 2011). It is expected that histone tails directly or indirectly affect any part of INO80's chemo-mechanical cycle and the objective is to find out more about their role in the context of the INO80-nucleosome interaction.

4. Materials and Methods

All chemicals have been purchased from Merck (Darmstadt, DE or Sigma-Aldrich, now Merck), Carl Roth (Karlsruhe, DE), VWR (Darmstadt, DE) or Thermo Fisher Scientific (Waltham, US-MA or Invitrogen, Life Technologies, now Thermo Fisher Scientific) unless stated otherwise. All buffers have been prepared from deionized or distilled water.

4.1 Molecular cloning and cell biology techniques

4.1.1 *E. coli* and *S. cerevisiae* strains

Escherichia coli (*E. coli*) strains were cultivated for plasmid DNA amplification (*E. coli XL1-blue*) or heterologous protein expression (*E. coli BL21 DE3 or BL21 DE3 star*) in lysogeny broth (LB) medium, containing 0.5 % w/v NaCl, 1 % w/v tryptone, 0.5 % w/v yeast extract (both from Becton, Dickinson & Company), supplemented with 100 µg/ml ampicillin, at 37 °. For purification of endogenous proteins, *S. cerevisiae (INO80-Flag₂)* was cultured in medium containing 2 % w/v peptone, 1 % w/v yeast extract (both from Becton, Dickinson & Company), 2 % w/v glucose, 50 µg/ml ampicillin (facultative), 10 µg/ml tetracycline (facultative), at 30 °.

E. coli and *S. cerevisiae* strains are summarized in Table 1. All media were autoclaved; glucose solution was autoclaved separately and for culture plates 1-2 % w/v agar was added. Bacterial and yeast cell cultures were grown in a shaker (Innova 44 incubator shaker, New Brunswick Scientific, now Eppendorf, Hamburg, DE). *INO80-Flag₂* yeast cell cultures were occasionally grown in a fermenter similar to an established protocol (Tosi, 2013) together with Stefan Benkert, Gene Center and Department of Biochemistry, LMU Munich; the optical density (OD) of yeast cells at 600 nm did not exceed OD 7 upon harvesting the shaking cultures or the fermented cultures.

Cells were harvested by centrifugation (Rotanta 460R, Hettich, Tuttlingen, DE or SLC-6000 rotor, Sorvall Evolution RC Superspeed centrifuge, depending on the scale of the cultures), frozen in liquid nitrogen and stored at -20 ° or -80 °. Yeast cells were washed in INO-lysis/resuspension buffer supplemented with commercially available protease inhibitors before freezing as described (Tosi, 2013) (section 4.2.1 and Table 5). If dedicated for cryogenic grinding (section 4.2.2), yeast cells were instead washed and resuspended with INO-lysis/resuspension buffer without any protease inhibitor and dropped into a liquid nitrogen bath. These droplets were stored at -80 °.

Table 1. List of bacterial and yeast strains.

organism	strain	genotype	obtained from
E. coli	*XL1-blue*	*recA1 endA1 gyrA96 thi-1 hsdR17 supE44 relA1 lac* [*F' proAB lacI^{q}ZΔM15 Tn10(Tet^r)]*	Stratagene, now Agilent (Santa Clara, US-CA)
E. coli	BL21 (DE3) star	*F⁻ ompT hsdS$_B$ (r$_B^-$ m$_B^-$) gal dcm rne131 (DE3)*	Invitrogen, now Thermo Fisher Scientific
E. coli	BL21 (DE3)	*F⁻ ompT hsdS$_B$ (r$_B^-$ m$_B^-$) gal dcm (DE3)*	Novagen, now Merck
S. cerevisiae	INO80-Flag$_2$	MATa INO80-FLAG$_2$ his3Δ200 leu2Δ0 met15Δ0 trp1Δ63 ura3Δ0	laboratory of Xuetong Shen (Shen et al., 2000)

4.1.2 Plasmids and oligonucleotides

Plasmids used for DNA amplification and protein expression are listed below (Table 3). Globular histones that lack histone tails have been cloned, purified and provided by Kevin Schall, Gene Center and Department of Biochemistry, LMU Munich and are therefore not listed. The protein sequence of the wild-type and all tailless histones can be found in the appendix 12.1.

Oligonucleotides are listed in Table 2. Some labeled primers (Table 2) have been designed for nucleosome-based smFRET by Barbara Treutlein, Institute of Biophysics, Ulm University (Sundaramoorthy et al., 2017; Treutlein, 2012), or are derived from similar primers that have been designed in the same studies (Sundaramoorthy et al., 2017; Treutlein, 2012). Internal dyes were attached to a thymine nucleobase via a flexible C6 linker by the manufacturer (Table 2). The sequence for the primers dedicated to the 147 bp competitor DNA (crDNA) amplification was provided by Dr. Andrew Routh.

The DNA sequence of the 147 bp crDNA and of the 200 bp 601-seq DNA as well as of the 220 bp 601-seq DNA can be found in the appendix 12.1 and in Figure 12, respectively. The 147 bp crDNA and the 200 bp 601-seq DNA were of use for the nucleosome assembly protocols described in section 4.3.2. Assays with INO80 rely on nucleosomes assembled from the 220 bp 601-seq DNA.

Table 2. List of oligonucleotides to modify or to amplify the 220 bp 601-seq or the 147 bp crDNA.

(Bio) denotes 5'-terminal biotin modification, (Cy5) or (Cy3) denote the respective individual 5'-terminal labeling, highlighted nucleotides are labeled with Alexa647 (red) or Tamra6 (green). Bold letters are sites designed for restriction enzymes. Oligonucleotides were labeled (dyes), modified (biotin) and purified (desalted, <u>p</u>oly<u>a</u>crylamide <u>g</u>el <u>e</u>lectrophoresis (PAGE) purified or <u>h</u>igh <u>p</u>ressure <u>l</u>iquid <u>c</u>hromatography (HPLC) purified) by the manufacturer.

name	5'-3'-sequence	purpose/ purity	obtained from
220bp_version2_fw_mod	GCG**AAGCTT**CCTGGAGAATCCCGGTGC	modi-fication/ desalted	Metabion (Martins-ried, DE)
220bp_version2_rv1_mod	TATCCGACTGGCACCGGCAAGGTCGCTGTTCAATACATGCAC		
220bp_version2_rv2_mod	GCCGC**GAATTC**TCTAGAGTGGGAGCTCGGAACACTATCCGACTGGCACCGGCAAG		
220bp_version2_fw	GGCCGCCCTGGAGAATCCCGGTGCCGAGGC	preparative ampli-fication/ desalted	
601competitor_fw	ATTCATTAATGCAGCTGGCACGACAGG		
601competitor_rv	GCTCACAATTCCACACAACATACGCGCC		
220bp_version2_rv_Cy5	(Cy5)TCCTCTAGAGTGGGAGCTCGGAACAC	preparative ampli-fication/ HPLC purified	
601competitor_rv_Cy3	(Cy3)GCTCACAATTCCACACAACATACGCGCC		
R-84A647_220bp_bio	(Bio)TCCTCTAGAGTGGGAGCTCGGAACACTATCCGACTGGCACCGGCAAGGTCGCTGTTCAATAC	ampli-fication for smFRET/ PAGE purified	IBA (Göttin-gen, DE)
F+13TMR	GGCCGCCCTGGAGAATCCCGGTGCCGAGGCCGCTCAATTGGTCGTAGCAAGCTCTAGCACCGCTTAAACGCACGTACGCGCTGTCCCCCGCGTTTTAACC		
F-72A647F+13TMR	GGCCGCCCTGGAGAATCCCGGTGCCGAGGCCGCTCAATTGGTCGTAGCAAGCTCTAGCACCGCTTAAACGCACGTACGCGCTGTCCCCCGCGTTTTAACC		
F-65A647F+13TMR	GGCCGCCCTGGAGAATCCCGGTGCCGAGGCCGCTCAATTGGTCGTAGCAAGCTCTAGCACCGCTTAAACGCACGTACGCGCTGTCCCCCGCGTTTTAACC		
R_220bp_bio	(Bio)TCCTCTAGAGTGGGAGCTCGGAACACTATCCGACTGGCACCGGCAAGGTCGCTGTTCAATAC	ampli-fication for smFRET/ HPLC purified	Sigma-Aldrich, now Merck

Table 3. List of plamids.
These plasmids convey ampicillin resistance, which was used for positive selection.

name	vector backbone	Insert	obtained from
pet21a::H2A	pet21a	*Hs*H2A	laboratory of Prof. G. Längst, University of Regensburg (Hoffmeister et al., 2017)
pet21a::H2B	pet21a	*Hs*H2B	
pet21a::H3	pet21a	*Hs*H3	
pet21a::H4	pet21a	*Hs*H4	
pUC18::12x200bp-601	pUC18	12 repeats of a 200 bp 601-seq fragment	
pMA::M220 bp-601	pMA	modified 220 bp 601-seq fragment	GeneArt AG (Life technologies)
pMA::220 bp-601	pMA	220 bp 601-seq fragment	derivative of pMA::M220 bp-601 (this study)

4.1.3   DNA modification and amplification techniques

DNA manipulation and amplification was performed following standard protocols of molecular cloning (Green and Sambrook, 2012). Commercially available kits and devices used to this end are indicated for the respective techniques and have been used according to the manufacturer's instruction. Restriction enzymes and polymerases have been applied using the reaction conditions recommended by the manufacturer. Specific sample treatment is indicated separately.

Plasmid DNA was amplified in *E. coli XL1-blue* cells. The plasmid DNA was introduced into competent *E. coli* cells according to standard procedures (Hanahan et al., 1991). Competent *E. coli* cells were stored at -80 ° and their competence for transformation had been induced chemically beforehand. Plasmid DNA (5-100 ng) was added to ca. 100 µl cell suspension; *E. coli* cells were then incubated on ice for 10 min, treated with a heat-shock at 43 ° for 45 s and incubated another 3 min on ice. *E. coli* cells recovered in LB medium while gently shaking in a thermo-mixer (Eppendorf, Hamburg, DE) at 37 °and were then transferred onto an LB culture plate containing ampicillin to select for transformed clones (section 4.1.1 and 4.1.2). This procedure also applies to the introduction of histone expression plasmids in *E. coli BL21 (DE3)* or *E. coli BL21 (DE3) star* cells.

E. coli XL1-blue cells were cultivated over night and harvested (section 4.1.1). Plasmid DNA was isolated with the NucleoSpin Plasmid Quick Pure Kit (Macherey-Nagel, Düren, DE) or the Spin Miniprep Kit (Qiagen, Hilden, DE).

The pMA::220 bp-601 was derived from the pMA::M220 bp-601 (Table 2 and Table 3). The pMA::M220 bp-601 was linearized (EcoRI-HF, New England Biolabs, NEB, Frankfurt, DE) to serve as a PCR-template (as outlined below) and the new insert was derived by two subsequent polymerase chain reactions (PCRs) using Phusion high-fidelity DNA polymerase (NEB) and the primers for 601-seq modification listed in (Table 2). Both, insert and vector backbone were digested with EcoRI-HF and HindIII (NEB) and the vector backbone was treated with fast alkaline phosphatase (Fermentas, now Thermo Fisher Scientific). Subsequently, preparative agarose gel electrophoresis of insert and backbone (section 4.1.4) and purification with the Gel and PCR Clean-up Kit (Macherey-Nagel, Düren, DE) was performed. The newly derived insert and the vector backbone were ligated with T4 DNA Ligase (Fermentas, now Thermo Fisher Scientific) and the ligation product was introduced in *E.coli XL-1 blue* by transformation.

pUC18::12x200bp-601 and pMA::220 bp-601 were each digested (linearized) with EcoRI-HF (NEB) to generate a template for the 147 crDNA amplification or the 601-seq amplification by PCR, respectively. pUC18::12x200bp-601 subsequently was digested with Not1-HF (NEB) over night to yield 12 separate repeats of the 601-seq alongside with the vector backbone.

601-seq DNA and 147 bp DNA were amplified by PCR. The 601-seq DNA was amplified using the linearized pMA::220 bp-601 as a template. Double-labeled nucleosomal DNA for the three smFRET-constructs (Figure 12) was amplified with Q5 DNA polymerase (NEB) and the primers F+13TMR and R-84A647_220bp_bio, F-72A647F+13TMR and R_220bp_bio, F-65A647F+13TMR and R_220bp_bio (Table 2), respectively. Preparative amplification of the terminally labeled 601-seq DNA was achieved by two subsequent PCRs with Taq DNA polymerase (NEB), using the linearized pMA::220 bp-601 as a template for the first PCR and its product as a template for the second PCR. Preparative amplification of the terminally labeled or unlabeled 147 bp crDNA was also accomplished by two subsequent PCRs, using Phusion polymerase (NEB) and the linearized pUC18::12x200bp-601 template in the first round. Its product served as template for Taq polymerase (NEB) amplification in the second round.

Digested plasmid DNA and PCR amplified samples were purified with the Gel and PCR Clean-up Kit (Macherey-Nagel) or the PCR Purification Kit (Qiagen, Hilden, DE) prior to further usage. The optional pH indicator provided separately in the kits was omitted for the preparation of FRET probes.

The double labeled nucleosomal DNA was purified by ethanol precipitation (Green and Sambrook, 2012) and size exclusion chromatography (SEC) according to an established procedure (Treutlein, 2012). Briefly, size exclusion chromatography was performed in 20 mM Tris(hydroxymethyl)-aminomethane (Tris) pH 8, 100 mM NaCl, 1 mM ethylenediaminetetraacetic acid (EDTA), using a Superose 6 PC 3.2/30 column (GE Healthcare, Freiburg, DE).

Purified DNA was concentrated with Amicon Ultra Centrifugal Filter Units (molecular weight cut-off 10 kDA, Merck Millipore, now Merck) if necessary. Table centrifuges (Eppendorf, Hamburg, DE) were used for the centrifugation steps described in this section.

4.1.4 Analytic assessment of DNA

In general, the analytic assessment of DNA as described in this section was performed following standard protocols (Green and Sambrook, 2012).

The intermediate products of the plasmid and the insert generated in the course of molecular cloning to modify the pMA::M220 bp-601 plasmid (section 4.1.3) and DNA plasmids that have been digested with a single restriction enzyme to generate a linear PCR template were analyzed on a 1 % agarose gel (data not shown). Agarose gels were supplemented with a DNA intercalator (GelRed, Biotium, Fremont, US-CA) and were run in a horizontal gel chamber (Bio Rad) in 1xTris Acetate EDTA (1xTAE) running buffer.

Plasmid DNA isolated from *E. coli XL-1 blue* cells (section 4.1.3) was sequenced by GATC Biotech (now Eurofins, Luxemburg, LU) or MWG Biotech (Ebersberg, DE), if required.

The 601-seq fragments generated by endonucleolytic digestion from the pUC18::12x200bp-601, the PCR amplified 601-seq, the PCR amplified 147 bp crDNA and the SEC-purified double-labeled 601-seq DNA were all analyzed on a 6 %

polyacrylamide (PAA) gel (1xTBE) (Table 4). Mononucleosomes were analyzed in the same way, with minor modifications (6 % PAA gel, 0.4xTBE, Table 4).

PAA gels were run in a vertical gel chamber (Bio Rad) in the respective TBE running buffer (Table 4). PAA gels were first imaged for the respective fluorescent label on the probes and subsequently stained in SYBRGold or SYBRGreen staining solutions, followed by two washing steps in water or in the respective TBE buffer (Table 4) and then imaged again. To estimate DNA size a 100 bp DNA Ladder, a 2-Log DNA Ladder (both NEB) or a GeneRuler (100 bp Plus DNA Ladder, Fermentas, now Thermo Fisher Scientific) were applied in a separate well on 6 % PAA gels.

Table 4. Buffers and gels used for analytic assessment of 601-seq DNA and of mononucleosomes.

name	composition or manufacturer	PAGE of
8x Ficoll loading solution	Ficoll solution Type 400, 20 % in water, Sigma-Aldrich, now Merck	mononucleosomes/ 601-seq DNA
1 x TBE running buffer	89 mM Tris base, 89 mM boric acid, 2 mM EDTA	601-seq DNA, 147 bp crDNA
0.4 x TBE running buffer	36 mM Tris base, 36 mM boric acid, 0.8 mM EDTA	mononucleosomes
6 % PAA, 1 x TBE gel	1 x TBE, 6 % acrylamide (diluted from Rotiphorese Gel, 30 % solution, 37.5:1 with bisacrylamide), 0.09 % w/v Ammonium-Persulfat (APS), 0.09 % v/v Tetramethylethylendiamin (TEMED)	601-seq DNA, 147 bp crDNA cast in-house
6 % PAA, 0.4 x TBE gel (alternatively 0.5xTBE)	0.4 x TBE, 6 % acrylamide (diluted from Rotiphorese Gel, 30 % solution, 37.5:1 with bisacrylamide), 0.09 % w/v APS, 0.09 % v/v TEMED	mononucleosomes cast in-house
SYBRGreen I nucleic acid gel staining solution	1:5000 in 0.5 x TBE or water Invitrogen, Life Technologies, now Thermo Fisher Scientific	mononucleosomes/ 601-seq DNA, 147 bp crDNA
SybrGold nucleic acid gel staining solution	1:10 000 in water Invitrogen, now Thermo Fisher Scientific	mononucleosomes/ 601-seq DNA, 147 bp crDNA

Gels were imaged either on a ChemiDocMP system (BioRad), or with a Typhoon FLA 9000 scanner (GE Healthcare), or with an INTAS UV System for gel documentation (Intas-Science-Imaging Instruments, Göttingen, DE), as indicated.

DNA concentrations and DNA-protein complex concentrations were estimated from the absorption at 260 nm, using a NanoDrop Instrument (peqlab NanoDrop 1000 or 2000, Thermo Fisher Scientific) or a NanoPhotometer Instrument (Implen, Munich, DE). In the latter case, measured concentrations are termed 'DNA equivalent'.

4.2 Protein purification techniques

4.2.1 List of buffers used for protein purification

Table 5. Buffers used for cell lysis and protein purification of recombinantly expressed histones and of endogenous INO80.

Components in brackets denote buffer components that are changed in the course of the respective chromatographic step, that is to say that both high and low salt buffers were used to establish an ion gradient for ion exchange chromatography. Further, elution of INO80 from the FLAG resin was performed in low salt buffer, reducing the salt concentration when washing the FLAG resin (Tosi, 2013). Buffer compositions for histone purification and octamer assembly as well as for INO80 purification are taken from published protocols (Haas, 2013; Klinker et al., 2014) and (Tosi, 2013; Tosi et al., 2013).

name	composition	application
histo-SAU buffer	8 M urea, 40 mM sodium acetate pH 5.2, 1 mM EDTA, 5 mM β-mercaptoethanol, 10 mM lysine, 200 mM NaCl (1 M NaCl)	cell lysis cation exchange chromatography
histo-anion exchange buffer	15 mM Tris pH 8, (2 M NaCl)	anion exchange chromatography
oct-unfolding buffer	7 M guanidin hydrochlorid, 20 mM Tris pH 7.5, 10 mM DTT	protein unfolding
oct-refolding/SEC buffer	2 M NaCl, 10 mM Tris pH 7.5, 1 mM EDTA, 5 mM β-mercaptoethanol	protein refolding size exclusion chromatography
INO-lysis/resuspension buffer	25 mM HEPES pH 8.0, 10 % v/v glycerol, 0.05 % v/v NP40 (IGEPAL, Sigma-Aldrich, now Merck), 1 mM EDTA, 1 mM DTT, 4 mM MgCl$_2$, 500 mM KCl	cell lysis
INO-affinity chromatography buffer	25 mM (30 mM) HEPES pH 8.0, 10 % v/v glycerol, 0.05 % v/v NP40, 1 mM EDTA (no EDTA), 1 mM DTT, 4 mM MgCl$_2$, 500 mM KCl (200 mM KCl)	FLAG affinity chromatography
INO-anion exchange buffer	25 mM HEPES pH 8.0, 7 % glycerol, 1 mM DTT, 4 mM MgCl$_2$, 200 mM KCl (1 M KCl)	anion exchange chromatography

4.2.2 Protein purification of INO80, histones and histone octamers

Each histone was heterologously expressed in *E. coli BL21 (DE3)* or *E. coli BL21 (DE3) star* cell cultures from a pET21a plasmid (Novagen, now Merck) (sections 4.1.1, 4.1.2 and 4.1.3, Table 1 and Table 3) based on an expression system developed in the eighties and nineties (Dubendorff and Studier, 1991; Studier and Moffatt, 1986; Studier et al., 1990). When the cell culture reached an OD (measured at 600 nm) of at the most 0.6, addition of isopropyl-β-D-1-thiogalactopyranoside (IPTG) with a final concentration of 0.25 mM induced histone expression for 2 h until cells were harvested (section 4.1.1). Histone expression was performed similar to recent protocols (Hoffmeister et al., 2017; Klinker et al., 2014).

Histone purification essentially followed a published protocol (Haas, 2013; Klinker et al., 2014); only its main steps and altered steps as applied for purifications performed in this study are described in detail in the following. Cells were disrupted by sonication (Sonifier 250, Branson, Emerson, St. Louis, US-MO) in denaturing buffer conditions (Table 5; here 200 mM NaCl) and the insoluble cell debris was separated from the soluble part by centrifugation (SS-34 rotor, Sorvall Evolution RC Superspeed centrifuge). Histones were applied to a cation exchange column (HiTrap SP, GE Healthcare) in denaturing conditions (Table 5). After refolding during dialysis (ZelluTrans membrane dialysis tube, Carl-Roth, molecular weight cut-off 3.5 kDa) against water, the sample was buffered with 15 mM Tris (pH 8) and anion exchange chromatography was performed (HiTrap Q, GE Healthcare). In this step, the histone proteins are positively charged at the near neutral pH of the mobile phase and virtually do not interact with the resin; however, residual DNA can be removed (Klinker et al., 2014). For storage, histones have been flash-frozen in liquid nitrogen and subsequently lyophilized.

Particularly alike-purified histone H4 revealed smaller proteins alongside with the desired product, presumably due to H4 degradation that was not negligible (data not shown), while other histones were largely pure (section 5.1.2). This wasn't addressed further, as after subsequent histone octamer assembly and histone octamer purification, these contaminants were no longer observed (section 5.1.2). While I performed histone purification and octamer assembly as presented in section 5.1.2, most histones and the respective histone octamers used for the smFRET experiments (section 5.2) were purified by Kevin Schall, Gene Center and Department of Biochemistry, LMU Munich. Histone purification featured equivalent steps as outlined above, with an improvement in including an inclusion body formation step (Dyer et al., 2003; Hoffmeister et al., 2017;

Schwarz et al., 2018). Alike-purified histone H4 was mostly devoid of degradation side-products in initial purification steps (data not shown). Wild-type octamers assembled from these histones were used for direct comparison with all-tailless histone octamers in functional assays (section 5.2). Kevin Schall also provided the all-tailless octamer construct.

Octamer formation as performed in this study followed the published protocols (Dyer et al., 2003; Klinker et al., 2014). An excess of histones H2A/H2B over histones H3/H4 was used when mixing all four core histones and unfolding them for 2-3 h at room temperature (RT). Octamers formed upon refolding during dialysis (ZelluTrans membrane dialysis tube, molecular weight cut-off 3500 Da) against oct-refolding/SEC buffer (unfolding and refolding buffer in Table 5); dialysis was performed for 18-20 h including 3x buffer exchange. The sample was concentrated in Amicon Ultra Centrifugal Filter Units (molecular weight cut-off 10 kDA, Merck Millipore, now Merck; centrifuge Rotanta 460R with a 4-place swing-out rotor, Hettich, Bäch, CH, or table centrifuge, Eppendorf). Prior to SEC, the sample was centrifuged in a table centrifuge for at least 10 min to remove potential aggregates. SEC was performed using a HiLoad 16/60 Superdex 200 prepgrade column (GE Healthcare). The collected fractions were analyzed by sodium dodecyl sulfate polyacrylamide gel electrophoresis (SDS-PAGE, section 4.2.3) and fractions containing histones in equimolar ratio were pooled and concentrated as described above. An amount of 100 % glycerol equivalent to the volume of the purified histone octamers was added and after gentle mixing, histone octamers were stored at -20 ° in 50 % v/v glycerol. In general, all protein purification steps were performed at 4 °, unless specified otherwise, and all chromatographic steps using columns were performed automatically with the help of ÄKTA systems (ÄKTAbasic, ÄKTAFPLC, ÄKTApurifier, ÄKTAexplorer, ÄKTAmicro, all GE Healthcare).

INO80 was purified endogenously from yeast as published in Tosi (2013) and Tosi et al. (2013); only the major steps of the aforementioned protocol for isolating INO80 as performed in this study are stated in the following. Cells were lysed in INO-lysis/resuspension buffer (Table 5; supplemented with commercially available protease inhibitors) using bead-beaters. This treatment required direct processing of the cell lysate. Alternatively, cells were lysed using a cryogenic grinder cooled with liquid nitrogen (Freezer Mill, SPEX SamplePrep, Metuchen, US-NJ). These grinded cells were stored at -80 °.

Chromatin was fragmented within the lysate mechanically as described (Tosi, 2013). The cell debris was removed by two centrifugation steps (SLA-1500 rotor, Sorvall Evolution RC Superspeed centrifuge and Ti45 rotor, Beckman Coulter Ultracentrifuge, Brea, US-CA). The supernatant, excluding the topmost layer, which formed a separate phase upon ultracentrifugation, was used for batch FLAG affinity purification. A clearing step elaborated in Tosi (2013) that involves batch incubation with Protein G Sepharose to remove unspecificly binding components of the lysate preceded the incubation with FLAG-beads (M2 FLAG-beads, Sigma-Aldrich, now Merck) and the FLAG affinity purification was performed as described (Tosi, 2013). As a final purification step, the eluate from the affinity chromatography was applied to an anion exchange column (MonoQ 5/50 GL, GE Healthcare) at RT. When applying a KCl salt gradient during anion exchange chromatography (buffers summarized in Table 5), the INO80 complex elutes at approximately 440 mM KCl.

The eluate containing pure INO80 was adjusted to final buffer concentrations of 20 mM HEPES pH 8, 350 mM KCl, 25 % glycerol, 0.8 mM DTT, 3.2 mM $MgCl_2$. This was achieved by addition of an amount of 100 % glycerol equivalent to 1/4th of the volume of the INO80 anion exchange eluate. After gentle mixing, INO80 was flash-frozen in liquid nitrogen and stored at -80° C (section 5.1.1). Refreezing after thawing was only performed once, if required.

4.2.3 Analytic assessment of proteins

SDS-PAGE analysis (Laemmli, 1970) was applied to all histone protein purification steps. Gels were cast in the format of the PROTEAN Electrophoresis System (Biorad), which was used to perform electrophoresis. Gradient PAGE was performed in denaturing conditions at near neutral pH (Moos et al., 1988) according to the manufacturer's instructions (Table 6) and was executed in the respective MiniCell gel chamber (Invitrogen, Life Technologies, now Thermo Fisher Scientific).

For SDS-PAGE (including denaturing gradient PAGE), protein samples were prepared in 1 x SDS loading buffer (Table 6) and heated at 95 ° for at least 10 min (Laemmli, 1970); samples of *E. coli* cell cultures were dissolved in urea sample buffer (Table 6) and heated for at least 10 min at 65 ° (Klinker et al., 2014). In order to estimate the size of the proteins as revealed by gel electrophoresis, a molecular weight marker (Unstained Protein Ladder, Unstained Protein Molecular Weight Marker, Thermo Fisher Scientific) was also

resolved. The *Drosophila melanogaster* (*Dm*) octamer molecular weight marker was provided by Dr. Caroline Haas.

For analyzing proteins in non-denaturing conditions (native PAGE), its charge and size are decisive for its electrophoretic mobility (Arndt et al., 2012). A native PAGE (3-12 %, Table 6) was assembled in a MiniCell with native PAGE running buffer (all Invitrogen, Life Technologies, now Thermo Fisher Scientific) to analyze INO80 (theoretical isoelectric point 5.23) or the INO80-nucleosome complex by electrophoresis at near neutral pH and at 4 °. The samples were loaded in the presence of 2.5 % Ficoll (Table 6). For comparison between different preparations, the NativeMark Unstained Protein Standard (Invitrogen, Life Technologies, now Thermo Fisher Scientific) was applied to each native PAGE. This protocol was also suitable to assess nucleosome samples that have been treated with INO80 (sections 4.4.1 and 4.4.2). The described procedure is a notable departure from the manufacturer's protocol.

All protein gels were stained with Coomassie staining solution at RT or SimplyBlue SafeStain according to the manufacturer's instruction (Table 6). Protein gels were destained in water and digitized using a scanner (Epson Perfection, Epson, Amsterdam, NL).

All protein concentrations were derived from the absorption at 280 nm that was determined with a NanoDrop (Thermo Fisher Scientific) or a NanoPhotometer (Implen). The extinction coefficient and the theoretical isoelectric point of proteins and protein complexes were calculated using the ExPASy ProtParam software (Gasteiger et al., 2005).

Table 6. Buffers and gels used for analytic assessment of protein samples.
X-fold buffers have been diluted accordingly.

name	composition/ manufacturer	application
4x SDS loading buffer	110 mM Tris pH 6.8, 16 % glycerol, 4 % SDS, 5 % β-mercaptoethanol, supplemented with bromphenolblue	SDS-PAGE (18 %) and SDS-PAGE (4-12 %)
urea sample buffer (Klinker et al., 2014)	9 M urea, 1 % SDS, 25 mM Tris pH 6.8, 1 mM EDTA, 100 mM DTT, supplemented with bromphenolblue	SDS-PAGE (18 %)
6x native loading buffer	20 mM Tris pH 7.6, 50 mM NaCl or KCl, 0.1 mM EDTA (facultative), 15 % w/v Ficoll	Native PAGE
1x TGS running buffer	25 mM Tris, 192 mM glycine, 0.1 % SDS	SDS-PAGE (18 %)
1x MOPS running buffer	20 x NuPAGE MOPS SDS running buffer (Invitrogen, Life Technologies, now Thermo Fisher Scientific)	SDS-PAGE (4-12 %)
1x NativePAGE running buffer	20x NativePAGE Running Buffer (Invitrogen, Life Technologies, now Thermo Fisher Scientific)	Native PAGE
stacking gel	125 mM Tris pH 6.8, 0.1 % SDS, 3.8 % acrylamide (diluted from Rotiphorese Gel, 30 % solution, 37.5:1 with bisacrylamide), 0.1 % w/v APS, 0.1 % v/v TEMED	SDS-PAGE (18 %) cast in-house
separating gel	750 mM Tris pH 8.5, 0.1 % SDS, 18 % acrylamide (diluted from Rotiphorese Gel, 30 % solution, 37.5:1 with bisacrylamide), 0.07 % w/v APS, 0.05 % v/v TEMED	
SDS-PAGE (4-12 %)	NuPAGE (4-12 %) Bis-Tris Protein Gel (precast, Invitrogen, Life Technologies, now Thermo Fisher Scientific)	SDS-PAGE (4-12 %)
Native-PAGE (3-12 %)	3-12 % NativePAGE Bis-Tris Protein Gel (Invitrogen, Life Technologies, now Thermo Fisher Scientific)	Native PAGE
Coomassie staining solution	7 % v/v acetic acid, 50 % v/v ethanol, 0.2 % w/v Coomassie brilliant blue R250	SDS-PAGE (18 %) and SDS-PAGE (4-12 %)
SimplyBlue SafeStain	Invitrogen, Life Technologies, now Thermo Fisher Scientific	SDS-PAGE (18 %), SDS-PAGE (4-12 %) and native PAGE

4.3 DNA-protein complex formation techniques

4.3.1 List of buffers used for nucleosome assembly

Table 7. Buffers used for mononucleosome assembly.
Buffers and gels used for analytic assessment of mononucleosomes are listed in Table 4.

name	composition	application
mono-low salt	20 mM Tris pH 7.6, 0.1 mM EDTA, 50 mM NaCl, 1 mM DTT	low salt buffer reservoir
mono-high salt	20 mM Tris pH 7.6, 0.1 mM EDTA, 2 M NaCl, 1 mM DTT	high salt buffer reservoir
mono-mix	20mM Tris pH 7.6, 2 M NaCl, 10 mM DTT, 200 ng/µl BSA	titration mixture

4.3.2 Nucleosomes dedicated to *ensemble* and single-molecule applications

In-vitro, the stoichiometry (octamer vs. DNA) of the nucleosome packing is ensured by preparing different molar octamer-to-DNA ratios when forming mononucleosomes (Dyer et al., 2003) or even chromatin fibers (Huynh et al., 2005). Salt gradient dialysis of these reaction mixtures is a standard procedure for nucleosome and for chromatin fiber assembly *in vitro* as this mimics the stepwise *in vivo* assembly mechanism assisted by chaperones (Akey and Luger, 2003): first the H3/H4 tetramer associates with DNA, onto which two H2A/B dimers pack (Dyer et al., 2003; Huynh et al., 2005).

In order to assemble nucleosomes dedicated to *ensemble* applications, in equimolar mixture of 147 bp crDNA and 220 bp 601-seq DNA, 0.42 µM each, were titrated with different molar ratios of histone octamers (referenced to the 220 bp 601-seq DNA concentration) in mono-mix buffer (Table 7).

For nucleosomes dedicated to single-molecule applications, the backbone of the pUC18::12x200bp-601 plasmid was used as crDNA in a mass ratio of 1:1 with reference to the total mass of 601-seq DNA. The plasmid backbone is prepared in conjunction with unlabeled 601-seq DNA that can form 7N46 nucleosomes (sticky end DNA nucleosomes, section 4.1.3, appendix 12.1). In total, the reaction mixture contained approximately 0.38 µM 601-seq DNA, thereof 1/10 labeled 220 bp 601-seq nucleosomal DNA and 9/10 unlabeled 601-seq. This unlabeled 200 bp 601-seq constitutes the 601-seq derived from endonucleolytic pUC18::12x200bp-601 digestion and has been prepared together with the crDNA vector backbone. The DNA was prepared in mono-mix buffer (Table 7) and histone octamers were added in different molar ratios (referenced to the total 601-seq

DNA concentration). This protocol is based on a nucleosome assembly procedure that has been described earlier (Treutlein, 2012), with minor modifications.

The reaction mixture was transferred to Slide-a-lyzer MINI dialysis devices (Thermo Fisher Scientific, Waltham, US-MA, 7-kDa molecular weight cut-off) and a salt gradient dialysis, starting with dialysis against 300 ml mono-high salt buffer, was performed at 4 °. The salt concentration was gradually reduced by adding mono-low salt buffer at 3 ml/min up to a final volume of 3 l using a membrane pump or a peristaltic pump (Pump P-50, Pharmazia Biotech; Minipuls3 Gilson, Middleton, US-WI). Nucleosomes were finally dialyzed against mono-low salt buffer and stored at 4 °.

Nucleosomes were analyzed by native PAGE at 4 °, as described in section 4.1.4. For nucleosome samples, approx. 350-400 ng DNA equivalents were applied to each well. For DNA samples (220 bp 601-seq DNA or 601-seq DNA mixed with crDNA) between 20 ng and 40 ng (with reference to the labeled DNA) were used. Generally, DNA samples were brighter than nucleosome samples in native PAGE fluorescence readouts. That is to say that nucleosome packing was assessed by the nucleosome by-product formation of under- and over-titrated nucleosome samples, as described in sections 5.1.3 and 5.1.6, rather than by comparing nucleosome probes to the DNA only probes. Gel representation and analysis is described in section 4.5.

4.4 Biochemical characterization of INO80

4.4.1 Electrophoretic mobility shift assays

The electrophoretic mobility shift assays (EMSA) presented in section 5.1.4 was performed in 25 mM HEPES pH 8.0, 7 % glycerol, 1 mM DTT, 4 mM $MgCl_2$, 200 mM KCl (taking the KCl introduced by the INO80 sample into account) in the absence of nucleotides with 7N66 nucleosomes containing approximately equimolar amounts of 147 bp crDNA (21 ng/µl DNA equivalents).

The EMSA presented in section 5.1.5 was performed in 20 mM HEPES pH 8, 50 mM KCl, 8 % glycerol, 2 mM $CaCl_2$ and 2 mM Adenosine diphosphate (ADP) with 15 nM 7N66 nucleosomes labeled with Fluorescein (instead of Cy5, other than in Table 2). Nucleosomes have been purified with a SourceQ column (GE Healthcare) to remove free DNA. Kevin Schall, Gene Center and Department of Biochemistry, LMU Munich, prepared these nucleosomes and the technical triplicates of the EMSA.

Each reaction mixture with the indicated amount of INO80 was incubated on ice for at least 20 min. The samples were then applied to a native PAGE (3-12 % PAA, Table 6) as described in section 4.2.3 and imaged with the Typhoon scanner (section 4.1.4). If required, the gel was then stained with SybrGreen staining solution in water (Table 4) and imaged with the INTAS gel documentation system (section 4.1.4). Quantification is described in section 4.5.

After quantification of the EMSA, the data were fitted with a curve that represents the fraction of bound nucleosomes (section 5.1.5) (MATLAB Curve Fitting Toolbox, Equation 1). Here, I_t is the total INO80 concentration, K_d is the dissociation constant (to be fitted) and N_t is the total nucleosome concentration (15 nM). Assuming that this fit model represents the underlying INO80-nucleosome binding properties (section 5.1.5), K_d for wild-type nucleosomes was between 1.7 nM and 2.6 nM and K_d for all tailless nucleosomes was between 1.9 nM and 3.8 nM (determined from the fit with 95 % confidence bounds).

$$fraction\ of\ bound\ nucleosomes =$$

$$= \frac{1}{2N_t} \cdot \left[(I_t + N_t + K_d) - \sqrt{(I_t + N_t + K_d)^2 - (4 \cdot I_t \cdot N_t)} \right]$$

Equation 1

4.4.2   Nucleosome sliding assays

The time-dependent nucleosome sliding assays contained nucleosomes in the presence of 147 bp crDNA (7-7.5 ng/µl DNA equivalents), 50 nM INO80, 500 µM DTT, 2 mM ATP, 0.5 µM nanobody (if indicated), 25 mM Tris pH 7.6, 4 mM MgCl$_2$, 200 ng/µl BSA, 80 mM KCl, 10 % glycerol and were performed at 23 °.

0.5-0.6 µM INO80, 5-6 µM nanobody and 2 mM ATP were incubated on ice. Nucleosomes were prepared in sliding buffer. The reaction was started by mixing (final concentrations given above) and stopped by addition of λ-DNA (NEB; final concentration 100 ng/µl) at the time points indicated. The reaction mixture was then kept on ice and applied to native PAGE (6 % PAA, 0.5xTBE, Table 4) as described in section 4.1.4. Kilian Knoll, Gene Center and Department of Biochemistry, LMU Munich, provided the purified nanobody.

The direct comparison of INO80 remodeling in the absence vs. the presence of the nanobody reports on potential differences in remodeling activity. Both nucleosome binding and remodeling by INO80 deliberately contribute to the apparent time needed for nucleosome sliding. It is assumed that the association rates for INO80-crDNA binding and INO80-nucleosome binding, as well as the concomitant total affinities, are not altered in the absence vs. the presence of the nanobody, as the concurring binding of INO80 to 147 bp crDNA (instead of nucleosomes) withdraws INO80 complexes from being active in remodeling at any given point in time.

The INO80-concentration-dependent nucleosome sliding assays contained nucleosomes in the presence of 147 bp crDNA (7.5 ng/µl DNA equivalents), 1 mM DTT, 2 mM ATP, 25 mM Tris pH 7.6, 4 mM $MgCl_2$, 80 mM KCl (or 50 mM NaCl in Figure 4), 10 % glycerol. Reactions were incubated on ice for 25 min and started by the addition of ATP. The remodeling mixture was incubated at 30 ° for 30 min, transferred to 4 ° and then analyzed by native PAGE (6 % PAA, 0.5xTBE, Table 4) as described in section 4.1.4.

4.5   Representation of analytic gels

Gels read out for fluorescent bands with the ChemiDocMP system (section 4.1.4) were acquired with the Image Lab software (BioRad). Gels read out for fluorescent bands with the Typhoon scanner (section 4.1.4) were converted to .tif files with the ImageQuant software (GE Healthcare) and displayed with ImageJ (Schneider et al., 2012). The maximum and minimum intensity of each gel was set to an adequate value (brightness and contrast adjustment) with the Image Lab software or with ImageJ, respectively, for data representation. The greyscale of single-channel fluorescence readouts was inverted for better visualization. Bands were quantified and profile plots were generated in ImageJ, using the gel quantification and profile plot plugins of the original software package, respectively. Profile plots were not normalized or corrected for background and are displayed "as is". For quantified assays, the standard deviation of technical triplicates is displayed. The INTAS gel documentation system (section 4.1.4) generated a color image as a gel readout, which was converted to greyscale using ImageJ (serving also for brightness and contrast adjustment). Signal saturation cannot be assessed for these gels.

All gels were annotated using Adobe Illustrator (Adobe Systems, US-CA).

4.6 Microscopy Techniques

4.6.1 TIRF microscopy

Functional assays were performed at RT in a sample flow chamber that was illuminated by prism-type total internal reflection (green Nd:YAG laser, 532 nm, ca. 12 mW in front of the prism and red diode laser, 643 nm, ca. 1 mW in front of the prism). The TIRF microscopy setup has been home-built at the Institute of Biophysics, Ulm University, and is described in detail elsewhere (Dörfler et al., 2017). Of note, the fluorescence detection pathway was split into a donor and acceptor channel and green and red fluorescence were detected by two separate electron multiplying charge-coupled device (EM-CCD) cameras (Andor Technology, Belfast, UK) operated with an integration time (time bin) of 105 ms. An integration time of 33 ms was used if indicated separately. In this case, the power of the illuminating laser light was increased to approximately 32 mW (532 nm) and 2.5 mW (643 nm) in front of the prism, respectively. All measurements were conducted using the alternating-laser excitation (ALEX) scheme (direct acceptor excitation every second time bin) during data acquisition (Hohlbein et al., 2014; Margeat et al., 2006). Alternating red and green illumination times were controlled by an acousto-optical tunable filter (AOTF), setting time bins of 100 ms or 30 ms, respectively, that were triggered synchronously with the EM-CCD camera integration time bins.

Sample chamber preparation included several cleaning and surface passivation procedures according to a published protocol that finally introduces a polyethylene glycol (PEG) layer onto fused silica quartz glass slides (Bennink et al., 2001; Treutlein, 2012). The sample chamber was mounted as elaborated elsewhere (Dörfler et al., 2017). For sample loading, the outlet of the sample chamber was connected to a syringe pump (PHD2000, Harvard Apparatus, Holliston, US-MA) and its inlet was connected to a buffer reservoir. The dead-volume between the buffer reservoir and the sample chamber is on the order of 5 μl and the volume of the sample chamber is on the order of 15 μl. Nucleosomes were tethered to the surface of the sample chamber via a biotin-neutravidin linkage (Bennink et al., 2001; Dörfler et al., 2017; Treutlein, 2012); the nucleosome entry DNA contained a terminal biotin (Table 2). The procedures for (i) INO80 remodeling, followed by quenching, (ii) INO80 remodeling, chase conditions and (iii) real-time INO80 remodeling are summarized in Table 8.

Table 8. Sequential buffer exchange procedures applied for the investigation of INO80 nucleosome remodeling by TIRF microscopy.

Nucleosome concentrations are given in DNA equivalents and refer to the assembly product described in section 4.3.2. This corresponds to a total nucleosome concentration on the order of 50 pM, including 5 pM/ 10 % labeled nucleosomes. Times of data acquisition are indicated and generally took 0.5-2 h. For the real-time INO80 remodeling condition, Trolox was used as a system of reducing agent and oxidant as described in Cordes et al. (2009) and was accordingly illuminated with UV light before measurements.

	INO80 remodeling, followed by quenching.	INO80 remodeling, chase conditions.	real-time INO80 remodeling.
1x RB+ buffer supplement to 1x remodeling buffer (1x RB, 25 mM Tris pH 7.6, 4 mM MgCl$_2$, 200 ng/µl BSA, 80 mM KCl, 10 % glycerol)	500 µM DTT	500 µM DTT	2 mM Trolox glucose oxidase (10 units/ml), catalase (200 units/ml; both Sigma-Aldrich, now Merck), 2 % w/v glucose 25 mM Tris pH 8 (50 mM Tris in total)
washing	100 µl 1x RB+	100 µl 1x RB+	
loading and incubation conditions *incubation time*	100 µl nucleosomes (ca. 0.03 ng/µl) in 1x RB+ *ca. 10 min* **data acquisition**	100 µl nucleosomes (ca. 0.03 ng/µl), INO80 (39 nM), ADP (2 mM, Calbiochem, now Merck) in1x RB+ *at least 10 min on ice/ 10 min after loading* **data acquisition**	100 µl nucleosomes (ca. 0.03 ng/µl) in 1x RB *ca. 10 min*
	100 µl INO80 (39 nM), ATP (2 mM, Sigma-Aldrich, now Merck) in 1x RB+ *10 min on ice/ 25 min after loading*		
	100 µl apyrase (5 units/ml, NEB) in 20 mM Tris or HEPES pH 7, 50 mM NaCl, 10 mM CaCl$_2$, 1 mM DTT, 100 ng/µl BSA, 3 % glycerol, 2 mM MgCl$_2$ *15 min*	200 µl 2 mM ATP in 1x RB+ *25 min*	100 µl INO80 (50 nM), nucleotides as indicated, in 1x RB+ **data acquisition**
thermal relaxation of nucleosomes *incubation time*	200 µl 1x RB+ *10 min* **data acquisition**	200 µl 1x RB+ *10 min* **data acquisition**	
camera integration time	105 ms	105 ms	33 ms

If indicated, the INO80 remodeling reaction was stopped by apyrase treatment (enzymatic removal of ATP) instead of a more rigorous quenching with λ-DNA preceding confocal spectroscopy assessment (section 4.6.2). λ-DNA was disadvantageous in TIRF microscopy as it introduced background signal.

The remodeled nucleosome sample (section 5.2.8) was prepared similar to the procedure described in section 4.6.2 (here: 200 nM INO80, 2.1 mM ATP, 30 °, 55 min). Quenching of the reaction was achieved by ca. 10 x dilution in apyrase quenching conditions (buffer as in Table 8). This sample was stored at 4 °. Before loading to the measurement chamber, the sample was diluted ca. 100 x in 1x RB. Data were then acquired in the conditions for live remodeling (as in Table 8) in the absence of INO80.

4.6.2 Confocal spectroscopy

A mixture of double-labeled 220 bp 601-seq nucleosomes, unlabeled 200 bp 601-seq nucleosomes and the pUC18::12x200bp-601 vector backbone, as derived from the nucleosome assembly (sections 4.1.3 and 4.3.2), was diluted to a final concentration of 20 ng/µl DNA equivalents and was remodeled with 100 nM INO80 and 2 mM ATP in 1x RB supplemented 500 µM DTT for 60 min at 27 °. The reaction was stopped by addition of λ-DNA (NEB) with a final concentration of 115 ng/µl. The reaction mixture was applied to native PAGE (3-12 % PAA, Table 6) as described in section 4.2.3 and assessed by confocal spectroscopy. Gels have been imaged for the respective fluorescent dyes attached to the nucleosomal DNA (Table 2) as described in section 4.1.4 and analyzed as described in section 4.5.

Nucleosomes and remodeled nucleosomes were diluted to a final concentration equivalent to approximately 0.5 ng/µl DNA equivalents in 1x RB supplemented with 500 µM DTT (section 4.6.1, Table 8) with reference to the DNA concentration determined for the respective nucleosome assembly (section 4.3.2). This corresponds to a total concentration on the order of 1 nM nucleosomes, including 0.1 nM/ 10 % labeled nucleosomes. All measurements were performed at RT. Nucleosomes in the presence of INO80 and 2 mM ADP were diluted to this concentration and 39 nM or 156 nM INO80, as indicated, were added last. The final buffer concentration after addition of INO80 corresponded to the composition of 1x RB supplemented with 500 µM DTT (taking the KCl and glycerol introduced by the INO80 sample into account). The sample was incubated on ice for at least 20 min to allow binding.

Time-correlated single-photon counting and pulsed interleaved excitation combined with multiparameter fluorescence detection (PIE-MFD) (Kudryavtsev et al., 2012) was performed on a confocal spectroscopy setup that has been home-built at the Institute of Biophysics, Ulm University, and is described in detail elsewhere (Schwarz et al., 2018). The lasers used for excitation (green, 531 nm and red, 640 nm, both diode lasers) have been adjusted to 95 µW and 30 µW, respectively, measured after the fiber. Of note, the emission pathway of the confocal spectroscopy setup is polarization sensitive, which is crucial for anisotropy determination.

Freely diffusing fluorescent nucleosomes were assayed similar to previous studies (Bönisch et al., 2012; Di Cerbo et al., 2014). In the present study, ca. 30 µl sample were spread into a well formed by uncolored liquid barrier marker (Carl Roth) onto surface-passivated coverslips. Passivation of coverslips essentially followed the procedure mentioned in section 4.6.1 (Bennink et al., 2001; Treutlein, 2012), omitting the biotinylation of the PEG layer as immobilization was not intended.

4.7 Förster radius determination and distance calculations

The isotropic Förster radius (R_0) was determined with the software PhotochemCAD (Dixon et al., 2005) for nucleosome samples (Figure 12). The program calculates the Förster radius, taking the emission spectrum of the donor (Tamra6), the absorption spectrum of the acceptor (Alexa647), the orientation factor κ^2 (κ^2: 2/3 for rotational averaging of the relative donor/acceptor fluorophore orientations), the quantum yield of the donor and the refractive index of the medium (here 1.38) into account (Dixon et al., 2005). The exact formula for Förster radius determination and the assumptions that justify to set $\kappa^2 = 2/3$ can be found in Hellenkamp et al. (arXiv:1710.03807 [q-bio.QM]). The emission spectrum of the donor was determined from a donor-only nucleosome sample (native PAGE shown in the appendix 12.2). The absorption spectrum of the acceptor was determined from the free dye (Alexa647).

In order to obtain the quantum yield of the donor (Φ_D), the product of the universal rate of radiative deexcitation of Tamra6 (0.2 ns^{-1}, see below) and of the amplitude-weighted mean of the donor lifetimes of the LF nucleosome construct (3 ns, see below) was used, according to Hellenkamp et al. (arXiv:1710.03807 [q-bio.QM]). Φ_D therefore was 0.6. For determination of the donor lifetime, I combined data of various confocal spectroscopy measurements of constructs derived from the Fp13Rm84-DNA, selected the donor-only nucleosomes that occurred simultaneously with the double labeled nucleosomes and fitted

the fluorescence lifetime of the pseudo-bulk lifetime decay of this species (fluorescent donor nucleosomes) with a double-exponential decay (section 4.8.3). This procedure yielded the same unquenched donor lifetime for nucleosome datasets derived from either the Fp13Fm65-DNA or from the Fp13Fm72-DNA. The universal rate of radiative deexcitation of Tamra6 was determined by Dr. Carlheinz Röcker and Eleni Kallis, both Institute of Biophysics, Ulm University, from lifetime and quantum yield measurements on Tamra6.

Using the aforementioned parameters and spectra, PhotochemCAD (Dixon et al., 2005) determined the isotropic Förster radius of all nucleosome constructs to be 67 Å. The distance uncertainty of the Förster radius was assumed to be 7 % as evaluated in a recent study by Hellenkamp et al. (arXiv:1710.03807 [q-bio.QM]).

The FRET efficiency, as determined by TIRF microscopy (section 4.8.2), was converted to the apparent distance of donor and acceptor (r) using Equation 2 (FRET-averaged distance, according to Hellenkamp et al. (arXiv:1710.03807 [q-bio.QM]). Equation 2 is an alternative representation of the classical distance-FRET efficiency relationship based on the theory derived by Förster and advanced by Stryer (Förster, 1948; Stryer and Haugland, 1967). E_μ is the mean of the FRET efficiency distribution as obtained from Gaussian fitting.

$$ r = R_0 \cdot \sqrt[6]{E_\mu^{-1} - 1} $$

Equation 2

The distance uncertainty of the apparent distance of donor and acceptor was derived as proposed in Hellenkamp et al. (arXiv:1710.03807 [q-bio.QM]), taking the distance uncertainty of the Förster radius and the standard deviation of the FRET efficiency into account. The denoted distance uncertainties for TIRF microscopy derived quantitative distance information refer to this uncertainty.

Note that confocal spectroscopy data were treated differently in order to determine the apparent distance of donor and acceptor and the corresponding uncertainty (section 4.8.3). Confocal spectroscopy FRET efficiency histograms were fitted either with the sum of three Gaussian distributions (MATLAB Curve Fitting Toolbox, sections 5.2.3,

5.2.4 and 5.2.5) or were converted to time binned (1 ms) histograms and fitted by probability distribution analysis (PDA; software description in section 4.8.3, data representation in appendix 12.3). Both approaches for fitting were applied by Eleni Kallis, Institute of Biophysics, Ulm University. PDA simulates an uncorrected FRET efficiency histogram for a Gaussian donor-acceptor dye distance distribution, taking into account the stochastic fluctuations of photon emission, the background and the correction factors (Antonik et al., 2006). PDA then iteratively optimizes the parameters that describe these donor-acceptor dye distance distributions to best describe the experimentally derived FRET efficiency histogram (Antonik et al., 2006). All quantitative distance information with respect to the apparent inter-dye distance was retrieved by PDA from confocal spectroscopy derived datasets as described in Schwarz et al. (2018). A detailed description of the uncertainty estimation of the derived distances (by Eleni Kallis) can be found in Schwarz et al. (2018).

The apparent distance of donor and acceptor retrieved from either TIRF microscopy or confocal spectroscopy data was converted to the distance of mean dye positions with a polynomial provided by Tobias Eilert, Institute of Biophysics, Ulm University. This particular polynomial for distance interconversion is valid for the given Förster radius (67 Å) and assumes spherical accessible volumes for the dyes with a radius of 20 Å, as published previously (Eilert et al., 2017). Equation 3 was applied for distance interconversion to determine the distance of mean dye positions (Eilert et al., 2017).

$$distance\ of\ mean\ dye\ positions =$$

$$= -34{,}3\ \text{Å} + 1{,}64 \cdot r - 1{,}59 \cdot 10^{-3} \frac{1}{\text{Å}} \cdot r^2 + 1{,}00 \cdot 10^{-5} \frac{1}{\text{Å}^2} \cdot r^3$$

Equation 3

4.8 Software applications for FRET

4.8.1 Calculation of the expected distance of mean dye positions

The expected mean dye positions were calculated with the FRET-restrained positioning and screening (FPS) software (Kalinin et al., 2012). The structure of the NCP wrapped by the 601-seq (PDB 3LZ0) (Vasudevan et al., 2010) served as a template. As a first

approximation for the entry- and exit DNA of the nucleosome, B-form DNA was built in USCF Chimera (Pettersen et al., 2004) and aligned with the second base pair (position ± 71) of the NCP close to the DNA entry/exit site, respectively. Of note, this does not necessarily reflect the entry/exit DNA coordination present in solution. A dye linker length of 19 Å (Alexa647) and 15 Å (Tamra6) was used for the FPS simulation (Kalinin et al., 2012), as well as a linker width of 4.5 Å and a dye radius of 6 Å. This was based on the numbers originally proposed (Kalinin et al., 2012) and on an estimation based on the structures of the dyes when covalently linked to a nucleobase via a flexible C6 linker (section 4.1.2). The accessible volumes displayed in the appendix 12.3 were calculated with the <u>N</u>ano-<u>P</u>ositioning <u>S</u>ystem (NPS) (Dörfler et al., 2017; Eilert et al., 2017; Muschielok and Michaelis, 2011) and represent expected priors without additional information from experimental data. The following parameters for the acceptor and donor were used: dye diameter 12 Å, linker length 18 Å, linker diameter 4.5 Å for the acceptor and dye diameter 13 Å, linker length 12 Å and linker diameter 4.5 Å for the donor. Both softwares (FPS, NPS) use different definitions for dye geometries. This explains minor differences in input parameters. The nucleosome structures and accessible volumes from NPS were displayed with USCF Chimera. The distance between the simulated donor and acceptor mean dye positions calculated with FPS was measured with USCF Chimera. In order to calculate expected FRET efficiencies (Table 9) this measured distance was converted to the apparent inter-dye distance (Eilert et al., 2017), which relates to the classical distance-FRET efficiency relationship (section 4.7, according to Förster (1948), Stryer and Haugland (1967) and Hellenkamp et al. (arXiv:1710.03807 [q-bio.QM])).

4.8.2 Analysis of TIRF microscopy data

Single molecule FRET time trajectories were extracted from the movies recorded with EM-CCD cameras (section 4.6.1) using software provided by the laboratory of Prof. Don Lamb, LMU Munich that has been described in detail (Heiss, 2011). In order to display the field of view of the green and red camera with reference to the same spatial coordinates, a bead map was generated similar to a published procedure (Dörfler et al., 2017) and applied as described (Heiss, 2011). All fluorescence intensities were background-corrected (Heiss, 2011). In order to calculate the FRET efficiency, different correction factors need to be taken into account as elaborated in Hellenkamp et al. (arXiv:1710.03807 [q-bio.QM]), that is (i) the γ-factor, which corrects for differences of donor and acceptor dye with respect to their quantum yields and with respect to the instrument specific detection efficiencies, (ii) a correction factor for the spectral crosstalk of the green emitted light leaking into the acceptor detection channel, denoted α, and

(iii) a correction factor accounting for residual direct excitation of the acceptor dye with the green laser, denoted δ. FRET efficiencies are calculated according to Equation 4; details can be found elsewhere (Hellenkamp et al., arXiv:1710.03807 [q-bio.QM]). *I* denotes background corrected intensity, *A* denotes acceptor, *D* denotes donor, *em* denotes emission and *ex* denotes excitation.

$$E = \frac{I_{Aem,Dex} - \alpha I_{Dem,Dex} - \delta I_{Aem,Aex}}{\gamma I_{Dem,Dex} + I_{Aem,Dex} - \alpha I_{Dem,Dex} - \delta I_{Aem,Aex}}$$

Equation 4

Of note, for TIRF microscopy data, δ = 0 was assumed. This is a simplification that eventually does not affect the calculated FRET efficiency in most cases; it can however lead to an overestimation of the FRET efficiency in a regime of very low FRET efficiencies (Hildebrandt et al., 2015).

The γ-factor and α were determined for each molecule individually according to Dörfler et al. (2017). A subset of molecules did not qualify for this approach as outlined in section 5.2.7 and were corrected with a global γ-factor and α (Hellenkamp et al., arXiv:1710.03807 [q-bio.QM]). This global γ-factor (and global α) corresponded to the mean of the respective distribution of the individual γ-factors (and α) addressed above. The global γ-factor was determined per class of nucleosomes based on the same DNA-construct and was 0.55 for the Fp13Rm84 class, 0.50 for the Fp13Fp65 class and 0.50 for the Fp13Fp72 class; α was 0.045 (for all measurements with 105 ms camera integration time). When instead a camera integration time of 33 ms was used, the γ-factor was 0.70 and α was 0.054 (Fp13Rm84 derived constructs). Most scripts necessary to combine the local and global γ-factor correction (for details, see section 5.2.7) have been available, as implemented in the abovementioned software (Heiss, 2011).

The time-averaged FRET efficiency of each individual molecule was used to construct FRET efficiency histograms that were displayed in MATLAB (MathWorks, US-MA) and fitted with the MATLAB Curve Fitting Toolbox.

Local Hidden-Markov-Models (HMM) applied to individual FRET efficiency time trajectories in section 5.2.8 are based on an HMM toolbox (https://github.com/probml/pmtk3) that has been applied successfully to smFRET data

previously (Sikor et al., 2013) and that is available, albeit adapted, in the abovementioned software (Heiss, 2011).

4.8.3 Analysis of confocal spectroscopy data

Individual fluorescent bursts originating from freely diffusing fluorescent molecules during passage of a femto-liter-sized focal volume were recorded with a confocal setup (section 4.6.2). A burst was qualified as such if at least 10 photons in 500 μs and 50 or more photons per burst in total were detected (irrespective of the detection channel), known as all-photon-burst-search (APBS) (Nir et al., 2006). The software that has been used in the present study for analyzing confocal spectroscopy data, denoted as pulsed interleaved excitation analysis with MATLAB (PAM, https://www.gitlab.com/PAM-PIE/PAM) has been recently published by the group of Prof. Don Lamb, LMU Munich (Schrimpf et al., 2018). This software was used for the APBS, for fitting the fluorescence lifetime from pseudo-bulk lifetime decays (section 4.7), for the determination of FRET efficiency histograms or the fluorescence anisotropy and lifetime histograms, and for PDA fitting (section 4.7).

All data were corrected for background, crosstalk (α) and direct excitation (δ) according to Equation 4 based on previously published procedures (Kudryavtsev et al., 2012; Lee et al., 2005). Final histograms contain only fluorescence bursts with at least 100 photons and were cleared from rare multimolecule events using the alternating laser excitation-two-channel kernel-based density distribution estimator filter (ALEX-2CDE filter) set to an upper limit of 8 or 9 (Tomov et al., 2012). For γ-factor determination, a combined dataset of each individual labeling class, that is, of the Fp13Rm84 derived constructs, of the Fp13Fp65 derived constructs and of the Fp13Fp72 derived constructs, was generated. A global γ-factor per class was determined using the so-called stoichiometry method (Kudryavtsev et al., 2012; Lee et al., 2005); γ-factors are 0.55, 0.64 and 0.56, respectively. Overall, this method yielded a consistent comparison of all data that relate to the same labeled DNA. Another method, namely the γ-factor determination via a characteristic fit that relates FRET efficiency to donor lifetime (Kudryavtsev et al., 2012) was inappropriate, as dye properties could not be described with a global set of parameters that yielded reasonable fits for all data related to the Fp13Rm84 DNA.

52

5. Results

5.1 INO80 purification, nucleosome assembly and INO80-nucleosome interplay

5.1.1 Endogenous *Sc*INO80 complex purification and storage

The 19-subunit *Sc*INO80 complex was purified endogenously from yeast cells (section 4.2.2) according to an established protocol (Tosi, 2013; Tosi et al., 2013). The protein yield was improved by lysing cells with a cryogenic grinder (section 4.2.2), compared to bead-beater cell lysis. Protein purification following cryogenic grinding yielded > 1 µg pure INO80 complex per gram yeast cells. Furthermore, after affinity chromatography and anion exchange chromatography, a pure and concentrated sample of the INO80 complex was obtained (Figure 4 a, b). This sample was suited to find appropriate long-term storage conditions, as the concentration was maximal at this purification step (Tosi, 2013) and low concentrations generally favor protein complex disintegration.

I found final buffer concentrations of 20 mM HEPES pH 8, 350 mM KCl, 25 % glycerol, 0.8 mM DTT, 3.2 mM $MgCl_2$ to be optimal for flash freezing and storage at -80° C (Figure 4 b, c) (section 4.2.2). The components of the INO80 complex are intact after having been subjected to the described storage conditions (Figure 4 b, lane labeled -80° C). The INO80 complex can slide mononucleosomes robustly after storage; with increased product formation the more INO80 is present (Figure 4 c). Increasing the concentration of the INO80 complex also leads to a pronounced shift of a fraction of the nucleosomes to the well of the gel matrix due to binding by INO80. Note also the complete binding of the 147 bp crDNA by INO80 in the control lane without ATP (Figure 4 c, in line with section 5.1.4).

A qualitative assessment of the integrity of the INO80 complex was done by native PAGE (Figure 4 d). Here, the functional INO80 complex showed a prominent characteristic and broad band for a high molecular weight species, indicative for a (probably fully) assembled complex after freezing. In other words, this assessment does not show partially disassembled INO80 complexes. It is however no direct evidence for complex integrity as it lacks suitable control samples, such as INO80 sub-module deletion complexes that have been described in Tosi et al. (2013). Taken together, the INO80

complex can be purified endogenously from yeast, essentially according to Tosi et al. (2013) and long term storage at -80° C has been established.
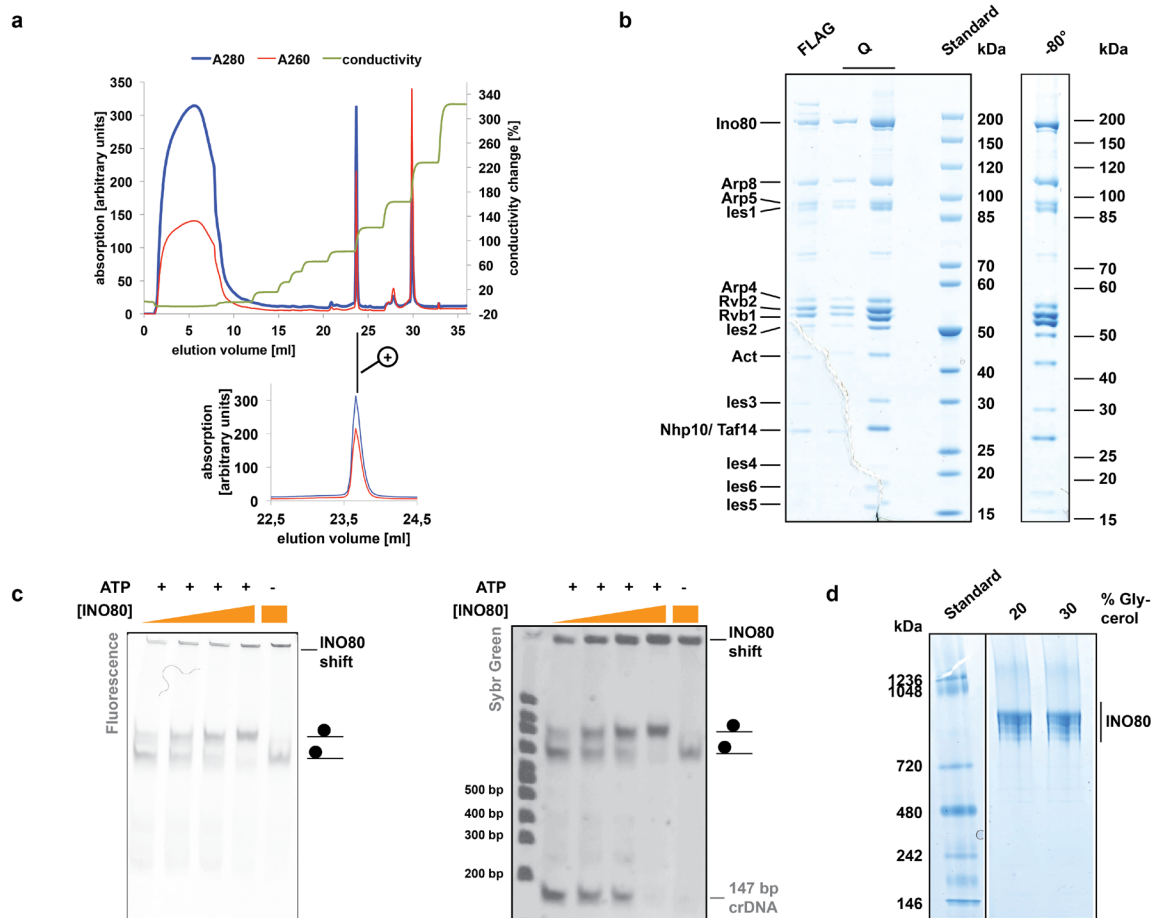

Figure 4. Purification and storage of the endogenous *Sc*INO80 complex.
(a) Anion exchange chromatography elution profile (INO80 purification). (b) SDS-PAGE (4-12 %) of INO80 purification with affinity chromatography (FLAG), anion exchange chromatography (Q) and storage (-80 °/ 25 % glycerol; uncropped gel in appendix 12.2). (c) Native PAGE (6 %) of mononucleosome sliding (7N66) with 11 nM, 18 nM, 23 nM, 37 nM, 37 nM INO80 (after INO80 storage, -80°/ 20 % glycerol), left panel: fluorescence scan for labeled nucleosomes (Typhoon), right panel: image of the same gel after SybrGreen staining (INTAS); note the presence of the 147 bp competitor DNA (section 4.3.2). (d) Native PAGE (3-12%) of the entire INO80 complex; two separate regions of the same gel are represented (complete gel in appendix 12.2).

5.1.2 Histone purification and octamer assembly

Human histone proteins were recombinantly expressed in *E. coli* and purified as described in Haas (2013) and in Klinker et al. (2014) (sections 4.1.2 and 4.2.2). Induction of the expression of a plasmid encoded histone gene (section 4.2.2) provoked massive synthesis of the respective gene product for each individual histone (Figure 5 a). As exemplarily shown for histone H2A, in a first step after cell lysis, the histone was purified with cation exchange chromatography under denaturing conditions (section 4.2.2)

54

(Figure 5 b, c). Pure fractions were pooled (Figure 5 c), refolded, applied to a reverse anion exchange chromatography and H2A was then pure (section 4.2.2, Figure 5 d).
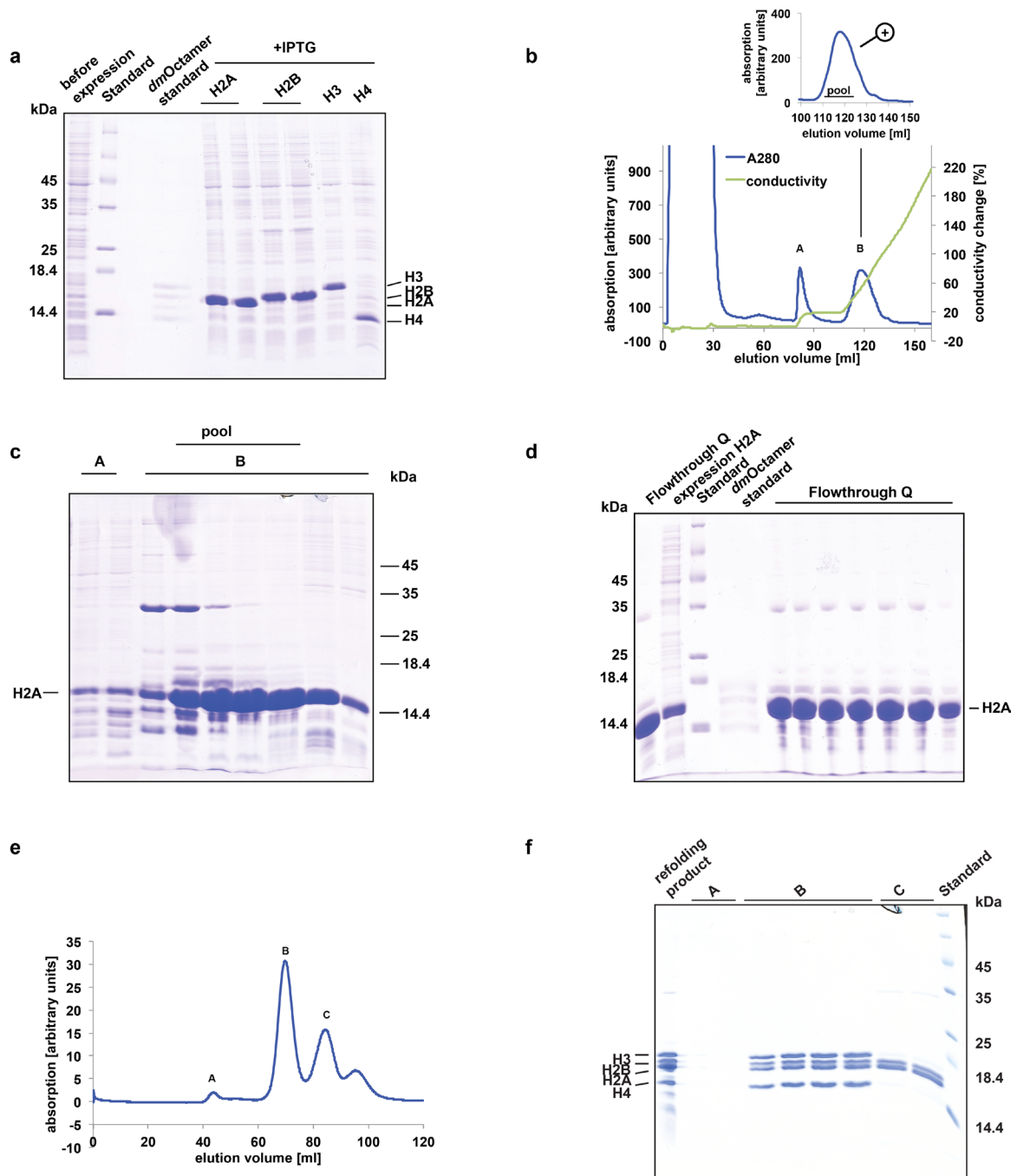

Figure 5. Histone purification and octamer assembly.
(a) SDS-PAGE (18 %) of individual recombinant expression of *Hs*H2A, *Hs*H2B, *Hs*H3 and *Hs*H4 in *E. coli*. (b) Cation exchange chromatography elution profile of H2A purification. (c) SDS-PAGE (18 %) of H2A purification (fractions collected by cation exchange chromatography). (d) SDS-PAGE (18 %) of H2A purification (reverse anion exchange chromatography). (e) Size exclusion chromatography elution profile after octamer refolding. (f) SDS-PAGE (18 %) of octamer formation (fractions collected by size exclusion chromatography). Uncropped gel of (c) in appendix 12.2.

Histone octamers were formed by refolding after mixing individually purified histones in denaturing conditions as described in Klinker et al. (2014) and in Dyer et al. (2003). The refolding product was separated by size, using size exclusion chromatography (Figure 5 e). This constitutes also an important additional purification step that removes residual side-products from individual histone purifications (see also note in section 4.2.2). Complete octamer formation (in contrast to e.g. concomitant hexamer and octamer formation) was ensured by using excess of H2A and H2B, which elute in a separate dimer peak if all H3/4 tetramers have been saturated with two H2A/B dimers to form an intact histone octamer (Haas, 2013; Klinker et al., 2014) (Figure 5 e). Stoichiometric histone octamer formation was verified by SDS-PAGE (Figure 5 f).

5.1.3 Mononucleosome formation

Mononucleosomes can be assembled from DNA and histone octamers using salt gradient dialysis (Dyer et al., 2003) (section 4.3.2). For alike-assembled chromatin fibers, the introduction of a competitor DNA (crDNA, 147 bp) of about the same length as the DNA wrapping the octamer core has been exploited to assess the saturation of the assembly (Huynh et al., 2005). Here, the octamer deposition is energetically favored for the 601-seq (Lowary and Widom, 1998), while the crDNA forms an NCP only upon 601-seq saturation (Huynh et al., 2005). Alternatively, plasmid backbone DNA has also been used previously as competitor DNA in mononucleosome assembly protocols (Sundaramoorthy et al., 2017; Treutlein, 2012) (section 5.1.6). In order to optimize the nucleosome or chromatin fiber assembly product, the ratio of octamers to DNA is varied in the reaction mixtures subjected to salt gradient dialysis (Dyer et al., 2003; Huynh et al., 2005).

Using this rational, I could induce mononucleosome formation in the presence of a 147 bp crDNA such that the resulting nucleosome species (7N66, 601-seq nucleosome with 7 bp and 66 bp overhang, respectively) migrates as a single band on a native PAGE. This is the case for full saturation of the 601-seq with histone octamers and only marginal NCP formation (Figure 6 a, b, c, 7N66-1.7, denoting a molar ratio of octamer to 601-seq DNA of 1.7). This was of importance, as a second band was observed when a smaller amount of histone octamer was used in the assembly (Figure 6 a, b, c, 7N66-1.1). Presumably, this species with increased electrophoretic mobility compared to the nucleosomes assembled on the same 601-seq DNA constitutes hexasomes as observed recently (Frouws et al., 2018; Levendosky et al., 2016).
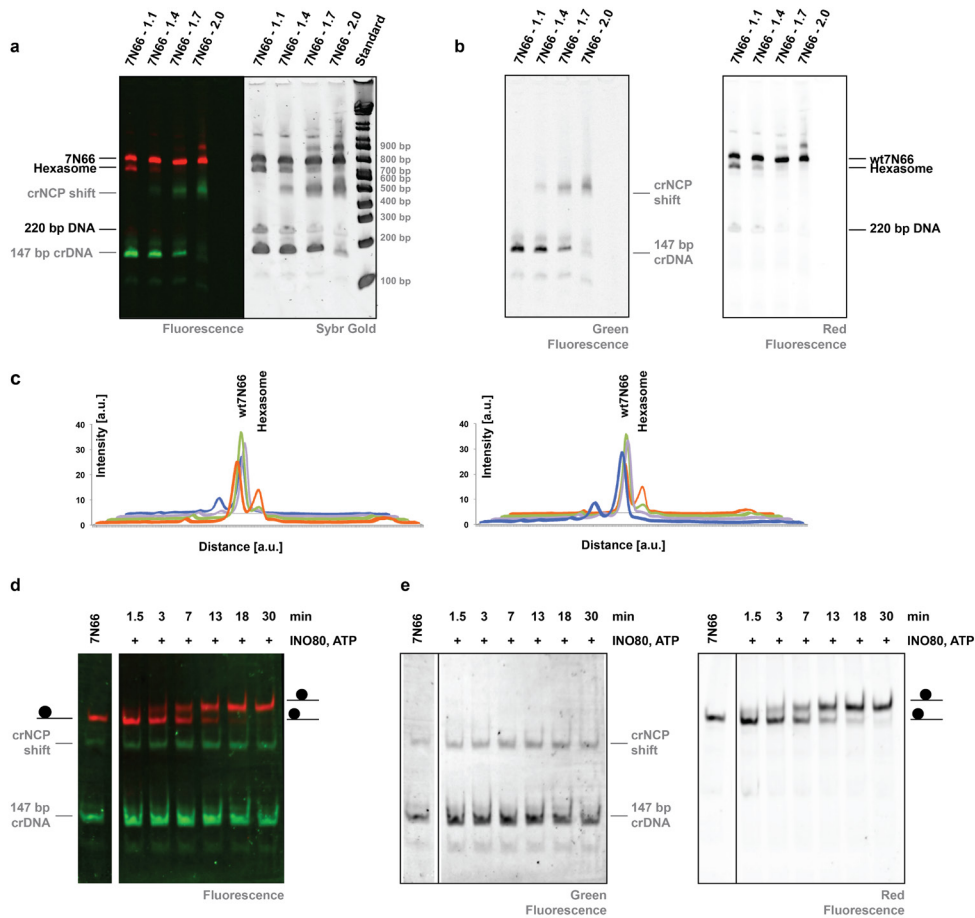
Figure 6. Mononucleosome formation and mononucleosome sliding.
(a) Native PAGE (6 %) of 7N66 nucleosome assembly in the presence of competitor DNA (147 bp crDNA); left: false color multichannel fluorescence readout for 220 bp 601-seq DNA (red bands) and for 147 bp crDNA (green bands); right: SybrGold staining of the same gel. (b) Separate single channel fluorescence readouts (green and red, respectively) of (a). (c) Intensity profiles of the red fluorescence readout shown in (b); (orange) 7N66 – 1.1, (green) 7N66 – 1.4, (violet) 7N66 – 1.7, (blue) 7N66 – 2.0, right panel: this order, left panel: reverse order. (d) Native PAGE (6 %) of 7N66 nucleosome remodeling by INO80 in the presence of competitor DNA (147 bp crDNA) in false colors as in (a). (e) Separate single channel fluorescence readouts (green and red, respectively) of (d). Fluorescence imaging: ChemiDocMP. Octamer:601-seq DNA ratios are indicated for each lane of the native PAGE. Remodeling in (d) was conducted in the presence of an INO80 specific nanobody that does not impact sliding (section 5.1.4, appendix 12.2, section 4.4.2). (d, e) represent two separate regions of the same gel (complete gel in appendix 12.2). Figure 6 a, b is adapted from Schwarz et al. (2018).

Likewise, at higher molar octamer:601-seq DNA ratios (e.g. 7N66-2.0), a side-product with reduced electrophoretic mobility was observed. Here, the 601-seq DNA has been saturated, as NCP formation on the crDNA is distinct (Figure 6 a, b, c, 7N66-2.0). A plausible explanation of the side-product is the formation of an overlapping dinucleosome (Kato et al., 2017). However, if so, the total length of the DNA is too short to accommodate all histone-DNA contacts described in (Kato et al., 2017). Maybe the contacts closest to the DNA entry and exit site present in the crystal structure (PDB 5GSE) (Kato et al., 2017) with the H3αN helix do not form if the observed nucleosome

assembly side-product in the present study is an overlapping dinucleosome. Alternatively, maybe a different position of the octamer on the DNA is enabled when over-titrating with histone octamers. Taken together, including crDNA to titrations of octamers for assembling 601-seq mononucleosomes is a convenient tool to gain a homogenous nucleosome sample upon 601-seq saturation.

Here, crDNA and 7N66 mononucleosomes can be distinguished spectroscopically by using different fluorophores for visualization (Figure 6 a, b). This is especially useful when monitoring the INO80 complex and its sliding activity on end-positioned mononucleosomes (Figure 6 d, e). As expected, robust nucleosome sliding takes place while the crDNA and the residual negligible NCP are not processed by the INO80 complex. Thus, the homogenously assembled 7N66 nucleosome samples can be used directly for assessing INO80 activity in the presence of crDNA, without the need of further purification steps. Still, this is a specialized condition and requires great care when inferring INO80 mechanistic features (see section 5.1.4).

5.1.4 Characterization of the recombinant ScINO80 complex

I validated the functionality of the purified recombinant *Sc*INO80 complex. These were key experiments to approve the recombinant INO80 expression for a comprehensive characterization of the recombinant *Sc*INO80 with various approaches, for example by smFRET (section 5.2). Dr. Sebastian Eustermann and Manuela Moldt, both Gene Center and Department of Biochemistry, LMU Munich, established its expression, generated the point mutants presented in Figure 7 and provided purified INO80 samples.

The recombinant wild-type *Sc*INO80 robustly repositions mononucleosomes to a more centered position (Figure 7 a). Increasing INO80 concentration also increases the formation of the repositioned nucleosome, in line with the described activity of the endogenously purified INO80 complex (section 5.1.1).

The INO80 complex harbors ten more subunits with a conserved ATP binding site (Shen et al., 2000; Tosi et al., 2013; Watanabe et al., 2015) (actin, Arps, Rvbs), in addition to the main ATPase. It was therefore of interest to see if the INO80 complex with Walker B mutants of Rvb1 and Rvb2 is still functional. This mutant INO80 complex is also fully functional in mononucleosome repositioning (Figure 7 b) and differences (wild-type vs. mutant INO80) in this and other sliding assays (data not shown) are only small. Note that this assay is not suitable to report on minor variations of the degree of nucleosome sliding. When additionally the Ino80 main ATPase was mutated, sliding activity was

abolished (Figure 7 b). This suggests a fundamental role of INO80's main ATPase for nucleosome sliding, while the ATPase activity of other subunits of the complex might play only a minor role (if at all) for nucleosome repositioning. Indeed, this was expected, as an early study demonstrated that the Ino80 main ATPase Walker A mutant abolishes ATPase activity of the *Sc*INO80 complex almost completely, even though other subunits have intact ATP binding sites (actin, Arps and Rvbs) and are an integral part of the INO80 complex (Shen et al., 2000). Further, INO80 ATPase activity and nucleosome sliding are completely abolished for an Ino80 main ATPase Walker B mutant in the context of *Hs*INO80^{conserved} (Willhoft et al., 2017).
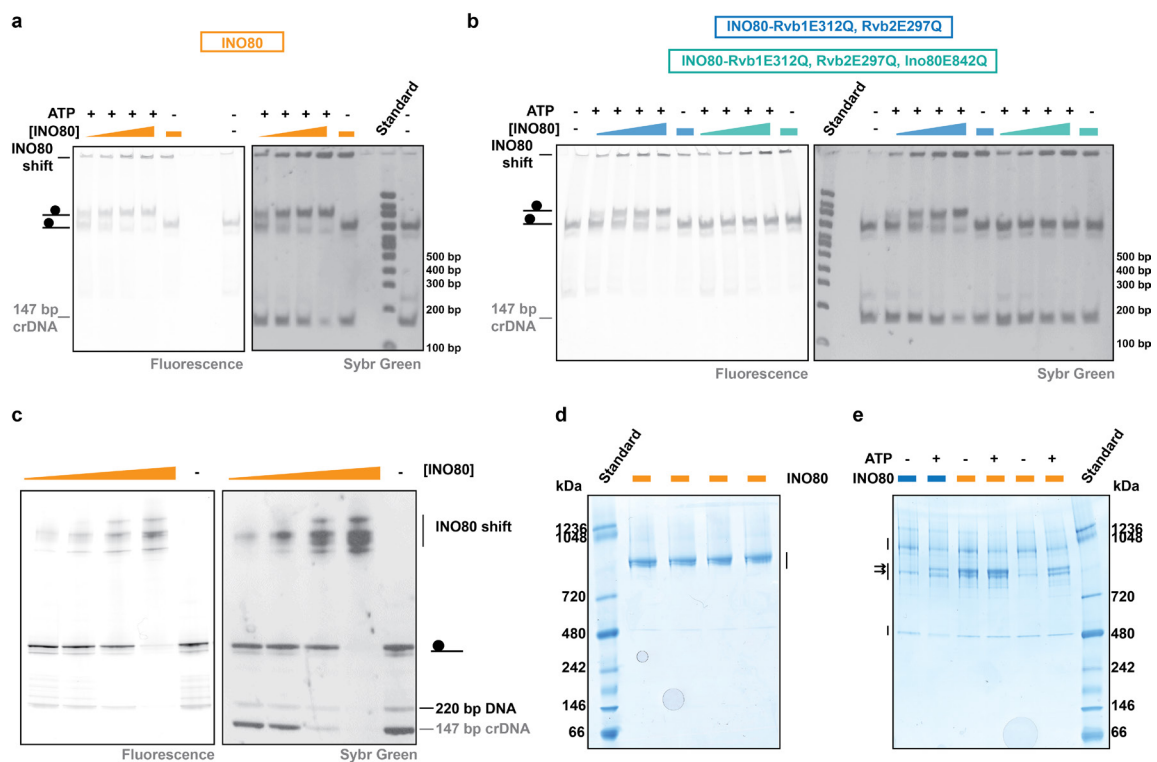
Figure 7. Characterization of the recombinant INO80 complex.
(a) Native PAGE (6 %) of mononucleosome sliding by the wild-type recombinant INO80 complex (11 nM, 20 nM, 27 nM, 41 nM, 27 nM INO80). (b) Native PAGE (6 %) of mononucleosome sliding by Walker B mutants of the recombinant INO80 complex, concentrations as in (a). (c) Competitive INO80 binding assay with approximately equimolar 147 bp crDNA and 7N66 nucleosomes (native PAGE, 3-12 %). INO80 concentrations are 25 nM, 50 nM, 100 nM, 200 nM, 0 nM. (a, b, c) Left panel: fluorescence scan for labeled nucleosomes (Typhoon), right panel: image of the same gel after SybrGreen staining (INTAS); note the presence of the 147 bp competitor DNA (section 4.3.2). (d) Native PAGE (3-12 %) of the INO80 complex after incubation of INO80 with different KCl concentrations (100 mM, 200 mM, 300 mM, 400 mM). (d) Native PAGE (3-12 %) of the INO80 complex with/ without prior incubation with ATP. Lane 3 and 5 as well as lane 4 and 6 have been prepared in the same way (independent replicates).

As the nucleosome sliding assays presented here are performed in the presence of crDNA (Figure 6, Figure 7) it was of interest to determine which binding partner (crDNA or 7N66 mononucleosomes) is preferred by the INO80 complex. Figure 7 c exemplifies that

the first substrate to be fully bound by the INO80 complex is the crDNA when approximately equimolar concentrations of both substrates (nucleosomes and crDNA) are present in concentrations well above the dissociation constant K_d; the K_d is in the low nanomolar range, sections 4.4.1 and 5.1.5. In this respect, the INO80 complex is unique compared to other remodelers that prefer nucleosome binding compared to DNA binding (Clapier et al., 2017). INO80 might integrate DNA- and nucleosome binding properties. This correlates with known functions of the INO80 complex, as it binds to the +1 nucleosome and the NFR *in vivo*, and it is required to establish yeast promoter regions *in vitro* (Krietenstein et al., 2016; Yen et al., 2013). Further, INO80 requires >60 bp flanking DNA for productive nucleosome sliding *in vitro* (Udugama et al., 2011; Zhou et al., 2018).

As established for the endogenous INO80 complex, a qualitative assessment on the integrity of the INO80 complex was performed by native PAGE (Figure 7 d, e). Again, a prominent characteristic band for a high molecular weight species was observed (comparable to the endogenous INO80 complex, Figure 4 d). However, the INO80 complex also often showed a tripartite electrophoretic mobility (Figure 7 e). Conformation, size and charge all contribute to the electrophoretic mobility assayed by native PAGE (Arndt et al., 2012), and it is therefore difficult to draw clear conclusions from the electrophoretic mobility of large, natively folded protein complexes (that may feature conformational heterogeneity). Multiple bands observed by native PAGE may reflect conformational heterogeneity as well as complex disintegration. Therefore, differences exemplified by Figure 7 d vs. Figure 7 e between equivalently prepared INO80 complexes cannot be fully explained. In order to reconcile both observations (Figure 7 d vs. Figure 7 e), I incubated the INO80 complex with ATP prior to the native PAGE. This induced the formation of a characteristic double band of a high molecular weight species (Figure 7 e) that is similar to Figure 7 d. If ATP binding by one or more subunits of the INO80 complex is the reason for the observed double-band formation, conformational changes as well as reduction of the net charge due to the introduction of one ore more nucleotides, can influence electrophoretic mobility. Therefore, this phenomenon can be described only qualitatively. It is however of great interest to see in future studies if the nucleotide state of one or more INO80 subunits has an impact on the overall complex conformation and thus may have functional importance.

Further, the impact of a nanobody that has been raised against INO80 (Tosi, 2013) was tested in the context of INO80 mediated mononucleosome sliding (Figure 8). When analyzing technical triplicates of INO80 nucleosome sliding probed at different points in

60

time (Figure 8 d) no significant difference in sliding for wild-type INO80 vs. INO80 incubated with the nanobody was observed.
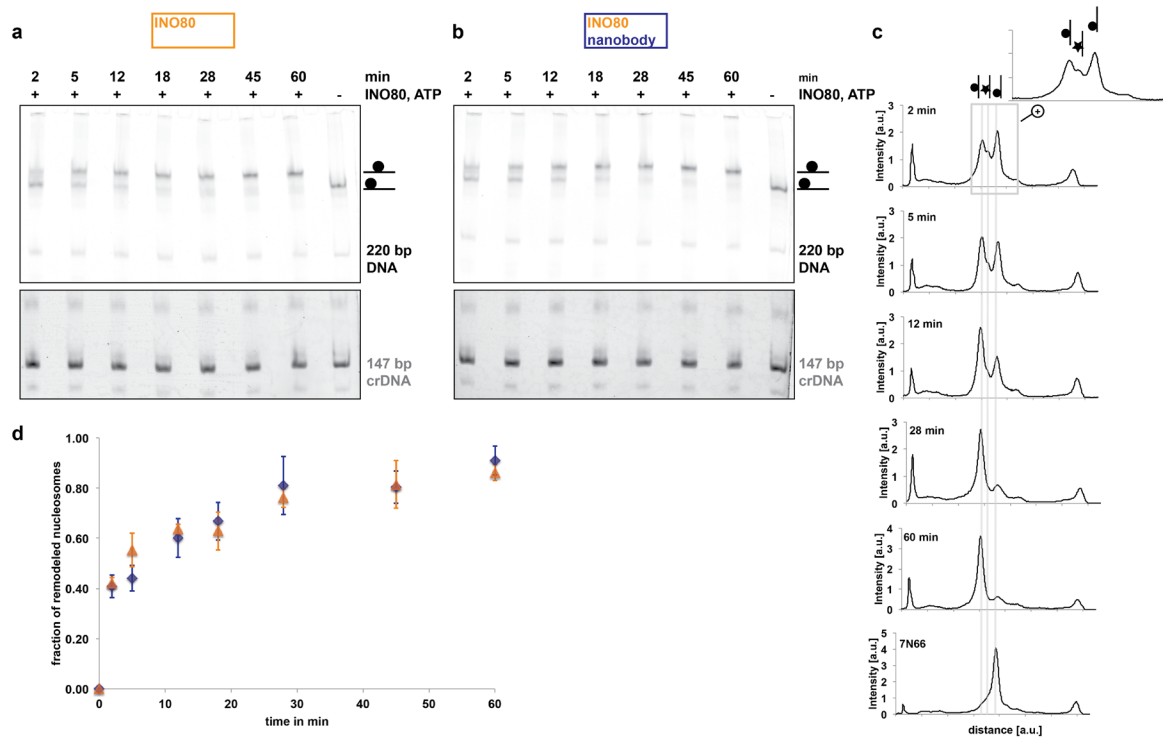

Figure 8. INO80 remodeling probed at different points in time.
(a) Native PAGE (6 %) of 7N66 nucleosome remodeling by wild-type INO80 (top panel, red fluorescence) in the presence of 147 bp crDNA (bottom panel, green fluorescence). (b) as in (a), but in the presence of an INO80 specific nanobody. (c) Intensity profiles of the red fluorescence readout shown in (b). (d) Quantification of technical triplicates for INO80 remodeling (INO80, orange, as in (a)) and INO80/nanobody, blue, as in (b)). Error bars are standard deviations of technical triplicates. For intensity profiles, the same distance from the top of the gel is shown but peaks have been aligned for better visualization.

As homogenously assembled mononucleosomes come along with roughly equimolar amounts of crDNA (section 5.1.3), the nucleosome sliding conditions (section 4.4.2) presented in Figure 8 do not reflect conditions used in classical enzymology and do not report on absolute kinetic rates. *Per se*, assays with competing binding partners or substrates can be highly relevant. For mechanistic studies on the related SWR1 complex such conditions have been intentionally developed to directly infer substrate preferences (Ranjan et al., 2013). When investigating nucleosome sliding in the presence of competing DNA, this has been shown to drastically influence apparent sliding rates (Sinha et al., 2017). This is a known caveat that can be overcome by ensuring equivalent amounts of competing DNA in all samples used to perform comparative studies (Sinha et al., 2017). Therefore, probing nucleosome sliding at different points in time for wild-type

INO80 (Figure 8 a) vs. INO80 incubated with the nanobody (Figure 8 b) is designed as a direct comparison of both conditions (section 4.4.2).

Interestingly, close inspection of the intensity profiles of the fluorescent nucleosome probes (Figure 8 c) reproducibly revealed three largely overlapping peaks after remodeling for 2 min (largely independent of the addition of the nanobody, data not shown). As the reaction was stopped by addition of competitor DNA to remove INO80 from nucleosomes, and nucleosomes then most likely relaxed to a more stable position, I propose to observe an intermediate remodeled nucleosome state after 2 min remodeling. Nucleosome conformations resulting from incomplete nucleosome sliding present in the *ensemble* are potentially heterogeneous when the remodeling reaction is quenched. However, as outlined in section 5.2.2, a defined intermediate nucleosome conformation may form upon relaxation as the rotational periodicity of the DNA wrapped around the nucleosome dictates defined energetically favored states (Blosser et al., 2009; Chua et al., 2012; Lowary and Widom, 1998; Luger et al., 1997a; McGinty and Tan, 2015). Such nucleosome intermediates and products are a characteristic feature of HsINO80^{conserved} mediated nucleosome sliding (Willhoft et al., 2017) and to some extent of the ScINO80 mediated nucleosome sliding (Zhou et al., 2018). In the latter study, the product distribution with respect to the nucleosome position on DNA was shown to depend on DNA-sequence, suggesting that the 601-seq contributes to distinct repositioned nucleosomes (Zhou et al., 2018).

5.1.5 Characterization of INO80 affinity to wild-type and all tailless nucleosomes

To characterize the INO80 bound state for wild-type and all tailless nucleosomes, its affinity to wt7N66 and to at7N66 nucleosomes was tested by EMSA, in the absence of competitor DNA (section 4.4.1). When quantified, these data reveal a tight binding of INO80 to nucleosomes (Figure 9). The dissociation constant is in the low nanomolar range. The fits presented for the data represent the exact description of the binding equilibrium (section 4.4.1), assume a 1:1 complex formation (Figure 9) and describe the data well ($R^2_{adj} = 0.999$ for wt7N66, $R^2_{adj} = 0.995$ for at7N66). Still, the absolute stoichiometry remains to be determined and I cannot rule out, for example, INO80 dimer formation as recently demonstrated for the catalytically active HsINO80^{conserved} complex (Willhoft et al., 2017). Importantly, the overall binding affinity is not changed in the absence of histone tails (Figure 9).
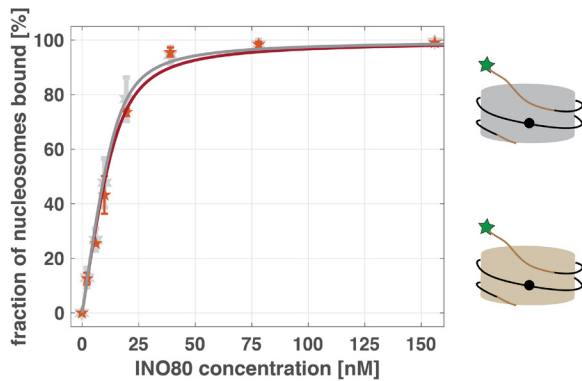
Figure 9. Binding affinity of the INO80 complex to wild-type and all tailless nucleosomes.

The fraction of bound nucleosomes (wt7N66, grey and at7N66, brown) was determined with EMSAs. Error bars are standard deviations from technical triplicates. The fit describing the binding curve and the fit parameters can be found in section 4.4.1. EMSAs have been performed by Kevin Schall, Gene Center and Department of Biochemistry, LMU Munich, see also appendix 12.3. Figure 9 is adapted from Schwarz et al. (2018).

5.1.6 Assembly of smFRET applicable mononucleosomes

In order to provide homogenous nucleosome samples for single-molecule applications, I extended the strategy presented in section 5.1.3 following an approach that uses the entire *pUC18*-plasmid backbone as competitor DNA (section 4.3.2), similar to an established protocol (Sundaramoorthy et al., 2017; Treutlein, 2012). Here, sample homogeneity is required for the labeled portion of the sample (double labeled 7N66 mononucleosomes, section 5.2.1).

The 7N66 mononucleosome forms upon octamer:601-seq DNA titration in the reaction mixtures subjected to salt gradient dialysis (Figure 10). The actual FRET probe (double labeled 7N66) can be visualized exclusively in fluorescent scans, Figure 10 a, left and middle panel. The side-products upon under- and over-titrating with octamers as described in section 5.1.3 are a characteristic feature. Concomitantly, unlabeled 7N46 are formed and can be visualized alongside with the labeled 7N66 nucleosomes and the competitor DNA after staining (Figure 10 a, right panel). Considering this procedure for nucleosome formation, the total nucleosome concentration (7N66 and 7N46 nucleosomes) is increased ca. 10x over the concentration of labeled nucleosomes (section 4.3.2). This is beneficial when using highly diluted samples in single-molecule applications.

In the context of INO80 nucleosome sliding and binding (section 5.2), it was of interest to compare wild-type nucleosome substrates to nucleosomes lacking all histone tails. I therefore successfully applied the outlined histone octamer titration scheme using globular (that is, all tailless) histone octamers (Figure 10 b), provided by Kevin Schall, Gene Center and Department of Biochemistry, LMU Munich. Given the reported reduced

stability of nucleosomes in the absence of histone tails (discussed in section 2.3.2) (Ferreira et al., 2007b; Iwasaki et al., 2013) the discrimination of homogenously assembled nucleosomes from samples that harbor distinct by-products is particularly valuable for those constructs. In this way, sample quality can be ensured by native PAGE prior to all single-molecule applications.
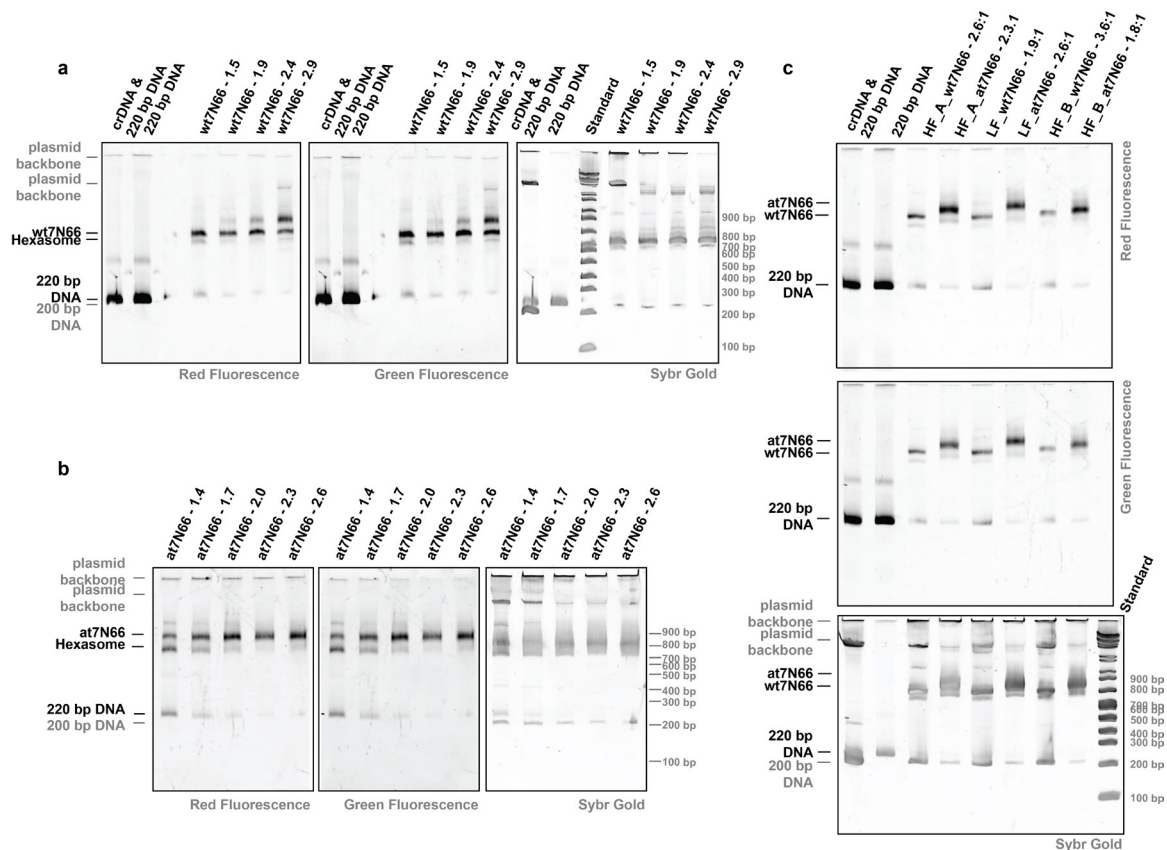

Figure 10. Assembly of smFRET applicable mononucleosomes.
(a) Native PAGE (6 %) of nucleosome assembly for the wtLF construct. Separate single channel fluorescence readouts (red, left panel and green, middle panel) are shown. Image of the same gel after SybrGold staining in the left panel. (b) Native PAGE (6%) of nucleosome assembly for the atLF construct presented as in (a). (c) Native PAGE (6%) of independent nucleosome assemblies for each of the six nucleosome constructs wtHF_A, atHF_A, wtLF, atLF, wtHF_B, atHF_B used for smFRET measurements; separate single channel fluorescence readouts (red, top panel and green, middle panel) are shown. Image of the same gel after SybrGold staining in the bottom panel. See also appendix 12.2. Nucleosome constructs LF, HF_A and HF_B only differ in label positions on the nucleosome DNA moiety (detailed description in section 5.2.1). Fluorescence imaging: ChemiDocMP. Molar ratios of octamer:601-seq DNA are indicated for each lane. (wt) *wild-type*, (at) *all tailless*. The lanes containing only DNA (crDNA & 220 bp or 220 bp DNA) do not report on the efficiency of the assembly *per se* (section 4.3.2). Dr. Mara Guariento, Institute of Biophysics, Ulm University, helped with the realization of most nucleosome assemblies presented here. Figure 10 is adapted from Schwarz et al. (2018).

Generally, the formation of homogenously assembled nucleosomes exploiting the presence of characteristic by-products for samples that have been under- or over-titrated with histone octamers was very reproducible also for other nucleosome constructs. All

mononucleosomes presented have been selected after performing an individual histone octamer titration per construct (data not shown). The achieved sample homogeneity renders each nucleosome construct highly suitable for single-molecule FRET applications. Selected titrations from the nucleosome assembly of different wild-type and all tailles nucleosomes, differing only in the position of the labels on the DNA (details in section 5.2.1), are summarized in Figure 10 c and appendix 12.2.

5.1.7   Overview on repositioned mononucleosomes used in smFRET

Each assembled nucleosome can be assigned to a distinct FRET efficiency (section 5.2.3). In order to understand the nucleosome sliding reaction, it is crucial to know as well the FRET efficiency of the repositioned mononucleosome after INO80 mediated nucleosome sliding. Therefore, I performed remodeling reactions on each smFRET applicable mononucleosome construct and verified manifest nucleosome sliding by native PAGE (Figure 11) before applying the same (diluted) sample to single-molecule FRET applications (Figure 13, section 5.2.3). A shortcoming of this approach is the high competitor DNA concentration (~10 ng/µl) in the ensemble reaction (section 4.6.2), a leftover from the nucleosome assembly (section 5.1.6) that competitively inhibits the reaction, especially since the INO80 complex prefers DNA over nucleosome binding (section 5.1.4). Still, the INO80 complex shifts the majority of nucleosomes to a new position on DNA (as illustrated by the intensity profiles depicted in Figure 11) in these remodeling conditions. The INO80 complex is assumed to mainly center the 7N66 nucleosomes, as for 0N70 nucleosomes it was previously shown that INO80 predominantly repositions 0N70 by 36 bp, sliding 78 % of the nucleosomes in total (Udugama et al., 2011).

More stringent conditions suggest comparable INO80 mediated remodeling (tested with smFRET for the construct presented in Figure 11 a, see appendix 12.3), but it is difficult to assess whether or not the degree of completion of the ensemble nucleosome sliding reaction (section 4.6.2) on the time scale tested is equivalent to the end point of the reaction. Still, mononucleosomes that have been repositioned by INO80 (*ensemble* approach) can be tested for manifest repositioning by native PAGE and thus constitute an ideal control sample for smFRET measurements that probe INO80 nucleosome sliding (section 5.2.3). Of note, repositioning of all-tailless nucleosomes is comparable to wild-type nucleosomes when analyzed by native PAGE (appendix 12.2) and pronounced when analyzed by smFRET (section 5.2.5).
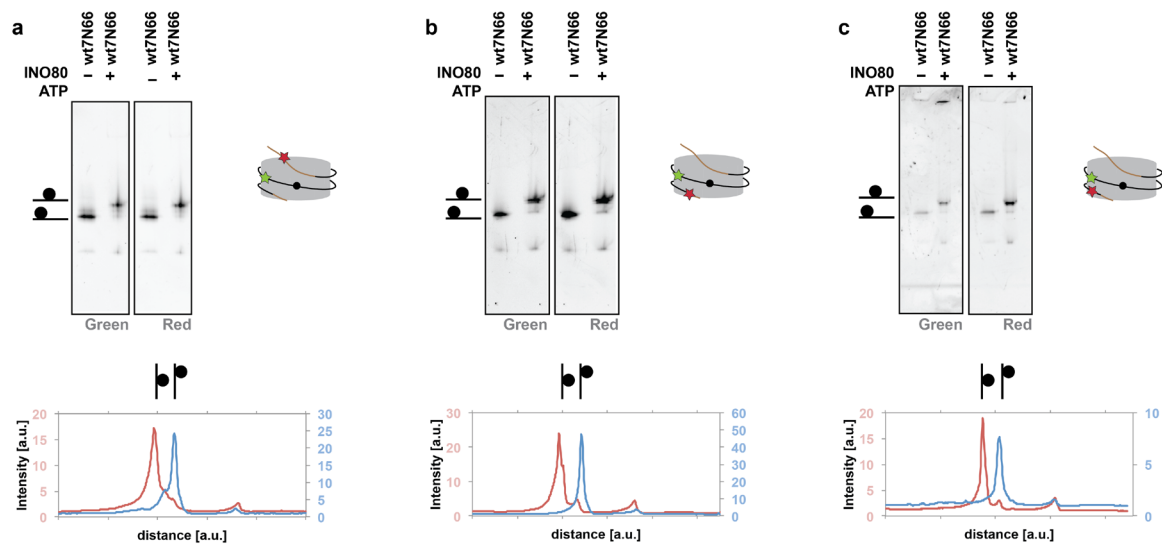
Figure 11. Overview of end-positioned and repositioned wild-type mononucleosome constructs.
(a) Native PAGE (fluorescence readouts for the acceptor fluorophore, red, or for the donor fluorophore, green) of wtLF compared to the repositioned wtLF nucleosome. Fluorescence intensity profiles are also shown (educt, blue vs. product, red). (b) wtHF_A compared to the repositioned wtHF_A nucleosome; representation as in (a). (c) wtHF_B compared to the repositioned wtHF_B nucleosome; representation as in (a). Nucleosome constructs LF, HF_A and HF_B only differ in label positions on the nucleosome DNA moiety (detailed description in section 5.2.1). Note that each intensity profile has a different scaling as indicated by the color of the y-axis caption. Figure 11 is adapted from Schwarz et al. (2018). Repositioning of all-tailless nucleosomes is comparable (appendix 12.2).

5.2 INO80-nucleosome interactions probed by smFRET

5.2.1 Overview of nucleosome constructs

The nucleosome is a structurally well characterized particle (Davey et al., 2002; Luger et al., 1997a; Vasudevan et al., 2010) and thus ideally suited for the design of FRET probes. In this study, the 7N66 constructs contain the NCP flanked by 7 bp and 66 bp of overhang DNA, respectively. The constructs "Low FRET" (LF) probes the conformation of the entry DNA, while the "High FRET A" (HF_A), "High FRET B" (HF_B) constructs probe the nucleosomal DNA in the vicinity of the DNA exit site (Figure 12). Similar constructs have been used previously (Sundaramoorthy et al., 2017; Treutlein, 2012). For unambiguous designation of the label positions, each label is named by its placement on the forward (F) or reverse (R) strand, with the number of bases plus (p, 3' direction) or alternatively minus (m, 5' direction) counted from the dyad onwards. The LF construct, for example, is designated Fp13(Tamra6)Rm84(Alexa647). The predicted distance of mean dye positions for LF, HF-A and HF-B are 76 Å, 50 Å and 15 Å, respectively (Table 9) (determined with the procedure described in section 4.8.1).
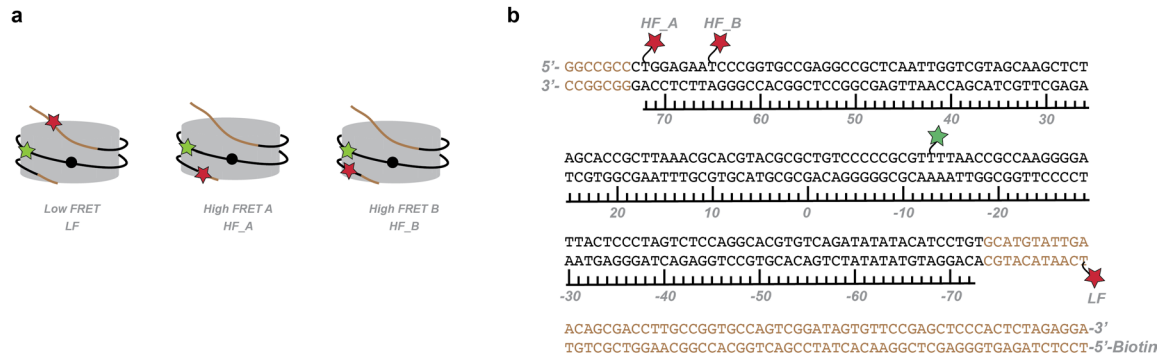
Figure 12. Schematic illustration of nucleosome constructs Low FRET (LF), High FRET A (HF_A) and High FRET B (HF_B).
(a) Label positions on the NCP for LF, HF_A and HF_B. Green star, Tamra6; red star, Alexa647; black dot, dyad; brown stroke, flanking DNA protruding from the NCP. **(b)** DNA sequence for the 7N66 constructs with label positions as in (a). Those label positions have been used previously (Sundaramoorthy et al., 2017; Treutlein, 2012). A base-pair ruler illustrates the positions on the NCP for the 145 bp that wrap the nucleosome in case of the Widom 601-sequence (Makde et al., 2010; Vasudevan et al., 2010). Brown letters, flanking DNA; black letters, 147 bp nucleosome core DNA. Figure 12 is adapted from Schwarz et al. (2018).

5.2.2 Expected remodeling intermediates and products

To estimate the FRET efficiency changes induced by INO80 nucleosome repositioning, I expect that after quenching the remodeling reaction and thermally relaxing the nucleosomes to a new stable position, canonical nucleosome conformations that are energetically favored might form. Nucleosomes intrinsically position such that at regions where histones H3/H4 contact the minor groove of the DNA helix, the DNA is most flexible (McGinty and Tan, 2015), that is at the so called "pressure points" 5 bp away from the dyad and further in 10 bp intervals (Chua et al., 2012; McGinty and Tan, 2015). A 10 bp-periodicity was also observed for sequences with high affinity for octamers and demonstrated using statistical evaluation of SELEX generated data (Lowary and Widom, 1998). Therefore, stable remodeling intermediates/products might mainly occur after repositioning by 10 bp, 20 bp or 30 bp. Indeed, 10 bp intervals were observed for repositioned nucleosomes (in the context of the 601-seq) after incubation with ACF, quenching and thermal relaxation, when applying smFRET to readout the final nucleosome position (Blosser et al., 2009). The expected distances of mean dye positions (inferred as described in section 4.8.1) after 10 bp, 20 bp and 30 bp nucleosome movement for the nucleosome constructs used in this work (LF, HF_A and HF_B) are summarized in Table 9. The assay development described herein was motivated by previous nucleosome-based smFRET studies of the single-subunit remodeler Chd1 that used similar nucleosome constructs (Sundaramoorthy et al., 2017; Treutlein, 2012).

Table 9. Expected distances of mean dye positions for hypothetical (see text) nucleosome movement in 10 bp intervals.

The respective expected new label positions are indicated for each new nucleosome position and have been used to determine the expected distance of mean dye positions using FPS calculations (Kalinin et al., 2012). Bold label positions are located on the NCP, others on the flanking DNA. The expected FRET efficiency (E) is given for the isotropic Förster radius (R_0) and a range of expected FRET efficiencies is given for $R_0 \pm 7\%$ (section 4.7). The observed FRET efficiencies have been determined by TIRF microscopy (sections 5.2.3 and 5.2.5) and complete fit results of the respective histograms are listed in the appendix 12.3.

	educt	10 bp	20 bp	30 bp
	7N66	17N56	27N46	37N36
LF	**Fp13**Rm84	**Fp3**Rm74	**Fm7Rm64**	**Fm17Rm54**
expected distance	76 Å	38 Å	38 Å	36 Å
E expected	0.33	0.89	0.89	0.91
E expected given R_0 error	0.24 to 0.42	0.84 to 0.93	0.84 to 0.93	0.87 to 0.94
E observed (wtLF)	μ: 0.48 σ: 0.06	μ: 0.85 σ: 0.07		
E observed (atLF)	μ: 0.37 σ: 0.07	μ: 0.87 σ: 0.06		
HF_A	**Fp13Fm72**	**Fp3**Fm82	**Fm7Fm92**	**Fm17Fm102**
expected distance	50 Å	35 Å	39 Å	97 Å
E expected	0.75	0.92	0.88	0.12
E expected given R_0 error	0.66 to 0.82	0.88 to 0.94	0.83 to 0.92	0.08 to 0.16
E observed (wtHF_A)	μ: 0.80 σ: 0.04	μ: 0.75 σ: 0.10, μ: 0.11 σ: 0.05		
E observed (atHF_A)	μ: 0.81 σ: 0.04	μ: 0.57 σ: 0.06, μ: 0.11 σ: 0.04		
HF_B	**Fp13Fm65**	**Fp3**Fm75	**Fm7Fm85**	**Fm17Fm95**
expected distance	15 Å	13 Å	37 Å	88 Å
E expected	0.99	0.99	0.90	0.18
E expected given R_0 error	0.99 to 0.99	0.99 to 1.0	0.86 to 0.93	0.13 to 0.25
E observed (wtHF_B)	μ: 0.96 σ: 0.03	μ: 0.68 σ: 0.09, μ: 0.13 σ: 0.05		

5.2.3 Proof-of-Principle for the smFRET readout of nucleosome repositioning

FRET efficiency histograms by TIRFM or by confocal spectroscopy of the double-labeled nucleosomes wtLF, wtHF_A and wtHF_B are overall in agreement with the expected FRET efficiencies (Table 9). Figure 13 c, f, i illustrates that each nucleosome construct displays a clearly distinct FRET efficiency of $E_\mu = 48\,\%$, $E_\mu = 80\,\%$ and $E_\mu = 96\,\%$, respectively, in TIRF microscopy. $\boldsymbol{E_\mu}$ is the mean of the FRET efficiency distribution as obtained from Gaussian fitting. Complete fit results with more than one Gaussian are summarized in the appendix 12.3. For confocal spectroscopy derived FRET efficiency histograms, peaks are centered around $E_\mu = 50\,\%$ (LF), $E_\mu = 81\,\%$ (HF_A) and $E_\mu = 93\,\%$, the latter complemented by another peak at $E_\mu = 82\,\%$ (HF_B); this is inferred from Figure 13 e, h, k, blue histograms. Notably, the HF_B construct shows a higher fraction of free DNA with a very low FRET efficiency (presumably unpacked DNA from the nucleosome assembly, section 5.1.6) than the other

two constructs. A possible explanation is that the close proximity of the labels (section 5.2.1) puts steric constraints on nucleosome packing.
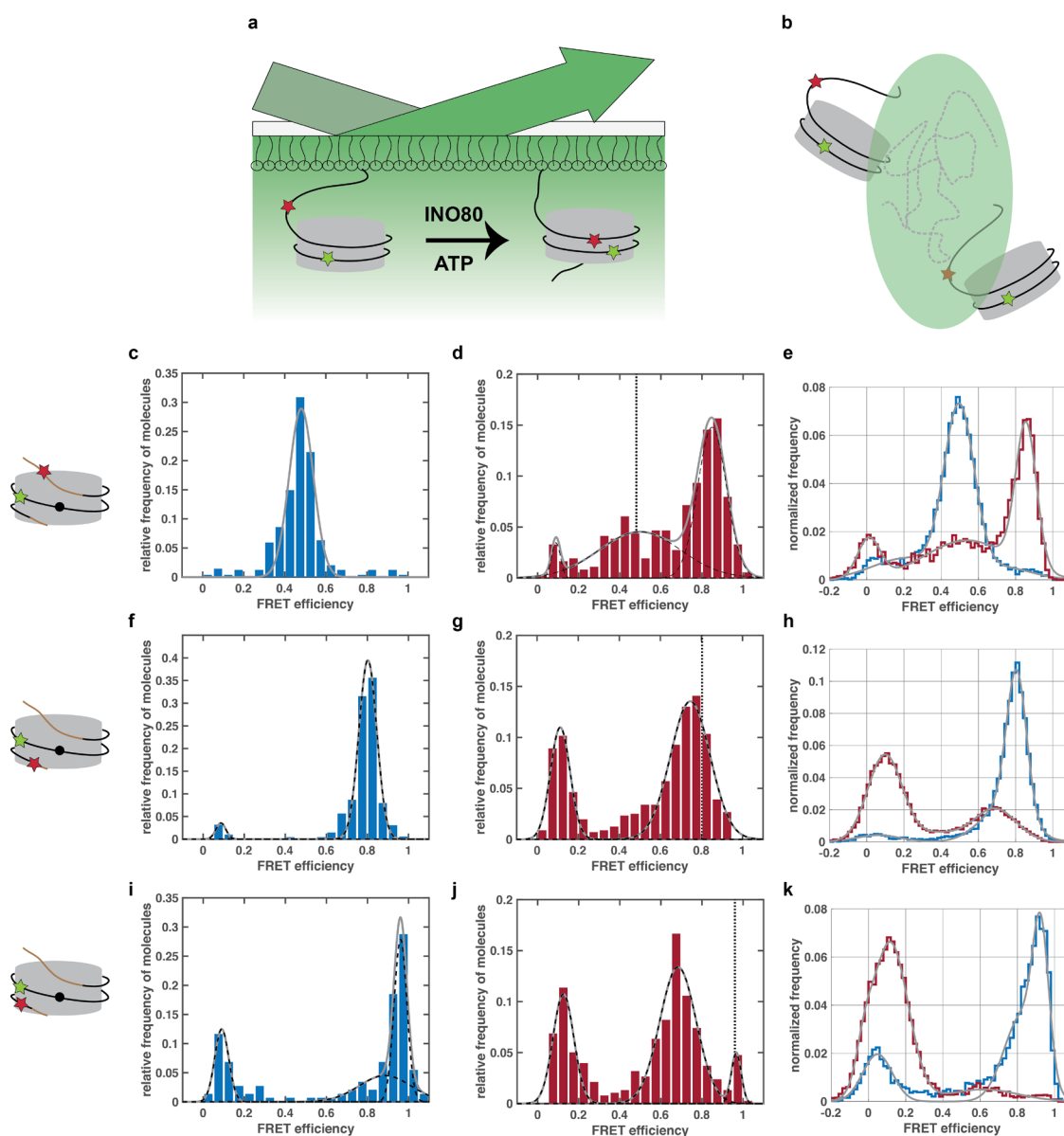

Figure 13. INO80 mediated nucleosome remodeling assayed by TIRFM and confocal spectroscopy.
(a) **Schematic overview of nucleosomes tethered to a biotinylated PEG layer on the surface of a TIRF sample chamber. The excitation laser light is introduced with a prism such that total internal reflection occurs and only near-surface fluorescent molecules are excited (shaded in green) (section 4.6.1). (b) Schematic overview of freely diffusing labeled nucleosome that pass the focal volume (shaded in green) of a confocal setup (section 4.6.2). (c, d, e) FRET efficiency histograms of the wtLF nucleosome. (c) wtLF (blue), TIRFM. (d) wtLF after remodeling (dark red), educt mean shown as dashed line, TIRFM. (e) wtLF (blue) and wtLF after remodeling (dark red), confocal spectroscopy. (f, g, h) FRET efficiency histograms of the wtHF_A nucleosome. (f) wtHF_A (blue), TIRFM. (g) wtHF_A after remodeling (dark red), educt mean shown as dashed line, TIRFM. (h) wtHF_A (blue) and wtHF_A after remodeling (dark red), confocal spectroscopy. (i, j, k) FRET efficiency histograms of the wtHF_B nucleosome. (i) wtHF_B (blue), TIRFM. (j) wtHF_B after remodeling (dark red), educt mean shown as dashed line, TIRFM. (k) wtHF_B (blue) and wtHF_B after remodeling (dark red), confocal spectroscopy. Fit results can be found in the appendix 12.3. Figure 13 c, d, e, h and k are adapted from Schwarz et al. (2018).**

In TIRF microscopy, nucleosome remodeling is performed by concomitantly adding INO80 and ATP, incubation, apyrase quenching and thermal relaxation (section 4.6.1, Figure 13 d, g, j). Construct wtLF was robustly shifted to a new position ($E_\mu = 85\,\%$, $\sigma = 7\,\%$, comprising 52 % of the data). The remodeled nucleosome position has an apparent donor-acceptor distance of ca. 50 Å. This is equivalent to a distance of mean dye positions of 42 Å ± 12 %. Herein, the apparent donor-acceptor distance was transformed to the distance of mean dye positions and the error takes into account the uncertainty of the Förster radius (67 Å ± 7 %) and the standard deviation of the FRET efficiency distribution as described in section 4.7 and as derived by Hellenkamp et al. (arXiv:1710.03807 [q-bio.QM]). The distance of mean dye positions inferred from experiments is in good agreement with any of the theoretically expected values (38 Å or 36 Å) for nucleosome repositioning on DNA by 10 bp or multiples thereof (Table 9).

Performing an ensemble remodeling reaction before confocal spectroscopy data acquisition (section 4.6.2) allows effective INO80 mediated nucleosome repositioning (Figure 13 e, h, k, dark red histograms), as validated also for the same samples by native PAGE (section 5.1.7). The apparent inter-dye distance of remodeled wtLF nucleosomes (Figure 13 e, dark red histogram) was extracted by PDA from confocal spectroscopy data as described in section 4.7 (appendix 12.3) and is ca. 49 Å. After interconversion to the distance of mean dye positions and taking the uncertainty of the Förster radius into account to determine the relative error as outlined in section 4.7 and in Schwarz et al. (2018), the distance of mean dye positions can be determined to 41 Å ± 12 %. This also matches the expected value (Table 9) and further validates the model.

Confocal spectroscopy confirms robust nucleosome repositioning by INO80 (Figure 13). For the confocal spectroscopy data of wtLF after INO80 mediated remodeling (Figure 13), 41 % of the data represent the repositioned wtLF nucleosome ($E_\mu = 86\,\%$). When the nucleosomes pass through the focal volume by diffusion and give rise to fluorescence bursts, detection may be somewhat biased for a burst of predominantly green photons compared to a burst of predominantly red photons (for the all-photon-burst search developed by Nir et al. (2006) that considers all photons independent of the excitation or emission color and given the dye combination with a γ-factor < 1, see also sections 4.6.2 and 4.8.3). In other words, the relative size of a population with respect to its FRET efficiency may be slightly underestimated for a high-FRET efficiency population (displaying mainly red fluorescence). That implies that the reported 41 % of the data for the repositioned wtLF nucleosome ($E_\mu = 86\,\%$) represent a lower limit for the

respective relative number of repositioned nucleosomes in the sample, reinforcing the notion of robust nucleosome remodeling by INO80.

Before remodeling, the apparent inter-dye distance of the wtLF nucleosome is ca. 68 Å (TIRFM). This is equivalent to a distance of mean dye positions of 66 Å ± 8 %, with the above-mentioned assumptions on distance interconversion and on error propagation, described in detail also in section 4.7. With respect to confocal spectroscopy data, these assumptions and PDA fitting reveal a distance of mean dye positions of 66 Å ± 9 %, derived from an apparent inter-dye distance of ca. 68 Å (appendix 12.3). In comparison, the expected distance of mean dye positions is 76 Å (Table 9). This small deviation of the model from the observed distance of mean dye positions in case of the educt nucleosome configuration of wtLF can be explained because the angle of the modeled overhang DNA bearing the acceptor label (section 4.8.1) with respect to the NCP is not precisely known. Therefore, theoretical distance estimations for labels that have not been placed on the known NCP structure but rely on a model including flanking DNA must not be overrated.

The interpretation of the histograms after INO80 remodeling of the wtHF_A and wtHF_B constructs is challenging. In Figure 13 g (HF_A, TIRFM), remodeling to $E_\mu = 11$ % comprises only 29 % of the data and the main peak shifts to $E_\mu = 75$ % and broadens. In Figure 13 h (HF_A, confocal spectroscopy, dark red histogram), remodeling to $E = 10$ % comprises 63 % of the data. Table 9 suggests that for HF_A, 30 bp sliding are required to substantially decrease the observed FRET efficiency, while shorter sliding distances may even lead to a slight FRET efficiency increase. To test the possibility that in the case of the wtHF_A construct, INO80 sliding for less than ~ 30 bp may not change the FRET efficiency and thus active remodeling could be masked by a very similar FRET efficiency distribution of the educt nucleosome, I tested the wtHF_B construct (Figure 12) in the same conditions. As shown in Table 9, also for wtHF_B, 30 bp sliding are expected to substantially decrease the observed FRET efficiency, however also shorter sliding distances (~ 20 bp) might lead to a FRET efficiency decrease. In Figure 13 j (wtHF_B, TIRFM), remodeling to $E_\mu = 13$ % comprises 29 % of the data; a comparable FRET efficiency population already represented 23 % of the data before remodeling as nucleosome packing on double-labeled DNA was less effective for the wtHF_B construct. Upon INO80 remodeling, also a new peak at $E_\mu = 68$ % emerges (representing 64 % of the data). Tethered nucleosomes are robustly repositioned (wtHF_B, Figure 13 j), albeit partially to a different position than observed after INO80 nucleosome repositioning in bulk conditions prior to confocal spectroscopy assessment (section 4.6.2). The latter assay (for wtHF_B) features remodeling to $E_\mu = 12$ % (comprising 81 % of the

data) complemented by a peak at $E_\mu = 0\,\%$ (comprising 7 % of the data, Figure 13 k, dark red histogram). Discrepancies between TIRF microscopy and confocal spectroscopy in the relative size of populations, defined by their respective mean FRET efficiencies, occur only for the remodeled wtHF_A and wtHF_B constructs (Figure 13). For wtLF, datasets of freely diffusing or tethered nucleosomes remodeled by INO80 confirm each other. Taking observations from confocal spectroscopy and TIRF microscopy for constructs wtLF, wtHF_A and wtHF_B into account, a complete remodeling reaction presumably relates to FRET efficiency changes from $E_\mu \sim 48\,\%$ to $E_\mu \sim 85\,\%$ (wtLF), from $E_\mu \sim 80\,\%$ to $E_\mu \sim 10\,\%$ (wtHF_A) and from $E_\mu \sim 96\,\%$ to $E_\mu \sim 12\,\%$ (wtHF_B). A presumable intermediate could have $E_\mu \sim 85\,\%$ (product-like), $E_\mu \sim 75\,\%$ (educt-like) and $E_\mu \sim 68\,\%$ (distinct from educt and product) for wtLF, wtHF_A and wtHF_B, respectively (Figure 14). A possible explanation for the observation of partially repositioned nucleosomes by TIRFM in case of wtHF_A and wtHF_B is that INO80 could be hindered due to surface interaction effects when the reaction reaches completion, because it shifts the nucleosome towards the surface of the measurement chamber by the continued sliding reaction. This explains why the intermediate remodeled nucleosome state is observed in TIRF microscopy in contrast to assays probed by confocal spectroscopy. Still, the INO80 sliding reaction, when performed with tethered nucleosomes, is not compromised for at least 10 bp. This is the minimal sliding distance that is required for the observed FRET efficiency change in case of the LF construct (Table 9).
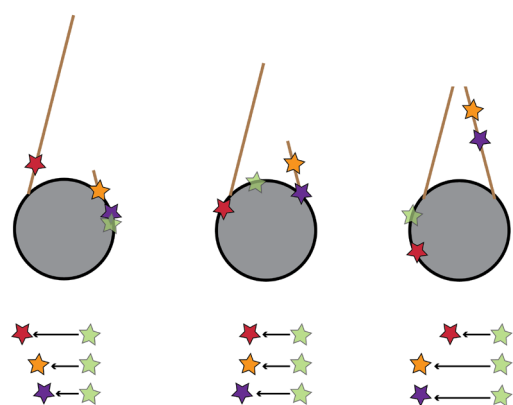

Figure 14. Cartoon of changes in label positions for 7N66 LF, HF_A and HF_B upon INO80 remodeling and thermal relaxation of nucleosomes.
(left) Educt conformation. (middle) Presumable intermediate. (right) Product conformation. (green) Donor dye for LF, HF_A and HF_B. (red) Acceptor dye for LF. (orange) Acceptor dye for HF_A. (violet) Acceptor dye for HF_B. (brown) flanking DNA. A detailed representation of the modeled accessible volumes of the dyes for the LF construct can be found in appendix 12.3.

In my own hands, one such stable intermediate for the 7N66 nucleosomes occurred in gel-based INO80 sliding assays (native PAGE, section 5.1.4). I assume that the described incomplete nucleosome repositioning by INO80 in TIRFM reflects the formation of such

an intermediate. Nucleosomes were thermally relaxed and therefore likely adopt a conformation that retains the rotational periodicity of DNA, that is being repositioned by 10 bp or multiples thereof. The distances of mean dye positions for such nucleosome conformations derived from a nucleosome model (section 4.8.1) do explain all observed FRET efficiencies of the wtLF nucleosome, but do not explain all observed FRET efficiencies of the wtHF_B nucleosome (Table 9). This discrepancy needs to be further addressed in future studies.

5.2.4 Processive nucleosome repositioning by INO80

To better understand the INO80 sliding reaction, I tested the processivity of the remodeling reaction. To this end, I used INO80 complexes pre-bound to the tethered 7N66 nucleosomes in the presence of ADP and initiated the remodeling reaction by adding ATP with a constant flow (section 4.6.1). With this experimental scenario, I excluded INO80 rebinding, thus remodeled nucleosomes are being moved by processive translocation. Here, 45 % of the data represent the remodeled wtLF construct (Figure 15 c). The FRET efficiency peak of wtLF, after remodeling, at $E_\mu = 85$ % in Figure 15 c (corresponding to a distance of mean dye positions of 42 Å ± 10 %) is in good agreement with any nucleosome repositioning on DNA by 10 bp or multiples thereof, as outlined in section 5.2.3 (Table 9). This implies that the INO80 chromatin remodeler is a processive molecular motor as discussed in detail in section 6.2. Processive nucleosome repositioning by INO80 is reflected in Figure 15 e (wtHF_A) only to some extent. This is not surprising as I inferred from section 5.2.3 that the FRET efficiency of a presumable remodeled intermediate nucleosome state likely displays a FRET efficiency that resembles the educt nucleosome state in case of wtHF_A. The fact that remodeling is generally less complete when remodeling is carried out exclusively by pre-bound INO80 complexes, compared to the conditions presented in Figure 13, is likely due to incomplete binding of substrate nucleosomes by INO80 and/or a small number of inactive remodeling complexes.

Interestingly, the INO80 bound state does not induce a marked change in FRET efficiency for the wtLF and the wtHF_A construct in TIRF microscopy (Figure 15 b, d) and for wtLF in confocal spectroscopy (Figure 15 a). However, conformational changes of the DNA path cannot be excluded, as the position of FRET labels (here on the DNA) are not sensitive to a potential distance change in any direction and greatly depend on construct design (Dimura et al., 2016).
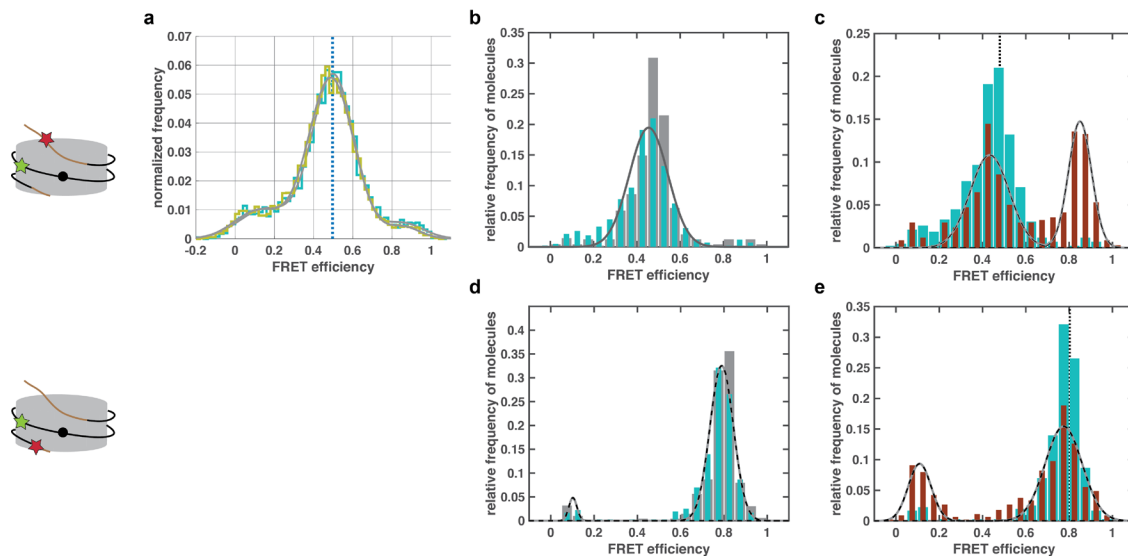
Figure 15. INO80 binding and processive sliding of wild-type nucleosomes.
(a, b, c) FRET efficiency histograms of the wtLF nucleosome. (a) wtLF in presence of INO80•ADP (39 nM dark green, 156 nM light green), confocal spectroscopy; wtLF mean shown as blue dashed line with corresponding histogram in Figure 13 e. (b) wtLF in the presence of INO80•ADP (dark green, TIRFM) compared to wtLF (grey, as in Figure 13 c). (c) bound wtLF (dark green) and wtLF after processive remodeling (brown), wtLF mean shown as black dashed line. (d, e) FRET efficiency histograms of the wtHF_A nucleosome. (d) wtHF_A in the presence of INO80•ADP (dark green, TIRFM) compared to wtHF_A (grey, as in Figure 13 f). (e) bound wtHF_A (dark green) and wtHF_A after processive remodeling (brown), wtHF_A mean shown as black dashed line. Fit results can be found in the appendix 12.3. Figure 15 a, b, c are adapted from Schwarz et al. (2018).

5.2.5 INO80 binding and remodeling for nucleosomes without histone tails

Histone tails are long extensions of the compact NCP structure with numerous functions *in vivo* (discussed in section 2.3.2). When repeating the INO80 binding assays with all tailless (at) nucleosomes, I observed a marked broadening of the FRET efficiency histogram for atLF nucleosomes in the presence of INO80 and ADP with both smaller and higher FRET efficiencies, as compared to atLF nucleosomes (Figure 16 a, b). In the presence of INO80 and ADP, the continuum of FRET states of the atLF has to be fitted with at least three Gaussians (here TIRFM data, Figure 16 b) with $E_\mu = 9~\%$, $E_\mu = 22~\%$ and $E_\mu = 48~\%$, comprising 13 %, 30 % and 57 % of the data. This indicates conformational heterogeneity and is in sharp contrast to the corresponding wtLF data (Figure 15). To exclude artifacts due to nucleosome binding to the surface of the TIRFM measurement chamber, I repeated the experiments using freely diffusing atLF•ADP•INO80 complexes, with two different INO80 concentrations (Figure 16 a), confirming the heterogeneity of conformations for the bound atLF.
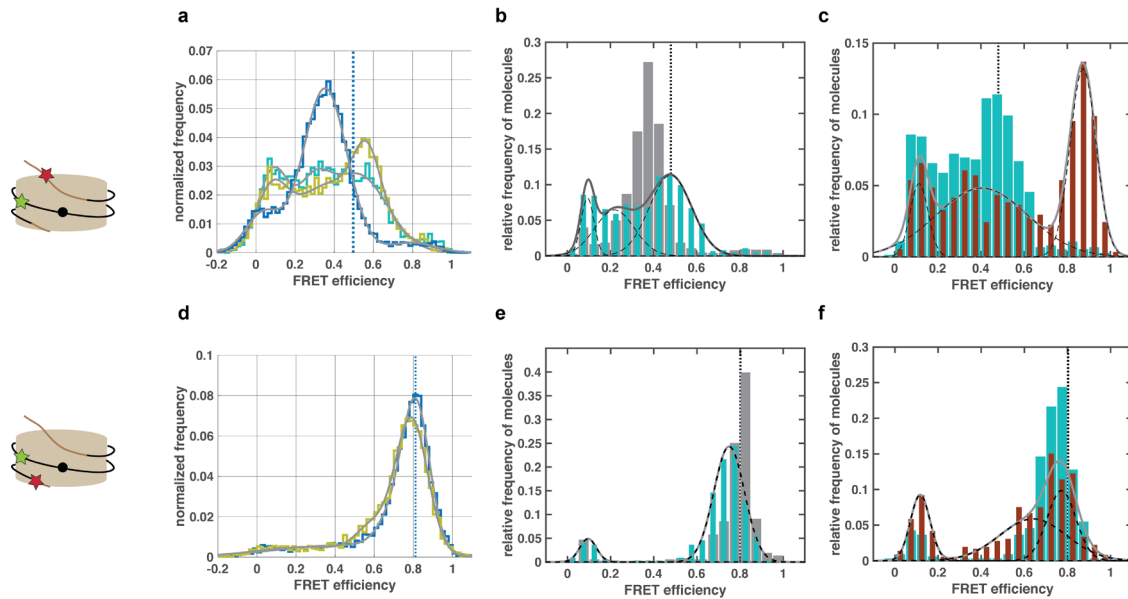
Figure 16. INO80 binding and processive sliding of all tailless nucleosomes.
(a, b, c) FRET efficiency histograms of the atLF nucleosome. **(a)** atLF (blue) and atLF in presence of INO80•ADP (39 nM dark green, 156 nM light green), confocal spectroscopy. **(b)** atLF (grey, as in Figure 17 a) in the presence of INO80•ADP (dark green) in TIRFM. **(c)** bound atLF (dark green) and atLF after processive remodeling (brown). **(d, e, f)** FRET efficiency histograms of the atHF_A nucleosome. **(d)** atHF_A (blue) and atHF_A in the presence of INO80•ADP (156 nM light green), confocal spectroscopy. **(e)** atHF_A (grey, as in Figure 17 d) in the presence of INO80•ADP (dark green) in TIRFM. **(f)** bound atHF_A (dark green) and atHF_A after processive remodeling (brown). Fit results can be found in the appendix 12.3. The absence of histone tails is implied by the brown color of the octamer core. The corresponding wt nucleosome FRET efficiency means are shown as dashed lines, respectively. Figure 16 a, b, c are adapted from Schwarz et al. (2018).

The observed multimodal FRET efficiency histogram of the atLF in the presence of INO80 and ADP likely has functional importance (section 6.3). In order to confirm a possible interpretation arguing in favor of an effect on the flanking entry-DNA conformation due to INO80 binding, I repeated the binding experiments with the atHF_A construct to probe the exit-DNA site of the nucleosome. Here, in contrast to the binding experiments that probe the DNA conformation close to the DNA entry site, only a minor change in FRET efficiencies (if any at all) is observed at the nucleosome exit-site in the presence of INO80 and ADP as seen in confocal spectroscopy (Figure 16 d, blue, $E_\mu = 81\,\%$, $\sigma = 7\,\%$, accompanied by a minor peak at $E_\mu = 70\,\%$, $\sigma = 8\,\%$ vs. bound atHF_A, light green, $E_\mu = 79\,\%$, $\sigma = 8\,\%$, accompanied by a minor peak at $E_\mu = 58\,\%$, $\sigma = 8\,\%$). This also holds true for TIRF microscopy (Figure 16 e, grey, atHF_A $E_\mu = 81\,\%$ vs. bound atHF_A, dark green, $E_\mu = 75\,\%$). Thus, the pronounced heterogeneity of conformational states for the atLF in the presence of INO80 and ADP is specific to the entry-site flanking DNA of the nucleosome.
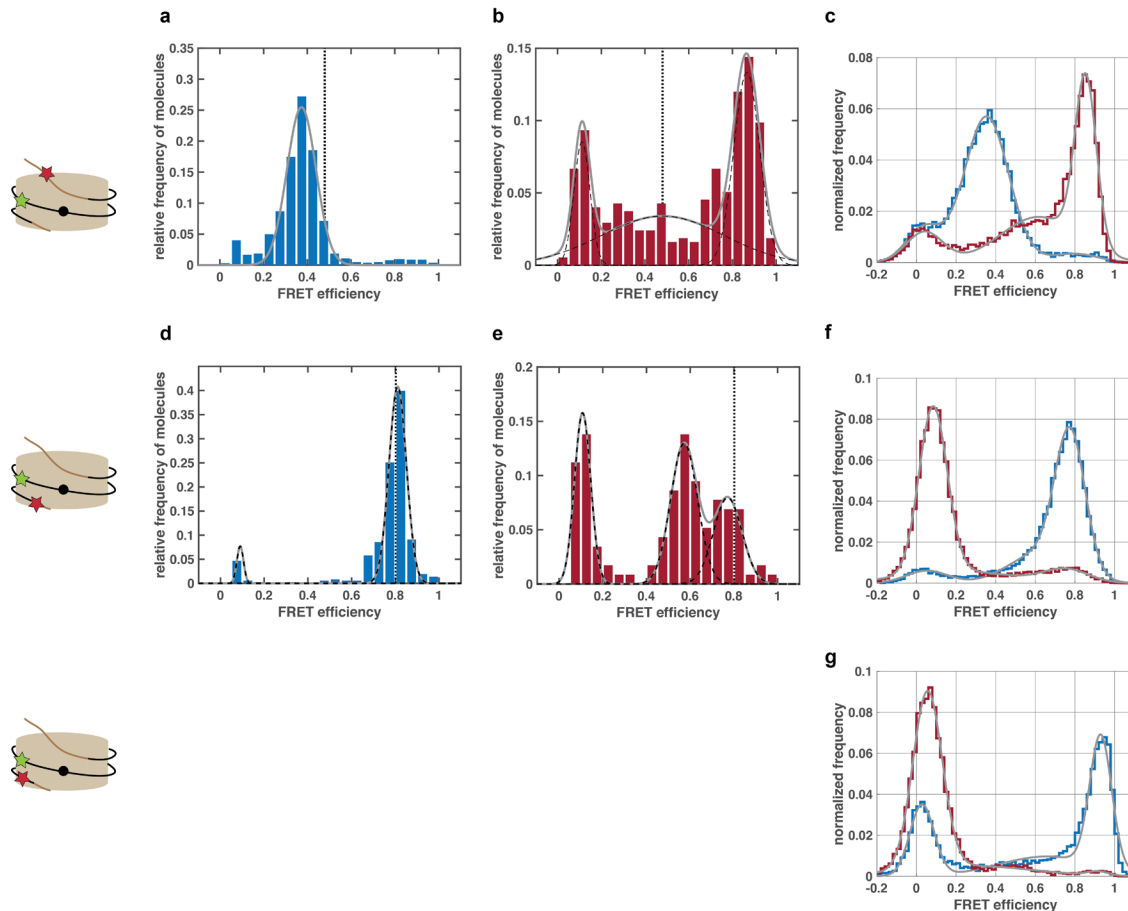
Figure 17. INO80 mediated nucleosome remodeling in the absence of histone tails assayed by TIRFM and confocal spectroscopy.
(a, b, c) FRET efficiency histograms of the atLF nucleosome. (a) atLF (blue), wtLF mean shown as black dashed line, TIRFM. (b) atLF after remodeling (dark red), wtLF mean shown as black dashed line, TIRFM. (c) atLF (blue) and atLF after remodeling (dark red), confocal spectroscopy. (d, e, f) FRET efficiency histograms of the atHF_A nucleosome. (d) atHF_A (blue), wtHF_A mean shown as black dashed line, TIRFM. (e) atHF_A after remodeling (dark red), wtHF_A mean shown as black dashed line, TIRFM. (f) atHF_A (blue) and atHF_A after remodeling (dark red), confocal spectroscopy. (g) atHF_B (blue) and atHF_B after remodeling (dark red), confocal spectroscopy. Fit results can be found in the appendix 12.3. The absence of histone tails is implied by the brown color of the octamer core. Figure 17 a, b, c, f and g are adapted from Schwarz et al. (2018).

Most experiments presented in this study use ~ 39 nM INO80. This is in a regime of > 90 % of nucleosomes bound by INO80 as observed with EMSAs (Figure 9). At least 90 % binding is therefore also expected for highly dilute nucleosome samples (section 4.6.1) in TIRF microscopy nucleosome-INO80 binding experiments (Figure 15 b, d and Figure 16 b, e). Confocal spectroscopy, as performed in this study, requires sample preparation with a ca. 20 fold higher concentration of labeled nucleosomes when compared to the sample preparation for TIRF microscopy (sections 4.6.2 and 4.6.1). Therefore, sub-saturating INO80 concentrations in combination with the residual competitor DNA from the nucleosome assembly (section 4.3.2) may

lead to an apparent reduction of INO80 complexes available for nucleosome binding, especially since the affinity of INO80 to DNA is higher than for nucleosomes (section 5.1.4). This was addressed by using saturating INO80 concentrations for a subset of confocal spectroscopy measurements. This approach confirmed heterogeneous nucleosome conformations for atLF•ADP•INO80 and the homogeneous nucleosome conformation for wtLF•ADP•INO80 (Figure 15 a and Figure 16 a). This likely implies INO80 mechanistic features upon initiation of remodeling that are caused by nucleosome histone tails (discussed in section 6.3) given the equivalent INO80-nucleosome binding properties (wild-type vs. all tailless) in *ensemble* experiments (section 5.1.5).

The FRET efficiency histogram of the atLF nucleosome in TIRF microscopy (Figure 17 a, blue, equivalent to Figure 16 b, grey) inherently shows a somewhat decreased FRET efficiency compared to wild-type nucleosomes ($E_\mu = 37\,\%$, $\sigma = 7\,\%$, atLF, in contrast to $E_\mu = 48\,\%$, $\sigma = 6\,\%$, wtLF). This is confirmed by confocal spectroscopy data (Figure 17 c, blue equivalent to Figure 16 a, blue) with $E_\mu = 35\,\%$, $\sigma = 11\,\%$ (for atLF, in contrast to $E_\mu = 50\,\%$, $\sigma = 8\,\%$, wtLF). Overall, the observed decreased FRET efficiency for atLF vs. wtLF agrees with reported differences of the histone-DNA interactions mainly at the entry- and exit-site of the nucleosome in the absence of histone tails. This has been previously deduced from decreased nucleosome stability and increased DNA breathing of such nucleosomes (Bintu et al., 2012; Brower-Toland et al., 2005; Ferreira et al., 2007b; Iwasaki et al., 2013). Given the comparable standard deviations for wtLF and atLF nucleosomes, the atLF displays a defined (but somewhat different) entry DNA conformation in the absence of histone tails. For the atLF nucleosome, the model-derived initial distance of mean dye positions (76 Å, see also Table 9) is in quantitative agreement with the distances of mean dye positions derived from experimental data. These are 73 Å ± 8 %, TIRF microscopy, inferred from Figure 17 a, and 74 Å ± 9 %, inferred from confocal spectroscopy data (Figure 17 c) by PDA (appendix 12.3).

For wtLF, I showed that INO80 accomplishes processive nucleosome repositioning. Importantly, the INO80 complex also remodels the atLF in a processive manner (Figure 16 c), resulting in a sharp peak centered at $E_\mu = 87\,\%$ comprising 39 % of the data. For the atHF_A nucleosome assayed with the same protocol (Figure 16 f), a new and unusually broad peak arises at $E_\mu = 64\,\%$, $\sigma = 15\,\%$ (46 % of the data). Additionally, 21 % of the data (compared to 7 % of the data before remodeling) display a FRET efficiency of $E_\mu = 12\,\%$, $\sigma = 5\,\%$ due to processive INO80 sliding. In order to better understand the underlying nucleosome repositioning events that lead to these observed

FRET efficiencies, I added INO80 and ATP concomitantly instead (Figure 17 e). New histogram peaks for atHF_A centered at $E = 11\,\%$ (31 % of the data) and $E = 57\,\%$ (42 % of the data) occur. Observing two clearly defined peaks instead of a broadened FRET efficiency distribution with this approach can be explained because generally more nucleosomes are being repositioned for simultaneous INO80•ATP incubation due to continuous rebinding of the remodeler (compared to nucleosomes repositioning by pre-bound INO80, see also section 5.2.4). Taken together, processive nucleosome sliding of all tailless nucleosomes was revealed with an INO80 chase experiment, that is, infusing ATP containing buffer into the sample chamber that has been loaded with nucleosomes, INO80 and ADP (section 4.6.1, applied also in section 5.2.4) and this is best illustrated by the FRET efficiency change observed for atLF (Figure 16 c).

A presumable nucleosome configuration that reflects incomplete INO80 mediated repositioning was indistinguishable from the respective educt nucleosome conformation by comparing FRET efficiencies in case of wtHF_A (section 5.2.3). An equivalent remodeling intermediate of atHF_A can be unmasked in the absence of histone tails (Figure 17 e). This rational assumes that the exiting flanking DNA has a different conformation for the all tailless compared to the wild-type situation (similar to the somewhat different wtLF vs. atLF nucleosome entry DNA conformation). Indeed, the histogram for the remodeled atHF_A nucleosome (Figure 17 e, TIRFM) is distinct from its unremodeled counterpart (Figure 17 d, TIRFM). Therefore, the results obtained for INO80 remodeling of all tailless nucleosomes strongly support the interpretation given in section 5.2.3, namely that when INO80 acts on tethered 7N66 nucleosomes, both an intermediate remodeled state and the product nucleosome conformation are observed. Concurrently, INO80 remodeling of the same nucleosome in ensemble conditions, assayed with confocal spectroscopy is more complete (Figure 17 f for atHF_A). A partially remodeled nucleosome intermediate for wild-type nucleosomes can be unmasked with a different acceptor label position as exemplified for wtHF_B (in contrast to wtHF_A, section 5.2.3). As discussed in section 5.2.3 for wild-type nucleosomes, discrepancies in the relative size of populations (TIRFM vs. confocal spectroscopy) occur. Here, a population is defined by its respective mean FRET efficiency and therefore represents the educt, intermediate or product remodeled nucleosome state or a mixture of two of these states, respectively (section 5.2.3). The data on all tailless nucleosomes further support the explanation given in section 5.2.3 that the continued remodeling reaction (intermediate to product nucleosome conformation) may be hindered by surface

interaction effects, as the nucleosome approaches the surface of the measurement chamber upon repositioning by INO80.

As seen by confocal spectroscopy (Figure 17 c, dark red histogram), atLF is robustly shifted to a new position by INO80 ($E = 85\,\%$, $\sigma = 5\,\%$, 44 % of the data) and nucleosome integrity is fully maintained. The unremodeled counterpart largely disappears when compared to the nucleosome educt (Figure 17 c, blue histogram) due to the characteristic FRET efficiency increase. The analogous histogram in Figure 17 b, obtained by TIRF microscopy (and also in Figure 16 c, brown histogram, obtained without quenching) features a peak at decreased FRET efficiency in addition to the established FRET increase after INO80 treatment. Given that the INO80 complex robustly binds nucleosomes in the absence of additional nucleotides (section 5.1.4), it is unlikely that apyrase treatment (applied to quench remodeling in the sample chamber of the TIRF microscope, section 4.6.1) effectively removes the remodeler from all nucleosome. Therefore, a fraction of nucleosomes that remains bound by INO80 throughout active repositioning and apyrase treatment (TIRFM) could partially explain the discrepancy between TIRFM and confocal spectroscopy histograms (Figure 17 b vs. Figure 17 c, dark red histogram). In contrast, nucleosomes as assayed by confocal spectroscopy are devoid of residual INO80 binding as the remodeling reaction has been quenched more rigorously by addition of λ-DNA (section 4.6.2). Additionally, if all tailless nucleosomes were less stable than wild-type nucleosomes, a small fraction of disintegrating nucleosome may contribute to the number of observed molecules with a low FRET efficiency in TIRF microscopy after INO80 atLF remodeling. When incubating atLF nucleosomes in the sample chamber for a time comparable to the duration of the experiments (section 4.6.1 and Table 8), > 90 % of the surface tethered atLF nucleosomes were stable. In summary, in the TIRFM approach probing nucleosomes after remodeling, a small number of all tailless nucleosome may remain bound to residual INO80 or may have disintegrated. Both effects can explain why a low FRET efficiency population arises in TIRFM but not in a similar assay probed by confocal spectroscopy.

Importantly, the INO80 and ATP dependent occurrence of the FRET efficiency peak at $E = 87\,\%$ (comprising 39 % of the data) for atLF (Figure 16 c, Figure 17 b, TIRFM) points to comparable nucleosome sliding as for wild-type nucleosomes. The corresponding distances of dye mean positions for repositioned surface-tethered nucleosomes are 40 Å ± 11 % (Figure 16 c) and 41 Å ± 11 % (Figure 17 b), respectively,

and agree with expected distances of mean dye positions for an intact NCP (Table 9), as well as with the distance of mean dye positions derived from confocal spectroscopy (42 Å ± 12 %).

5.2.6 Characterization of nucleosome acceptor dye qualities upon INO80 binding

Further characterization of INO80 binding with a saturating INO80 concentration (156 nM) can be accomplished by fluorescence lifetime and anisotropy analyses of the multiparameter fluorescence detection derived data acquired with confocal spectroscopy (section 4.6.2 and 4.8.3). Both lifetime and anisotropy are sensitive to the local dye environment. In this regard, an increase in the apparent fluorescence lifetime upon protein binding has been attributed to an increased fluorophore quantum yield (Stennett et al., 2015), a phenomenon described earlier as protein induced fluorescence enhancement (PIFE) (Hwang et al., 2011). Likewise, the vicinity of protein moieties with respect to the dye molecule potentially constrains its rotational freedom, resulting in a change in anisotropy. A possible explanation could be that the fluorophore transiently interacts with the protein surface. Thus lifetime and anisotropy measurement of the acceptor dye (Alexa647) of the LF nucleosome confirm INO80 binding to nucleosomes. The effect becomes most apparent in 2D lifetime vs. anisotropy histograms (Figure 18 a, b).

For wtLF, the acceptor lifetimes increase upon INO80 binding, as expected for PIFE (Figure 18 a, blue vs. green) and concomitantly the anisotropy increases. Interestingly, when the acceptor dye is moved onto the NCP due to repositioning resulting in nearby histone proteins, a similar, though not identical, change in acceptor lifetimes and anisotropy is observed (Figure 18 a, blue vs. red). Both lifetime histograms for the acceptor dye in the vicinity of proteins (Figure 18 a, green, red) have a multimodal distribution. This heterogeneity may result from a small fraction of nucleosomes that are not bound or may not have been remodeled by INO80, respectively. Alternatively, histone proteins and/or INO80 subunits that get close to the acceptor dye could give rise to different acceptor lifetimes if the bound/remodeled nucleosome had different conformations that in turn impact the acceptor to different extends. Notably, both explanations are not mutually exclusive and might contribute to the outlined acceptor lifetime properties. Concomitantly, the anisotropy histogram of the acceptor dye shows that dye rotation is restricted to a different degree depending on the dye environment (Figure 18 a, Figure 18 b).

Convincingly, also INO80 bound atLF (Figure 18 b, green) as well as remodeled atLF (Figure 18 b, red) display similar lifetime and anisotropy histograms for the acceptor dye in the vicinity of proteins, while being markedly different from the atLF educt (Figure 18 b, blue). Further, the absolute change in lifetime and anisotropy upon INO80 binding/after remodeling are more pronounced for atLF (compared to wtLF, Figure 18 a vs. b). For the respective reference sample, atLF, both lifetime and anisotropy histograms are shifted to smaller values compared to wtLF (Figure 18 a vs. b, blue). Therefore, effects on both parameters by binding/remodeling become more obvious for atLF. These differences between atLF and wtLF acceptor lifetime and anisotropy are in agreement with the proposed difference in flanking DNA coordination by the octamer core in the absence of histone tails described in section 5.2.5, which might well position the acceptor label out of reach of protein moieties in case of atLF. Taken together, these results highlight once more pronounced INO80 binding to atLF and wtLF, specifically in confocal spectroscopy measurement conditions, while both binding scenarios are markedly different.
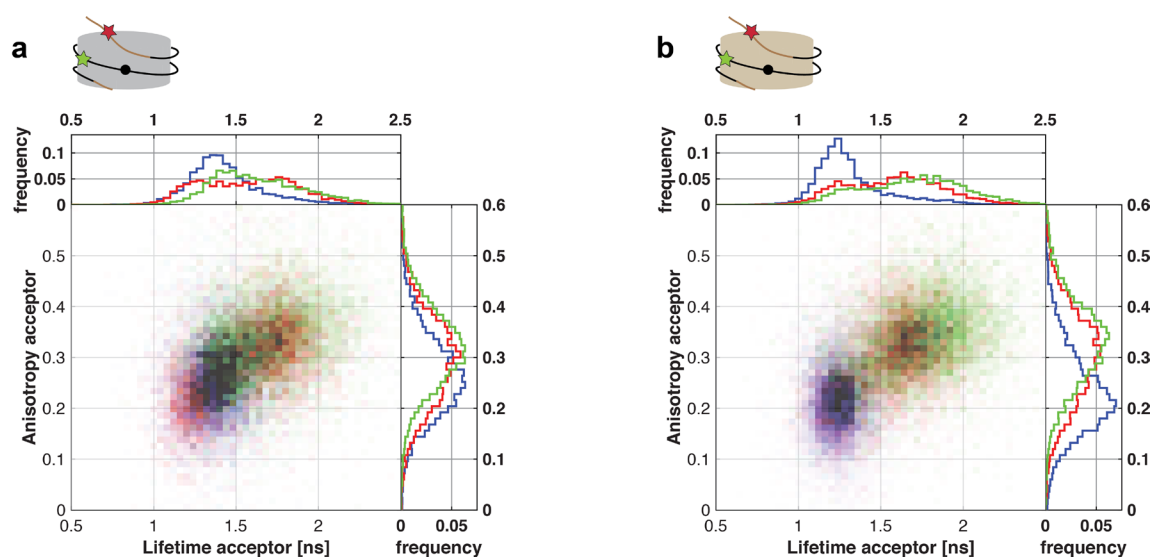
Figure 18. Changes in acceptor dye properties upon INO80 binding/remodeling of wild-type and of all tailless nucleosomes (confocal spectroscopy).
(a) Acceptor dye properties of wtLF (blue, dataset as in Figure 13 e) compared to wtLF in presence of 156 nM INO80 and ADP (green, dataset as in Figure 15 a) and compared to remodeled wtLF (red, dataset as in Figure 13 e). (b) Acceptor dye properties of atLF (blue, dataset as in Figure 17 c) compared to atLF in presence of 156 nM INO80 and ADP (green, dataset as in Figure 16 a) and compared to remodeled atLF (red, dataset as in Figure 17 c). A direct comparison of the histograms of wild-type vs. all tailless nucleosomes can be found in the appendix 12.3 for each condition.

A similar readout for the donor fluorophore is not presented, as changes in donor lifetime generally are also caused by changes in FRET efficiency (with a minor reservation of this rational if FRET efficiencies dynamically switch on timescales faster than the duration of a fluorescent burst). FRET efficiency distributions have been described in detail (sections 5.2.3, 5.2.4 and 5.2.5). Notably, PIFE is not expected to occur for the Tamra6 dye (rhodamine dye), as previous studies on PIFE rely on cyanine dyes (Hwang et al., 2011; Hwang and Myong, 2014; Ploetz et al., 2016; Stennett et al., 2015).

5.2.7 Data analysis characteristics of the presented smFRET data

Insights from confocal spectroscopy smFRET data

The determination of accurate FRET efficiencies strongly depends on key correction factors, mainly the γ-factor (Hellenkamp et al., arXiv:1710.03807 [q-bio.QM]). An ensemble of molecules with different acceptor lifetimes (Figure 18) directly implies that each subpopulation of molecules defined by a specific acceptor lifetime has an individual acceptor quantum yield. This in turn points to a change in γ-factor between subpopulations. Inappropriate γ-factor values could therefore lead to inaccurate FRET efficiencies. Despite a change in the distribution of acceptor fluorophore lifetimes when different experimental conditions for the same construct, here LF, are probed (Figure 18), FRET efficiency correction using a "compromise" γ-factor, that is one γ-factor for all nucleosomes samples with/without INO80 that relate to the same double-labeled DNA (section 4.8.3) accurately represents confocal spectroscopy data. This is illustrated by the good overall agreement with TIRF microscopy data that does not rely on the above approaches for γ-factor determination and instead uses a molecule-by-molecule derived γ-factor (section 4.8.2). The quantitative agreement of mean FRET efficiencies for most nucleosome samples probed individually by TIRFM and confocal spectroscopy (fit results in appendix 12.3) confirms the applied FRET efficiency correction for confocal spectroscopy data using a "compromise" γ-factor per DNA construct.

Insights from TIRF microscopy smFRET data

In TIRF microscopy, molecules that show first acceptor and then donor photo-bleaching are oftentimes selected as FRET events (Dörfler et al., 2017) (exemplary single molecule fluorescence time trajectories of donor and acceptor in Figure 19 a, b, c). For the calculation of their individual FRET efficiencies, it is crucial to know the γ-factor to accurately represent corrected FRET efficiencies (Hellenkamp et al., arXiv:1710.03807 [q-bio.QM]) (section 4.8.2). The γ-factor can be individually determined for each

molecule as described (Dörfler et al., 2017) for single molecule fluorescence time trajectories such as depicted in Figure 19 a, b, c.

A disadvantage of this approach is that only molecules that feature those distinct photo-bleaching steps are taken into account. Photo-bleaching preferentially occurs from distinct photo-chemically induced species that are energetically accessible from the excited state (Stennett et al., 2014). Therefore, the FRET efficiency (measured quantity) and photo-bleaching (a selection criterion for FRET molecules) are not strictly speaking independent. In order to partially overcome this limitation, I included molecules devoid of donor photo-bleaching (Figure 19 d, e) or displaying donor before acceptor photo-bleaching (Figure 19 g, h, i).

For those molecules (no donor photo-bleaching, Figure 19 d, e or donor before acceptor photo-bleaching, Figure 19 g, h, i) a global γ-factor was applied for FRET efficiency correction (section 4.8.2). This γ-factor was also applied to molecules that displayed the canonical photo-bleaching steps, but did not qualify for reasonable individual γ-factor determination, which is the case if very low FRET efficiencies at the border of the dynamic range of FRET are observed (Hildebrandt et al., 2015). I assume to observe such FRET efficiencies (that can be as low as zero FRET efficiency, equivalent to no energy transfer at all because donor and acceptor are too far apart) for few double-labeled DNA molecules that remain from the nucleosome assembly (distance on linear DNA > 70 bp, Figure 12, section 4.3.2). In summary, the presented rational to select FRET events from raw data was applied to establish unbiased selection of single-molecules that qualify for FRET efficiency histogram analysis.

All of the examples of single-molecule fluorescence time trajectories in Figure 19 are quasi-static in time, that is, no apparent jumps in FRET efficiency are visible. Static FRET efficiencies were expected, as nucleosomes in thermodynamic equilibrium were assessed by smFRET in sections 5.2.3, 5.2.4 and 5.2.5, for example after INO80 binding or after remodeling and nucleosome relaxation (sections 4.6.1 and 4.6.2). However, concomitantly a small percentage (< 4 %) of dynamic single-molecule fluorescence time trajectories occurred (examples in Figure 20). Here at least one jump in FRET efficiency is observed that is larger than the noise. These molecules are not included in the FRET efficiency histograms in sections 5.2.3, 5.2.4 and 5.2.5.
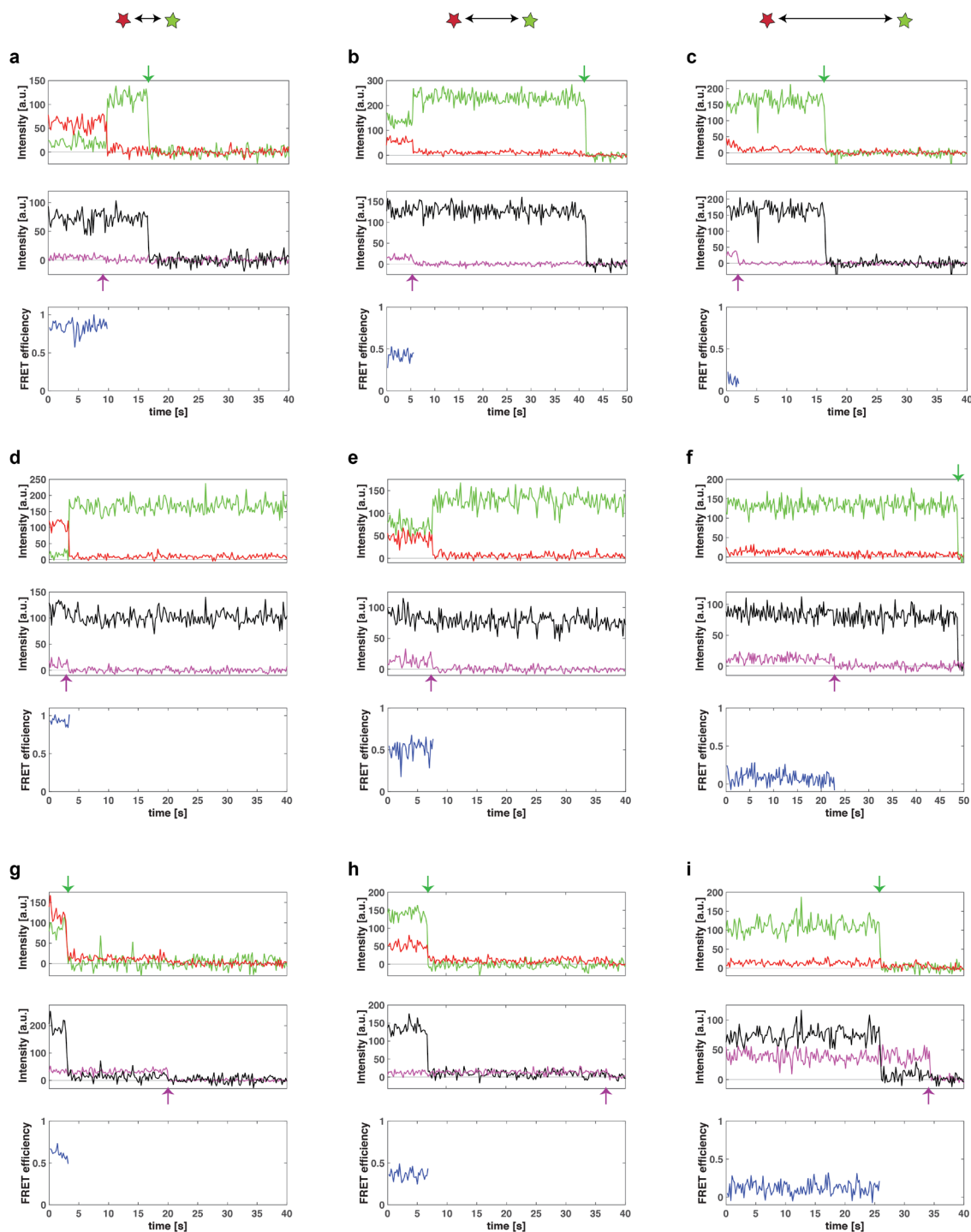
Figure 19. Exemplary static single molecule fluorescence time trajectories from TIRFM. The mean FRET efficiency of each molecule is classified in a FRET efficiency histogram.

(a, b, c) Acceptor photo-bleaching before donor photo-bleaching; FRET efficiency correction with a molecule-by-molecule individual γ-factor. (d, e) Acceptor photo-bleaching only; FRET efficiency correction with a mean γ-factor. (f) Acceptor photo-bleaching before donor photo-bleaching; FRET efficiency correction with a mean γ-factor (this molecule is inappropriate for the molecule-by-molecule individual γ-factor determination, see text). (g, h, i) Donor photo-bleaching before acceptor photo-bleaching; FRET efficiency correction with a mean γ-factor. Examples include high FRET efficiencies (a, d, g), low FRET efficiencies (b, e, h) or very low FRET efficiencies (c, f, i). Top panel: donor fluorescence after green excitation (green), acceptor fluorescence after green excitation (red), green arrow: donor photo-bleaching. Middle panel: γ-weighted sum of donor and acceptor fluorescence after green excitation (black), acceptor fluorescence after red excitation (magenta), magenta arrow: acceptor photo-bleaching. Bottom panel: Computed smFRET efficiency (blue).

84

Few (< 4 %) dynamic single-molecules were observed for educt nucleosomes (wtLF and atLF, Figure 20 a and d, respectively), nucleosomes in the presence of INO80 and ADP (wtLF, atLF, Figure 20 b, c and e, f, respectively) and after nucleosome remodeling (data not shown). In contrast, when using a protocol optimized for the observation of real-time INO80 remodeling (Table 8) a large number of dynamic single-molecule fluorescence time trajectories (up to 29 % of all molecules) were observed. This indicates that the developed assay has the potential to observe real-time remodeling dynamics and details are discussed in section 5.2.8.
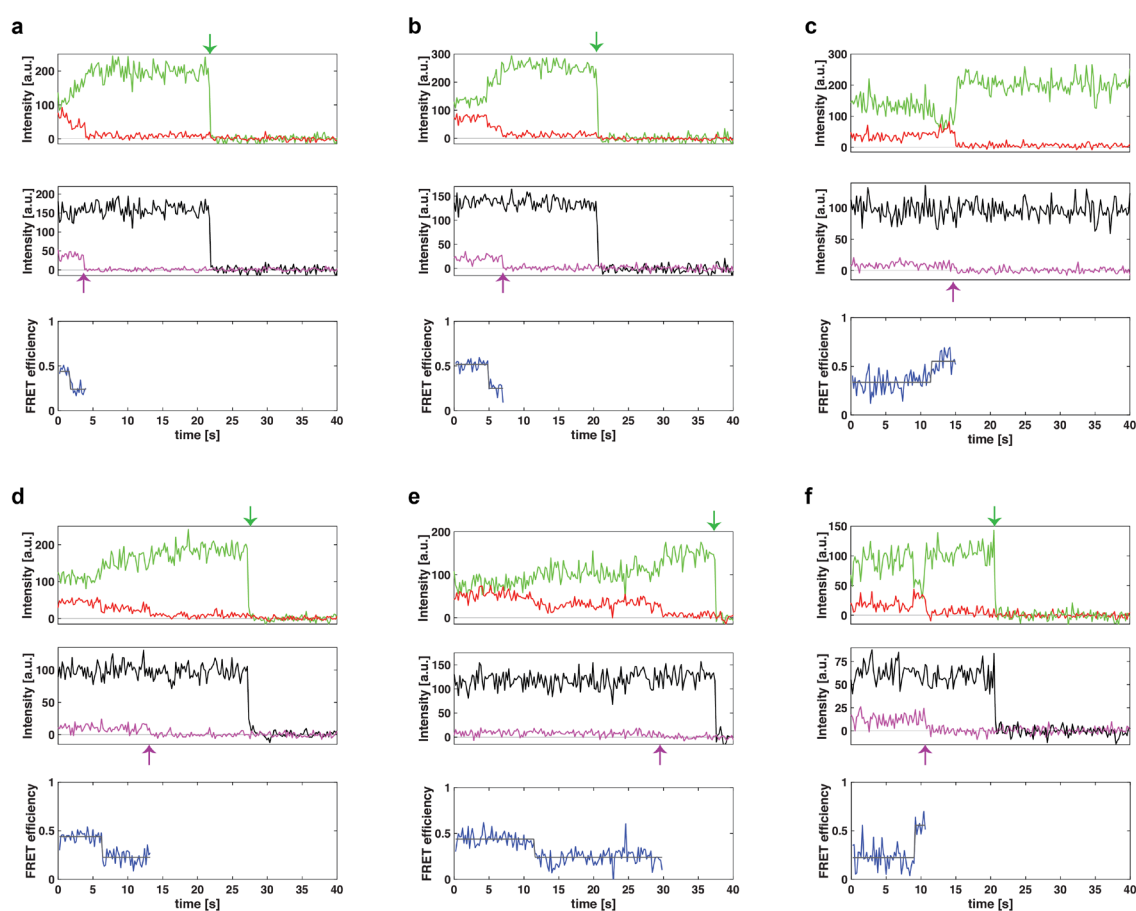
Figure 20. Examples of ATP-independent dynamic single-molecule fluorescence time trajectories for the LF nucleosome in the presence or absence of INO80 (TIRFM).
(a) **wtLF. (b, c) wtLF in the presence of INO80, 2 mM ADP. (d) atLF. (e, f) atLF in the presence of INO80, 2 mM ADP. Top panel: donor fluorescence after green excitation (green), acceptor fluorescence after green excitation (red), green arrow: donor photo-bleaching. Middle panel: γ-weighted sum of donor and acceptor fluorescence after green excitation (black), acceptor fluorescence after red excitation (magenta), magenta arrow: acceptor photo-bleaching. Bottom panel: Computed smFRET efficiency (blue), HMM fit to the smFRET efficiency (grey). Figure 20 is adapted from Schwarz et al. (2018).**

5.2.8   Real-time FRET efficiency changes of the nucleosome induced by INO80

Previous nucleosome based smFRET studies monitored nucleosome sliding in real-time, inferred from entry-DNA movement (Deindl et al., 2013), from exit-DNA movement (Blosser et al., 2009; Deindl et al., 2013; Harada et al., 2016; Hwang et al., 2014; Levendosky et al., 2016) and from DNA movement at an internal nucleosome site (Harada et al., 2016) with respect to the histone octamer core. In contrast, in the experiments described here, live remodeling events induced by INO80 can be observed for the relative change in label positions on the entry side DNA gyre of the nucleosome in case of the wtLF nucleosome (adapted conditions for live observation, section 4.6.1) (Figure 21). Example real-time FRET efficiency changes of such dynamic single-molecules are shown in Figure 21 d, g (in the presence of INO80, 0.3 mM ATP), Figure 21 e, h (repositioned wtLF in the absence of INO80 and ATP) and Figure 21 f, i (in the presence of INO80, 0.3 mM ATP and 2 mM ADP, termed herein competitive inhibition condition). In the presence of INO80 and ATP, ~29 % of the molecules are dynamic, as well as ~17 % of the molecules for the competitive inhibition condition, but only ~11 % of the repositioned wtLF molecules are inherently dynamic.

This implies that around 2/3rd of the dynamically switching nucleosomes in the presence of INO80 and ATP display INO80 induced structural changes (ideally ATP-dependent active translocation). To identify these properties molecule-by-molecule, a local HMM (section 4.8.2) was applied to each individual dynamic time trajectory (exemplarily depicted in Figure 21 d, g, e, h, f and i, bottom panel) that extracts different FRET efficiency states associated with a characteristic dwell time. Many dynamic FRET-efficiency time trajectories display short dwell times on the order of one to a few time bins à 33 ms (Figure 21 d, g, bottom panel). This phenomenon was particularly prominent in the presence of INO80 and ATP. Of note, the ALEX excitation scheme (magenta direct excitation in Figure 21 d, g, e, h, f and i, middle panel) (Hohlbein et al., 2014; Margeat et al., 2006) ensures a fluorescent (instead of a dark) state of the acceptor during real-time observation of FRET efficiency fluctuations. I next set out to infer an ATP-dependent FRET efficiency change and therefore introduced ADP as a competitive inhibitor to slow down the reaction (or in other words, to increase the Michaelis-Menten constant (K_M), Figure 21 f, i). The probability that the main ATPase is in a translocation competent ATP-bound state is reduced when introducing ADP to compete for ATP binding. The occurrence of some short dwell times persisted when introducing ADP as a competitive inhibitor (Figure 21 f). I refrain from quantitative assessment of kinetic properties related to INO80 remodeling, for example to compare different nucleotide

conditions, because data interpretation in terms of the associated absolute FRET efficiency for such short-lived states is challenging. For very short dwell times the total number of photons may not be sufficient to accurately determine the FRET efficiency (> 100 photons needed for medium accuracy (Ha and Tinnefeld, 2012)). The signal-to-noise ratio needs to be improved for data acquisition with short camera integration times (e.g. 33 ms) in order to accurately quantify the FRET efficiency of short dwell times. Still, the herein established platform for real-time observation of INO80 is a promising tool to dissect the conformational changes of the entry side DNA gyre upon INO80 mediated DNA translocation. Real-time information of INO80's interaction, in particular with the entry side DNA gyre, is highly relevant to understand INO80's mechanism (section 6.2). In that respect, the discovery of FRET efficiency fluctuations on an unexpectedly fast time scale (including dwell times on the order of tens/hundreds of milliseconds, Figure 21) likely has functional importance that is discussed in section 6.2.

Real-time observations by TIRFM as described in this study are also sensitive to investigate the inherent dynamics of nucleosomes. This is of interest for repositioned nucleosomes, given that the octamer has been shifted to a new position on the 601-seq DNA by INO80 and thus is no longer in its energetically favored position. It is therefore expected that inherent fluctuations of the nucleosomal DNA are more likely for the repositioned nucleosome sample (compared to the conventional 601-seq end-positioned educt sample). I therefore developed a protocol yielding a highly homogenous repositioned wtLF sample (section 4.6.1), associated with a very sharp FRET efficiency peak built from the static molecules ($E_\mu = 86$ %, $\sigma = 3$ %, Figure 21 b). This highly homogenous sample of repositioned wtLF also displayed dynamic FRET efficiency changes (Figure 21 e, h). Future studies are therefore required to quantify the kinetic properties of this process, which represents a detailed balance situation that does not dependent on ATP. Such knowledge could help to discriminate nucleosome dynamics from active nucleosome sliding, in particular for real-time observation datasets of nucleosome sliding in the presence of INO80 and ATP. Here, single molecules that either display dynamic nucleosome properties or active nucleosome sliding by INO80 might co-occur. Examples for real-time FRET efficiency changes by inherent nucleosome dynamics, fitted with a local HMM, are displayed in Figure 21 e, h.
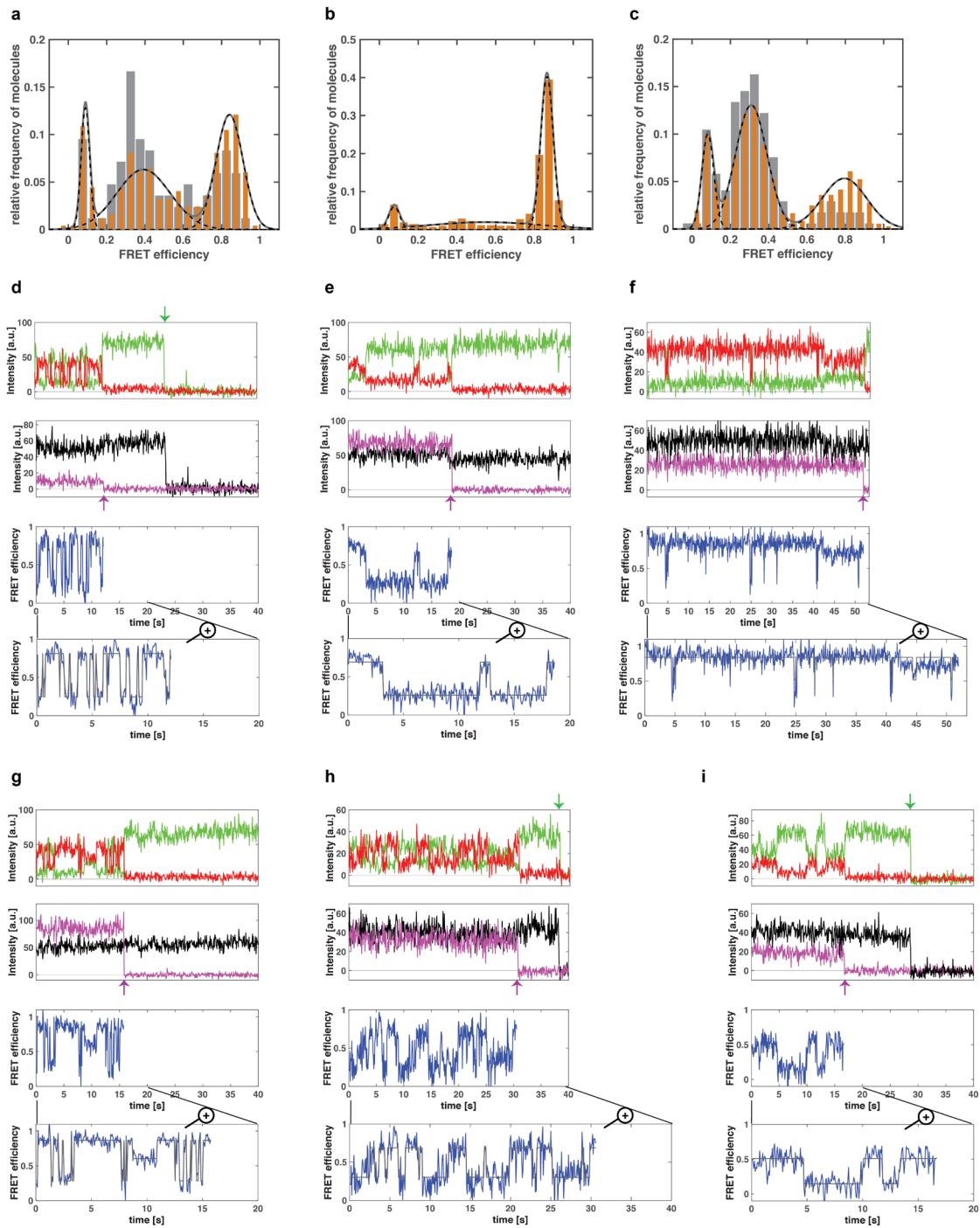
Figure 21. Real-time FRET efficiency changes of ATP-dependent wtLF nucleosome repositioning as observed by TIRFM. FRET efficiency histograms of static molecules and examples for dynamic molecules are shown.

(a) wtLF, static molecules, in the presence of INO80 and 0.3 mM ATP (orange, > 20 min incubation and grey, < 20 min incubation). (b) Repositioned wtLF, static molecules. (c) wtLF, static molecules, in the presence of INO80, 0.3 mM ATP and 2 mM ADP (orange, > 40 min incubation and grey, < 40 min incubation). (d, g) examples of dynamic wtLF molecules in the presence of INO80 and 0.3 mM ATP. (e, h) examples of inherently dynamic repositioned wtLF molecules. (f, i) examples of dynamic wtLF molecules in the presence of INO80 and 0.3 mM ATP, 2 mM ADP. (d, g, e, h, f, i) top panel: donor fluorescence after green excitation (green), acceptor fluorescence after green excitation (red), green arrow: donor photo-bleaching. Middle panel: γ-weighted sum of donor and acceptor fluorescence after green excitation (black), acceptor fluorescence after red excitation (magenta), magenta arrow: acceptor photo-bleaching. Bottom panel: Computed smFRET efficiency (blue), HMM fit to the smFRET efficiency (grey). Figure 21 d, e and g are adapted from Schwarz et al. (2018).

88

Static and dynamic fluorescence time trajectories both occur in a measurement and the static molecules were used to assess the remodeling reaction in general. Figure 21 a shows the FRET efficiency distribution of wtLF after at least 20 min incubation with INO80, 0.3 mM ATP (orange histogram). Nucleosome repositioning resulted in $E_\mu = 84\,\%$ (including 42 % of the data). At earlier time points (< 20 min, grey background histogram) less nucleosomes have been repositioned (Figure 21 a, grey background histogram). This provides evidence for robust nucleosome repositioning by INO80.

When incubating wtLF with INO80, 0.3 mM ATP, 2 mM ADP in the TIRFM measurement chamber for at least 40 min, 31 % of the nucleosomes are shifted to a new position. The associated FRET efficiency distribution has a broad peak at $E_\mu = 79\,\%$, $\sigma = 12\,\%$ (Figure 21 c, orange histogram) and is not equivalent to the previously observed well-defined wtLF FRET efficiency peaks after INO80 treatment of surface-tethered nucleosomes (Figure 13 d, Figure 15 c, Figure 21 a). Here, in contrast to the experiments described in sections 5.2.3, 5.2.4 and 5.2.5, the reaction has not been quenched. Therefore, the somewhat more heterogeneous nucleosome states do not necessarily represent a thermodynamically favored position of nucleosomes on DNA as assumed for previous experiments. A broadened FRET efficiency distribution for repositioned nucleosomes that have not been subjected to a quenching protocol is conceivable, especially since ADP was introduced to slow down the remodeling reaction (see above). Overall, nucleosomes have been repositioned with INO80, 0.3 mM ATP, 2 mM ADP, as a clear increase in FRET efficiency was observed for a fraction of the molecules.

Taken together, this study provides evidence that INO80 and ATP-dependent nucleosome remodeling can be monitored in real time by TIRF microscopy. However, the heterogeneity of the expected time-dependent events that co-occur in a given condition, such as INO80 binding, INO80 remodeling, nucleosome flexibility in the product (and educt) state, requires careful classification of the observed single-molecules in terms of FRET efficiency, dwell time and respective frequency of occurrence. At the present point, data interpretation to this level remains ambiguous due to technical challenges. As a consequence, real-time nucleosome remodeling by INO80 will be a subject of future detailed studies.

6. Discussion

6.1 Development of a nucleosome-based smFRET assay for INO80

The investigation of the INO80 nucleosome-interplay in the present study relies on concomitant application of surface- and solution-based single molecule fluorescence microscopy techniques. The FRET probes are different nucleosome constructs that have been assembled from double-labeled DNA (Figure 12) and every nucleosome is at the most double-labeled. This enables the dual TIRF microscopy and confocal spectroscopy approach that, for example, unambiguously relates the observed FRET efficiency change by INO80 and ATP to mononucleosome repositioning by INO80 (section 5.2.2). In contrast, nucleosome-based smFRET experiments of chromatin remodelers of the ISWI-subfamily, RSC and Chd1 (discussed in sections 2.4.1, 2.4.2, 2.4.4, 2.6.1 and 2.6.3) combine DNA and histone labeling and bring about nucleosomes labeled stochastically on either of the two equivalent histone copies as well as triple-labeled nucleosomes (both histones and DNA) (Deindl et al., 2013; Gamarra et al., 2018; Harada et al., 2016; Hwang et al., 2014; Levendosky et al., 2016; Qiu et al., 2017). This requires sorting individual nucleosomes into labeling classes and limits the assay to surface-based microscopy techniques (Blosser et al., 2009; Deindl et al., 2013).

In the present study, nucleosome sliding of the LF nucleosome construct induces a distinct FRET efficiency increase that is in agreement with an intact repositioned nucleosome (sections 5.2.2, 5.2.3 and 5.2.4). The data interpretation exploits the explicit relationship of FRET efficiencies to actual dye distances to provide evidence for active nucleosome repositioning. This interpretation also implies that nucleosomes adopt their canonical structure after active remodeling by INO80 and subsequent thermal relaxation (section 5.2.4). Previous surface-based smFRET experiments with the single-subunit remodeler Chd1 that rely on similar nucleosome constructs gave rise to a FRET efficiency increase for repositioned 7N46-wtLF nucleosomes (Treutlein, 2012) comparable to my observation of INO80 remodeling. Nucleosome conformational changes other then repositioning to a new stable position (for example DNA unpeeling or nucleosome disassembly) are expected to instead decrease the FRET efficiency in case of LF. Together, this confirms that nucleosome constructs derived from double-labeled DNA are highly suitable to probe the catalytic activity of the INO80 chromatin remodeler (Schwarz et al., 2018).

Other nucleosome-based single-molecule FRET studies of different remodelers report a FRET efficiency decrease upon remodeling (that ultimately even reaches the limit of the FRET dynamic range) as DNA is being actively translocated along the octamer core (here, the DNA-histone labeling scheme was used, see above) (Deindl et al., 2013; Gamarra et al., 2018; Harada et al., 2016; Hwang et al., 2014; Levendosky et al., 2016; Qiu et al., 2017). Therefore, conformational changes of nucleosomes other than sliding, for example related to nucleosome dynamics such as DNA gaping or breathing (Buning and van Noort, 2010; Fierz, 2016; Ngo and Ha, 2015) cannot be excluded when interpreting an observed FRET efficiency decrease. The smFRET remodeling assays by Deindl et al. (2013), Gamarra et al. (2018), Harada et al. (2016), Hwang et al. (2014), Levendosky et al. (2016) and Qiu et al. (2017) gain insights into nucleosome sliding when taking advantage of the kinetic properties of this process. As exemplified for ACF (ISWI subfamily), nucleosome binding, active translocation and also the pause phases between translocation events all depend on the ATP concentration (Blosser et al., 2009). If conformational changes of the remodeler are intimately connected to nucleotide turnover, all phases of nucleosome repositioning that have been unmasked by nucleosome-based smFRET might require such rearrangements of the remodeler itself. Furthermore, successive incremental translocation step sizes of 1 bp or 1-2 bp, respectively, have been reported for nucleosome repositioning by an ISWI subfamily remodeler and RSC when limiting timely nucleotide turnover in the presence of a competitive inhibitor and/or at low temperatures – Deindl et al. (2013) and Harada et al. (2016) thereby convincingly demonstrated that their nucleosome-based smFRET assay reads out active translocation of the remodeler.

6.2 *Sc*INO80 as processive enzyme with distinct mechanistic properties

Pre-bound INO80 repositions surface tethered nucleosomes for at least 10 bp as outlined in section 5.2.4. This reveals that INO80 is a processive enzyme given that Swi2/Snf2-type ATPases in general execute incremental sub-steps, for example single bp steps (Deindl et al., 2013; Farnung et al., 2017; Harada et al., 2016; Hopfner and Michaelis, 2007; Liu et al., 2017; Sirinakis et al., 2011; Wigley and Bowman, 2017). This notion also agrees with a recent single-molecule study on INO80 that exploited the fast exit DNA elongation off the nucleosome core observed in real time to reveal the step size of the initial processive translocation event, which is between ca. 5 bp to 20 bp (Zhou et al., 2018). Roughly half of these translocation events feature nucleosome movement beyond 10 bp (Zhou et al., 2018). My observation of processive INO80 sliding describes

a lower limit for the fraction of nucleosomes that remained bound by INO80 throughout several chemo-mechanical cycles, as potentially some nucleosomes have not been bound by INO80, or some nucleosomes potentially have been bound by an inactive remodeling complex. All nucleosomes are taken into consideration when probing the equilibrium situation after active remodeling (section 5.2.4). With this approach, roughly half of the observed nucleosomes were repositioned by at least 10 bp (or multiples thereof) when restricting remodeling to pre-bound INO80 (section 5.2.4). Consistently, INO80 is a processive enzyme (Schwarz et al., 2018; Zhou et al., 2018).

It has been outlined in section 2.5.2 that the nucleosome is engaged by INO80^{core} in a unique manner that involves all interaction platforms provided by the NCP and in particular INO80's main ATPase and its subunits Arp5 and Ies2 (Eustermann et al., 2018). Additionally the ARP- and NHP10-modules (described in sections 2.5.1 and 2.5.3) interact with the nucleosome and/or the adjacent linker DNA when INO80 is probed with *in vitro* crosslinking or *in vivo* high-resolution chromatin immunoprecipitation studies (Tosi et al., 2013; Yen et al., 2013). Therefore, a number of INO80 subunits might contribute to tether the INO80 complex to the nucleosome and to confer its processivity.

Further, I observed fast FRET efficiency fluctuations with dwell times on the order of tens to hundreds of milliseconds in the presence of INO80 and ATP (section 5.2.8). Here, specialized measurement conditions distinct from the conditions of the assays discussed above were used. The observation of real time INO80 nucleosome interactions described in section 5.2.8 provides an unprecedented experimental platform to understand how the remodeler acts on the entry side gyre DNA in real time, given the position of the donor and of the acceptor label on the DNA (Figure 12). This is of functional importance, as the INO80^{core} nucleosome structures put forward an INO80 sliding mechanism that relies on entry side gyre DNA loop formation between the INO80-ATPase (as it actively translocates on the DNA close to the DNA entry site, near SHL-6) and the Arp5 counter grip on DNA (SHL-2 to -3) (Ayala et al., 2018; Eustermann et al., 2018). More detailed investigations are needed to understand which processes directly contribute to the FRET efficiency changes of the LF construct in the presence of INO80 and ATP (section 5.2.8).

Processive nucleosome back-and-forth movement of nucleosomes that have flanking DNA on both sides by INO80 has been reported to cause periodic changes in FRET efficiency (Zhou et al., 2018). This is equivalent to nucleosome off-centering, as nucleosomes are labeled on the histone (donor) and on the DNA (acceptor) moiety (Zhou et al., 2018). The directionality is reversed on the order of tens of seconds at saturating

ATP concentrations (Zhou et al., 2018). Bidirectional movement of similarly labeled nucleosomes by ACF and Chd1 has been shown to change direction on the time scale of seconds and is slowed down when limiting the ATP turnover (Blosser et al., 2009; Qiu et al., 2017). The alternating phases of FRET efficiency increase and decrease observed for the remodelers ACF and Chd1 showed either an ATP-dependent characteristic oscillation time or at least one ATP-dependent rate constant, respectively (Blosser et al., 2009; Qiu et al., 2017). While alternating changes from high to low FRET efficiencies and *vice versa* have been clearly linked to an ATP-dependent process (presumably nucleosome sliding) in case of ACF and Chd1 (Blosser et al., 2009; Qiu et al., 2017), dynamic FRET efficiency fluctuations of nucleosomes in the presence of INO80 (section 5.2.8) (Zhou et al., 2018) yet await an explicit proof that these observations relate to any nucleotide-dependent step of INO80's chemo-mechanical cycle.

It will be interesting to understand in future studies how the fast FRET efficiency changes that I observed for the entry side gyre DNA in the presence of INO80 and ATP (section 5.2.8), the fast INO80 nucleosome repositioning (Zhou et al., 2018) and the slow INO80 directionality switching (Zhou et al., 2018) are functionally integrated.

6.3 Nucleosome recognition by INO80 in the presence and absence of histone tails

The effect of histone tails on INO80 nucleosome recognition and sliding has been addressed by smFRET in the present study by probing the conformation of the entry side DNA (section 5.2.5) and revealed that particularly nucleosome recognition by INO80 is markedly affected in the absence of histone tails.

The FRET efficiency histogram of wtLF in the presence of *Sc*INO80 and ADP resembles the histogram of the wtLF nucleosome sample (section 5.2.4). From the cryo-EM structures of the nucleosome-INO80^{core} complexes that show that the flanking entry DNA and entry site DNA is lifted with respect to the NCP (Ayala et al., 2018; Eustermann et al., 2018), I expect a conformation of the LF nucleosome that features a FRET efficiency drop below 20 % upon INO80 binding. However, the interaction of the Snf2 ATPase with the nucleosome at SHL6 reported by an earlier structure does not require rearrangements of the nucleosomal DNA *per se* (Liu et al., 2017). The INO80 main ATPase could as well interact with the nucleosome when it exhibits the canonical DNA path at SHL6, for example as a step of nucleosome recognition and/or during INO80's mechano-chemical cycle. Also, the smFRET data reported in the present study were acquired in the presence

of ADP, while the structures of INO80[core] represent the INO80 main ATPase in the presence of a nucleotide analogue that induces an activated ground-state (Ayala et al., 2018) or in the absence of a nucleotide (Eustermann et al., 2018). The conditions applied for the smFRET measurements are not equivalent to those for INO80[conserved] structures (Ayala et al., 2018; Eustermann et al., 2018) and could reflect a different binding mode.

The molecular concept for the INO80 mechanism as inferred from INO80[conserved] structures bound to the nucleosome reports exclusively on the conserved parts of the INO80 complex (Ayala et al., 2018; Eustermann et al., 2018). The conformation of the nucleosomal DNA observed in the presence of INO80[conserved] may be different in the presence of *Sc*INO80 that has an additional species specific NHP10-module (discussed in section 2.5.1). The altered entry-site DNA conformation described by structural data of the nucleosome-INO80[conserved] (Ayala et al., 2018; Eustermann et al., 2018) and the unchanged entry-site DNA conformation for the smFRET data of nucleosomes in the presence of the entire *Sc*INO80 (this study) therefore suggests that the NHP10-module may have an unknown role in organizing the entry DNA on the nucleosome core. Subunits Nhp10, Ies5 (NHP10-module) and Arp8 (ARP-module) have been mapped to the periphery of the nucleosome free region of genes in a population of yeast cells (Yen et al., 2013). Subunits of the NHP10-module cross-link to the globular histone fold of H4 and H2B, suggesting that the NHP10-module directly participates in nucleosome engagement by INO80 (Tosi et al., 2013). Together, these studies show that the NHP10-module interacts with both, the flanking DNA and the NCP, and therefore potentially influences how the flanking DNA is organized with respect to the NCP.

For the chromatin remodeler Chd1 bound to wild-type nucleosomes, a distinct large-scale conformational change of the entry DNA has recently been demonstrated by cryoEM and smFRET (Farnung et al., 2017; Sundaramoorthy et al., 2017). This mode of interaction with the nucleosome has so far been demonstrated uniquely for Chd1 and is not conserved for INO80 (Ayala et al., 2018; Eustermann et al., 2018; Farnung et al., 2017; Sundaramoorthy et al., 2017). In case of Chd1 nucleosome engagement, entry DNA is released from the nucleosome by a cross-gyre interaction mediated by Chd1's ATPase domain and its DNA binding domain (Farnung et al., 2017; Sundaramoorthy et al., 2017).

The LF construct shows a heterogeneous population of conformational states with respect to the entry DNA in the absence of histone tails and in the presence of INO80 and ADP, while the FRET efficiency of wild-type LF nucleosomes remains largely unchanged in the presence of INO80 and ADP (section 5.2.5). INO80 is the only remodeler that is

known to be negatively regulated by histone tails (discussed in section 2.6.2). In particular in the absence of all histone tails, the nucleosome sliding and ATP hydrolysis rates are increased (Udugama et al., 2011). This suggests an impact of histone tails on the activity of the INO80 main ATPase *per se* (Udugama et al., 2011). The INO80[core] engages the entire NCP and its main ATPase interacts with the nucleosome close to SHL6 near the DNA entry site (Ayala et al., 2018; Brahma et al., 2017; Eustermann et al., 2018) (Figure 3). For wild-type nucleosomes bound by INO80[conserved], the N-terminal structured part of histone H3 adopts a conformation that allows for small scale DNA rearrangements and therefore favors the interaction of DNA with the INO80 main ATPase (Ayala et al., 2018). The smFRET data presented in sections 5.2.4 and 5.2.5 suggest that INO80 rectifies the known decreased stability and increased DNA breathing behavior of all tailless nucleosomes (Bintu et al., 2012; Brower-Toland et al., 2005; Ferreira et al., 2007b; Iwasaki et al., 2013) such that, in the presence of INO80 and ADP and in the absence of histone tails, a heterogeneous population of diverse nucleosome conformational states with respect to the entry DNA is observed. These states could then be poised for translocation by the Ino80 main ATPase when it is bound to nucleosomes in the absence of histone tails, in contrast to wild-type nucleosome recognition by INO80.

The clear indications inferred from acceptor dye properties that INO80 binding places proteins in the vicinity of the Rm84-acceptor label (section 5.2.6, Figure 18) confirm that nucleosome recognition by INO80 takes place for both wild-type and all-tailless nucleosomes. I observe a change of the acceptor dye micro-environment upon binding by INO80. This was expected, as the position of the LF acceptor label (Rm84) is located at one of the sites protected by any (not yet defined) extra-nucleosomal DNA binding module of the *Sc*INO80 complex (Brahma et al., 2017). This module has been shown to bind to one side of the entry-DNA helix with contacts centered at positions -83, -93, -103 and -115 (Brahma et al., 2017). The INO80 nucleosome recognition mode itself is different in the presence or absence of histone tails (this study) and this has functional implications on the initiation of the nucleosome sliding reaction as outlined above.

It is tempting to speculate that the observed heterogeneity of nucleosomal DNA conformations for the atLF (section 5.2.5) could be related to differences in the conformation of the bound INO80 complex (in the absence and presence of histone tails). For example, if some INO80 subunits such as Arp8 and Ies5 could generally bind to the nucleosome flanking DNA as inferred from *in vivo* mapping data (Yen et al., 2013) and at the same time stably interact with histone tails as derived from crosslinking data (Tosi et al., 2013), this constrains the conformation of the nucleosome flanking DNA. In the

absence of histone tails, the entry DNA could then explore more conformational states as observed by smFRET (section 5.2.5).

The altered nucleosome recognition by *Sc*INO80 in the absence of histone tails might reflect a modified energy landscape of nucleosome sliding initiation in the absence of histone tails (Figure 22) and is therefore a structural perspective for the reported kinetic differences of INO80 nucleosome sliding in the presence or absence of histone tails (Udugama et al., 2011). Biochemical *ensemble* experiments suggest that nucleosome sliding by INO80 likely implies DNA twist accumulation and is therefore functionally distinct from the continued remodeling reaction (Brahma et al., 2017). The transition from nucleosome recognition by INO80 to productive nucleosome sliding might therefore require most energy input during the sliding reaction. Along this line, the regulatory impact by the plasticity of the nucleosome itself on nucleosome remodeling by INO80 might be greatest when nucleosome sliding is initiated. This explains how the nucleosome recognition mode by INO80 in the presence or absence of histone tails as defined by smFRET (sections 5.2.4 and 5.2.5) potentially affects the energy expenditure required to induce nucleosome repositioning (Figure 22). Another enzyme that initiates its interplay with the nucleosome at the DNA entry site is the RNAP (Chang et al., 2014; Hodges et al., 2009; Kulaeva et al., 2013). Using elegant force-spectroscopy methods it was demonstrated on a single-molecule level that RNAP is a ratchet that moves around the nucleosome when the nucleosome's intrinsic thermally induced dynamics provide windows of opportunity with unhindered access to the DNA (Hodges et al., 2009; Otterstrom and van Oijen, 2009). Consequently, RNAP features significantly fewer and shorter pause phases when invading all tailless nucleosomes (Bintu et al., 2012; Újvári et al., 2008). Taken together, the plasticity of all tailless nucleosomes might confer an increased accessibility of the INO80 main ATPase to the translocation site or reduce the number of futile ATPase cycles that do not provoke DNA translocation (Schwarz et al., 2018).
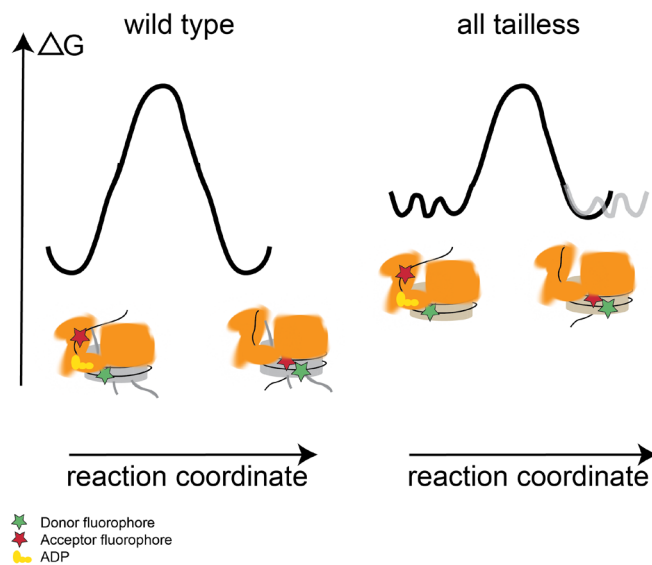
Figure 22. SmFRET reveals a homogenous INO80 bound state for wild-type nucleosomes in contrast to a heterogeneous distribution of INO80 bound states for all tailless nucleosomes. This might cause a lowered energy barrier for the initiation of nucleosome remodeling in the absence of histone tails. INO80 binds with the same affinity to wild-type and all tailless nucleosomes, but nucleosome sliding by INO80 is facilitated in the absence of histone tails (Udugama et al., 2011).

Figure 22 is adapted from Schwarz et al. (2018). The absence of histone tails is implied by the brown color of the octamer core. For clarity, some histone tails are shown for the wild-type octamer core. For exact FRET label positions, see Figure 12 and for the location of histone tails and the binding mode of INO80^{core}, see Figure 2 and Figure 3.

The presence or absence of histone tails could reflect a more general impact of nucleosome plasticity in the context of INO80 remodeling that may have physiological relevance. The combinatorial nature of histone modifications (Jenuwein and Allis, 2001; Strahl and Allis, 2000) and the incorporation of histone variants (Talbert and Henikoff, 2017) provide a large spectrum of potential remodeler substrates with differential nucleosome plasticity. An immense number of various histone modifications and mutations that provide a regulatory spectrum for chromatin organization were recently probed for effects on ISWI nucleosome sliding (Dann et al., 2017). This seminal effort used a large barcoded nucleosome library and seven different human ISWI subfamily remodelers (Dann et al., 2017). Some modified nucleosomes elicited variable responses by these remodelers, but in most cases remodeling by the different ISWI remodelers was similarly impacted by a given nucleosome modification (Dann et al., 2017). This implies that the physicochemical properties of nucleosomes as such tune the ISWI remodeler (Dann et al., 2017). The idea that the altered flexibility of modified nucleosomes might generally contribute to the regulation of INO80's activity *in vivo* is an appealing explanation of how INO80 can accomplish pivotal roles that impact DNA repair, DNA replication and transcription.

6.4 Outlook

The INO80-nucleosome binding investigations in the present study motivate further experiments to validate the interpretation that the initiation of nucleosome remodeling by the INO80 ATPase could be tuned by its nucleosome substrate. Much like all tailless nucleosomes, H3K56 acetylated nucleosomes feature an altered DNA coordination at the entry/exit sites and increased DNA breathing as unraveled by single-molecule studies (Buning and van Noort, 2010; Kim et al., 2015; Neumann et al., 2009; Simon et al., 2011). It is also another substrate that enhances INO80 activity, referring to the H3K56Q acetylation mimic nucleosome and to the H2A.Z histone variant exchange editing activity of INO80 (Watanabe et al., 2013). It will be interesting to see if the nucleosome recognition step by INO80 for nucleosomes harboring H3K56 acetylated histones features a similarly heterogeneous population of entry DNA conformations as observed for the all tailless nucleosomes.

Further, it needs to be clarified how the INO80 complex elicits the herein reported differential nucleosome recognition either in the presence and absence of histone tails, for example with respect to INO80 submodules that contribute to both scenarios. Subunits that have been crosslinked to histone tails are the INO80 main ATPase, Rvb1, Rvb2, Ies2, Arp5, Ies6 (components of the INO80^{core}), Arp4, Arp8, Taf14, Ies4 (components of the ARP-module) and Ies1, Ies3, Ies5 (components of the NHP10-module) (Tosi et al., 2013). The globular histone fold and histone tails interact with a number of INO80 subunits as identified by crosslinking (Tosi et al., 2013) and it remains elusive which interactions are explicitly important for nucleosome recognition. Previously characterized INO80 submodule deletion mutants (Tosi et al., 2013) are ideally suited to address this question.

Such investigations are for example important to understand if the NHP10-module contributes to distinct nucleosome recognition by INO80 or to give a molecular insight into the previously reported inhibitory role of the NHP10-module on INO80 nucleosome sliding (Zhou et al., 2018). The Nhp10 subunit itself is a <u>h</u>igh <u>m</u>obility <u>g</u>roup <u>B</u> (HMGB) family protein that has been shown to bind preferentially to distorted DNA *in vitro* (Ray and Grove, 2012). This property could influence the nucleosome recognition mode of the INO80 complex. Distantly related vertebrate HMGN proteins have indeed been reported to staple the nucleosome flanking DNA to the nucleosome core and to hinder chromatin remodelers (Kato et al., 2011; McGinty and Tan, 2015; Rattner et al., 2009). Given that the wtLF nucleosome construct in the presence of the entire *Sc*INO80 (this study) features a FRET efficiency that cannot be explained by the structures of the nucleosome bound by

INO80[conserved] (Ayala et al., 2018; Eustermann et al., 2018), it may be an exclusive probe to study nucleosome recognition and entry DNA conformation upon nucleosome engagement by INO80 in the presence or absence of the yeast species specific NHP10-module.

Continued investigations that use the platform for smFRET based real-time assays that probe INO80 as established in the present study are of great interest. The dissection of ATP dependent sub-steps of INO80's chemo-mechanical cycle is so far elusive and future studies need to address this in detail (section 5.2.8). Along this line, the technical feasibility of another recent similar single-molecule study on INO80 was limited to ATP concentrations in the micro-molar range and, within these limits, found only the waiting time that precedes INO80 translocation to depend on ATP, as well as a weak ATP-dependence of the initial nucleosomes repositioning phase as a whole (Zhou et al., 2018). Competitive inhibitors for ATP binding, for example ADP, are a promising approach to infer different nucleotide dependent sub-steps in future studies (section 5.2.8).

The nucleosome constructs characterized in the present study probe the conformation of the entry side DNA gyre that is engaged by the INO80 main ATPase and the Arp5 subunit, or instead the exiting DNA that is not known to directly interact with INO80 (Ayala et al., 2018; Eustermann et al., 2018). Therefore, these complementary nucleosome constructs are ideally suited to probe the ongoing sliding reaction and to solve a paradox that recently came up in the context of INO80's nucleosome sliding mechanism. Transient DNA loop formation suggested by nucleosome-INO80[core] structures is proposed near the H2A/B dimer contact sites on the **entry** side DNA gyre (Ayala et al., 2018; Eustermann et al., 2018). INO80 main ATPase translocation at SHL6 close to the DNA entry site (in the context of *Sc*INO80) indeed considerably weakens the histone-DNA contacts of the proximal H2A/B dimer (Brahma et al., 2017). In contrast, a regulatory intermediate nucleosome state that features excess DNA as inferred from site-specific accessibility assays, suggests DNA loop formation near the H2A/B dimer contact sites on the DNA **exit** side gyre (Zhou et al., 2018). Similarly, the timescales reported for INO80 induced FRET efficiency fluctuations of double-labeled nucleosomes greatly depend on the nucleosome construct and on the label positions. Dwell times that range from the order of tens/hundreds of milliseconds (section 5.2.8, this study) to seconds/tens of seconds (Zhou et al., 2018) have been observed. Future studies need to investigate how such real-time FRET efficiency changes explain INO80's chemo-mechanical cycle.

7. References

Christopher W. Akey and Karolin Luger (2003). Histone chaperones and nucleosome assembly. In *Current Opinion in Structural Biology* 13 (1)*: pp. 6-14.

Hanan E. Alatwi and Jessica A. Downs (2015). Removal of H2A.Z by INO80 promotes homologous recombination. In *EMBO Reports* 16 (8)*: pp. 986-994.

Istvan Albert, Travis N. Mavrich, Lynn P. Tomsho, Ji Qi, Sara J. Zanton, Stephan C. Schuster and B. Franklin Pugh (2007). Translational and rotational settings of H2A.Z nucleosomes across the *Saccharomyces cerevisiae* genome. In *Nature* 446 (7135)*: pp. 572-576.

Eric A. Alcid and Toshio Tsukiyama (2014). ATP-dependent chromatin remodeling shapes the long noncoding RNA landscape. In *Genes & Development* 28 (21)*: pp. 2348-2360.

Robin C. Allshire and Hiten D. Madhani (2018). Ten principles of heterochromatin formation and function. In *Nature Reviews Molecular Cell Biology* 19 (4)*: pp. 229-244.

Anita Almer, Hans Rudolph, Albert Hinnen and Wolfram Hörz (1986). Removal of positioned nucleosomes from the yeast PHO5 promoter upon PHO5 induction releases additional upstream activating DNA elements. In *The EMBO Journal* 5 (10)*: pp. 2689-2696.

J. D. Anderson and J. Widom (2000). Sequence and position-dependence of the equilibrium accessibility of nucleosomal DNA target sites. In *Journal of Molecular Biology* 296 (4)*: pp. 979-987.

Matthew Antonik, Suren Felekyan, Alexander Gaiduk and Claus A. Seidel (2006). Separating structural heterogeneities from stochastic variations in fluorescence resonance energy transfer distributions via photon distribution analysis. In *The Journal of Physical Chemistry B* 110 (13)*: pp. 6970-6978.

Ricardo J. Aramayo, Oliver Willhoft, Rafael Ayala, Rohan Bythell-Douglas, Dale B. Wigley and Xiaodong Zhang (2018). Cryo-EM structures of the human INO80 chromatin-remodeling complex. In *Nature Structural & Molecular Biology* 25 (1)*: pp. 37-44.

Claudia Arndt, Stefanie Koristka, Holger Bartsch and Michael Bachmann (2012). Native polyacrylamide gels. In *Protein Electrophoresis. Methods in Molecular Biology (Methods and Protocols),* vol. 869. eds: B. Kurien, and R. Scofield. Totowa, New Jersey: Humana Press

Rafael Ayala, Oliver Willhoft, Ricardo J. Aramayo, Martin Wilkinson, Elizabeth A. McCormack, Lorraine Ocloo, Dale B. Wigley and Xiaodong Zhang (2018). Structure and regulation of the human INO80-nucleosome complex. In *Nature* 556 (7701)*: pp. 391-395.

Yunhe Bao and Xuetong Shen (2011). SnapShot: Chromatin remodeling: INO80 and SWR1. In *Cell* 144 (1)*:* p. 158. 158e1. 158e2.

Blaine Bartholomew (2013). Monomeric actin required for INO80 remodeling. In *Nature Structural & Molecular Biology* 20 (4)*:* pp. 405-407.

Blaine Bartholomew (2014). Regulating the chromatin landscape: structural and mechanistic perspectives. In *Annual Review of Biochemistry* 83*:* pp. 671-696.

Martin L. Bennink, Sanford H. Leuba, Gregory H. Leno, Jordanka Zlatanova, Bart G. de Grooth and Jan Greve (2001). Unfolding individual nucleosomes by stretching single chromatin fibers with optical tweezers. In *Nature Structural Biology* 8 (7)*:* pp. 606-610.

Silvija Bilokapic, Mike Strauss and Mario Halic (2018). Histone octamer rearranges to adapt to DNA unwrapping. In *Nature Structural & Molecular Biology* 25 (1)*:* pp. 101-108.

Lacramioara Bintu, Toyotaka Ishibashi, Manchuta Dangkulwanich, Yueh-Yi Wu, Lucyna Lubkowska, Mikhail Kashlev and Carlos Bustamante (2012). Nucleosomal elements that control the topography of the barrier to transcription. In *Cell* 151 (4)*:* pp. 738-749.

Timothy R. Blosser, Janet G. Yang, Michael D. Stone, Geeta J. Narlikar and Xiaowei Zhuang (2009). Dynamics of nucleosome remodelling by individual ACF complexes. In *Nature* 462 (7276)*:* pp. 1022-1027.

Vera Böhm, Aaron R. Hieb, Andrew J. Andrews, Alexander Gansen, Andrea Rocker, Katalin Tóth, Karolin Luger and Jörg Langowski (2011). Nucleosome accessibility governed by the dimer/tetramer interface. In *Nucleic Acids Research* 39 (8)*:* pp. 3093-3102.

Clemens Bönisch, Katrin Schneider, Sebastian Punzeler, Sonja M. Wiedemann, Christina Bielmeier, Marco Bocola, H. Christian Eberl, Wolfgang Kuegel, Jürgen Neumann, Elisabeth Kremmer, Heinrich Leonhardt, Matthias Mann, Jens Michaelis, Lothar Schermelleh and Sandra B. Hake (2012). H2A.Z.2.2 is an alternatively spliced histone H2A.Z variant that causes severe nucleosome destabilization. In *Nucleic Acids Research* 40 (13)*:* pp. 5951-5964.

Gregory D. Bowman (2010). Mechanisms of ATP-dependent nucleosome sliding. In *Current Opinion in Structural Biology* 20 (1)*:* pp. 73-81.

Sandipan Brahma, Maheshi I. Udugama, Jongseong Kim, Arjan Hada, Saurabh K. Bhardwaj, Solomon G. Hailu, Tae-Hee Lee and Blaine Bartholomew (2017). INO80 exchanges H2A.Z for H2A by translocating on DNA proximal to histone dimers. In *Nature Communications* 8. Article number: 15616.

Brent Brower-Toland, David A. Wacker, Robert M. Fulbright, John T. Lis, W. Lee Kraus and Michelle D. Wang (2005). Specific contributions of histone tails and their acetylation to the mechanical stability of nucleosomes. In *Journal of Molecular Biology* 346 (1)*:* pp. 135-146.

Ruth Buning and John van Noort (2010). Single-pair FRET experiments on nucleosome conformational dynamics. In *Biochimie* 92 (12)*: pp. 1729-1740.

Tingting Cao, Lingfei Sun, Yuxiang Jiang, Shanjin Huang, Jiawei Wang and Zhucheng Chen (2016). Crystal structure of a nuclear actin ternary complex. In *Proceedings of the National Academy of Sciences of the United States of America* 113 (32)*: pp. 8985-8990.

Han-Wen Chang, Olga I. Kulaeva, Alexey K. Shaytan, Mikhail Kibanov, Konstantin Kuznedelov, Konstantin V. Severinov, Mikhail P. Kirpichnikov, David J. Clark and Vasily M. Studitsky (2014). Analysis of the mechanism of nucleosome survival during transcription. In *Nucleic Acids Research* 42 (3)*: pp. 1619-1627.

Lu Chen, Yong Cai, Jingji Jin, Laurence Florens, Selene K. Swanson, Michael P. Washburn, Joan W. Conaway and Ronald C. Conaway (2011). Subunit organization of the human INO80 chromatin remodeling complex: an evolutionarily conserved core complex catalyzes ATP-dependent nucleosome remodeling. In *The Journal of Biological Chemistry* 286 (13)*: pp. 11283-11289.

Lu Chen, Ronald C. Conaway and Joan W. Conaway (2013). Multiple modes of regulation of the human Ino80 SNF2 ATPase by subunits of the INO80 chromatin-remodeling complex. In *Proceedings of the National Academy of Sciences of the United States of America* 110 (51)*: pp. 20497-20502.

Eugene Y. Chua, Dileep Vasudevan, Gabriela E. Davey, Bin Wu and Curt A. Davey (2012). The mechanics behind DNA sequence-dependent properties of the nucleosome. In *Nucleic Acids Research* 40 (13)*: pp. 6338-6352.

Cedric R. Clapier and Bradley R. Cairns (2009). The biology of chromatin remodeling complexes. In *Annual Review of Biochemistry* 78*: pp. 273-304.

Cedric R. Clapier and Bradley R. Cairns (2012). Regulation of ISWI involves inhibitory modules antagonized by nucleosomal epitopes. In *Nature* 492 (7428)*: pp. 280-284.

Cedric R. Clapier, Srinivas Chakravarthy, Carlo Petosa, Carlos Fernández-Tornero, Karolin Luger and Christoph W. Müller (2008). Structure of the Drosophila nucleosome core particle highlights evolutionary constraints on the H2A-H2B histone dimer. In *Proteins* 71 (1)*: pp. 1-7.

Cedric R. Clapier, Janet Iwasa, Bradley R. Cairns and Craig L. Peterson (2017). Mechanisms of action and regulation of ATP-dependent chromatin-remodelling complexes. In *Nature Reviews Molecular Cell Biology* 18 (7)*: pp. 407-422.

Cedric R. Clapier, Margaret M. Kasten, Timothy J. Parnell, Ramya Viswanathan, Heather Szerlong, George Sirinakis, Yongli Zhang and Bradley R. Cairns (2016). Regulation of DNA translocation efficiency within the chromatin remodeler RSC/Sth1 potentiates nucleosome sliding and ejection. In *Molecular Cell* 62 (3)*: pp. 453-461.

Matthew Cobb (2017). 60 years ago, Francis Crick changed the logic of biology. In *PLoS Biology* 15 (9)*. e2003243, doi: 10.1371/journal.pbio.2003243.

Ronald C. Conaway and Joan W. Conaway (2009). The INO80 chromatin remodeling complex in transcription, replication and repair. In *Trends in Biochemical Sciences* 34 (2)*: pp. 71-77.*

Thorben Cordes, Jan Vogelsang and Philip Tinnefeld (2009). On the mechanism of Trolox as antiblinking and antibleaching reagent. In *Journal of the American Chemical Society* 131 (14)*: pp. 5018-5019.*

F. H. C. Crick (1958). On protein synthesis. In *The Symposia of the Society for Experimental Biology* 12*: pp. 138-163.*

Francis Crick (1970). Central dogma of molecular biology. In *Nature* 227 (5258)*: pp. 561-563.*

Remus T. Dame (2005). The role of nucleoid-associated proteins in the organization and compaction of bacterial chromatin. In *Molecular Microbiology* 56 (4)*: pp. 858-870.*

Geoffrey P. Dann, Glen P. Liszczak, John D. Bagert, Manuel M. Müller, Uyen T. T. Nguyen, Felix Wojcik, Zachary Z. Brown, Jeffrey Bos, Tatyana Panchenko, Rasmus Pihl, Samuel B. Pollock, Katharine L. Diehl, C. David Allis and Tom W. Muir (2017). ISWI chromatin remodellers sense nucleosome modifications to determine substrate preference. In *Nature* 548 (7669)*: pp. 607-611.*

Curt A. Davey, David F. Sargent, Karolin Luger, Armin W. Maeder and Timothy J. Richmond (2002). Solvent mediated interactions in the structure of the nucleosome core particle at 1.9 Å resolution. In *Journal of Molecular Biology* 319 (5)*: pp. 1097-1113.*

Mekonnen L. Dechassa, Swetansu K. Hota, Payel Sen, Nilanjana Chatterjee, Punit Prasad and Blaine Bartholomew (2012). Disparity in the DNA translocase domains of SWI/SNF and ISW2. In *Nucleic Acids Research* 40 (10)*: pp. 4412-4421.*

Sebastian Deindl, William L. Hwang, Swetansu K. Hota, Timothy R. Blosser, Punit Prasad, Blaine Bartholomew and Xiaowei Zhuang (2013). ISWI remodelers slide nucleosomes with coordinated multi-base-pair entry steps and single-base-pair exit steps. In *Cell* 152 (3)*: pp. 442-452.*

Vincenzo Di Cerbo, Fabio Mohn, Daniel P. Ryan, Emilie Montellier, Salim Kacem, Philipp Tropberger, Eleni Kallis, Monika Holzner, Leslie Hoerner, Angelika Feldmann, Florian M. Richter, Andrew J. Bannister, Gerhard Mittler, Jens Michaelis, Saadi Khochbin, Robert Feil, Dirk Schuebeler, Tom Owen-Hughes, Sylvain Daujat and Robert Schneider (2014). Acetylation of histone H3 at lysine 64 regulates nucleosome dynamics and facilitates transcription. In *eLife* 3. e01632, doi: 10.7554/eLife.01632.

Mykola Dimura, Thomas O. Peulen, Christian A. Hanke, Aiswaria Prakash, Holger Gohlke and Claus A. Seidel (2016). Quantitative FRET studies and integrative modeling unravel the structure and dynamics of biomolecular systems. In *Current Opinion in Structural Biology* 40*: pp. 163-185.*

James M. Dixon, Masahiko Taniguchi and Jonathan S. Lindsey (2005). PhotochemCAD 2: A Refined Program with Accompanying Spectral Databases for Photochemical Calculations. In *Photochemistry and Photobiology* 81 (1)*: pp. 212-213.*

Thilo Dörfler, Tobias Eilert, Carlheinz Röcker, Julia Nagy and Jens Michaelis (2017). Structural Information from Single-molecule FRET Experiments Using the Fast Nano-positioning System. In *Journal of Visualized Experiments* 120. e54782, doi: 10.3791/54782.

John W. Dubendorff and F. William Studier (1991). Controlling basal expression in an inducible T7 expression system by blocking the target T7 promoter with lac repressor. In *Journal of Molecular Biology* 219 (1)*: pp. 45-59.

Harald Dürr, Christian Körner, Marisa Müller, Volker Hickmann and Karl-Peter Hopfner (2005). X-ray structures of the Sulfolobus solfataricus SWI2/SNF2 ATPase core and its complex with DNA. In *Cell* 121 (3)*: pp. 363-373.

Pamela N. Dyer, Raji S. Edayathumangalam, Cindy L. White, Yunhe Bao, Srinivas Chakravarthy, Uma M. Muthurajan and Karolin Luger (2003). Reconstitution of nucleosome core particles from recombinant histones and DNA. In *Methods in Enzymology* 375 pp. 23-44.

Ronald Ebbert, Alexander Birkmann and Hans-Joachim Schüller (1999). The product of the SNF2/SWI2 paralogue INO80 of *Saccharomyces cerevisiae* required for efficient expression of various yeast structural genes is part of a high-molecular-weight protein complex. In *Molecular Microbiology* 32 (4)*: pp. 741-751.

Tobias Eilert, Maximilian Beckers, Florian Drechsler and Jens Michaelis (2017). Fast-NPS-A Markov Chain Monte Carlo-based analysis tool to obtain structural information from single-molecule FRET measurements. In *Computer Physics Communications* 219 pp. 377-389.

Umut Eser, Devon Chandler-Brown, Ferhat Ay, Aaron F. Straight, Zhijun Duan, William S. Noble and Jan M. Skotheim (2017). Form and function of topologically associating genomic domains in budding yeast. In *Proceedings of the National Academy of Sciences of the United States of America* 114 (15). e3061-e3070, doi: 10.1073/pnas.1612256114.

Sebastian Eustermann, Kevin Schall, Dirk Kostrewa, Kristina Lakomek, Mike Strauss, Manuela Moldt and Karl-Peter Hopfner (2018). Structural basis for ATP-dependent chromatin remodelling by the INO80 complex. In *Nature* 556 (7701)*: pp. 386-390.

Lucas Farnung, Seychelle M. Vos, Christoph Wigge and Patrick Cramer (2017). Nucleosome-Chd1 structure and implications for chromatin remodelling. In *Nature* 550 (7677)*: pp. 539-542.

Helder Ferreira, Andrew Flaus and Tom Owen-Hughes (2007a). Histone modifications influence the action of Snf2 family remodelling enzymes by different mechanisms. In *Journal of Molecular Biology* 374 (3)*: pp. 563-579.

Helder Ferreira, Joanna Somers, Ryan Webster, Andrew Flaus and Tom Owen-Hughes (2007b). Histone tails and the H3 αN helix regulate nucleosome mobility and stability. In *Molecular and Cellular Biology* 27 (11)*: pp. 4037-4048.

Beat Fierz (2016). Dynamic chromatin regulation from a single molecule perspective. In *ACS Chemical Biology* 11 (3)*: pp. 609-620.

J. T. Finch and A. Klug (1976). Solenoidal model for superstructure in chromatin. In *Proceedings of the National Academy of Sciences of the United States of America* 73 (6)*:* pp. 1897-1901.

Andrew Flaus, David M. Martin, Geoffrey J. Barton and Tom Owen-Hughes (2006). Identification of multiple distinct Snf2 subfamilies with conserved structural motifs. In *Nucleic Acids Research* 34 (10)*:* pp. 2887-2905.

Th. Förster (1948). Zwischenmolekulare Energiewanderung und Fluoreszenz. In *Annalen der Physik* 6 (2)*:* pp. 55-75.

Timothy D. Frouws, Philip D. Barth and Timothy J. Richmond (2018). Site-Specific Disulfide Crosslinked Nucleosomes with Enhanced Stability. In *Journal of Molecular Biology* 430 (1)*:* pp. 45-57.

Eden Fussner, Reagan W. Ching and David P. Bazett-Jones (2011). Living without 30 nm chromatin fibers. In *Trends in Biochemical Sciences* 36 (1)*:* pp. 1-6*.*

Nathan Gamarra, Stephanie L. Johnson, Michael J. Trnka, Alma L. Burlingame and Geeta J. Narlikar (2018). The nucleosomal acidic patch relieves auto-inhibition by the ISWI remodeler SNF2h. In *eLife* 7. e35322*,* doi: 10.7554/eLife.35322.

Alex Gansen, Katalin Tóth, Nathalie Schwarz and Jörg Langowski (2009a). Structural variability of nucleosomes detected by single-pair Förster resonance energy transfer: histone acetylation, sequence variation, and salt effects. In *The Journal of Physical Chemistry B* 113 (9)*:* pp. 2604-2613.

Alexander Gansen, Alessandro Valeri, Florian Hauger, Suren Felekyan, Stanislav Kalinin, Katalin Tóth, Jörg Langowski and Claus A. Seidel (2009b). Nucleosome disassembly intermediates characterized by single-molecule FRET. In *Proceedings of the National Academy of Sciences of the United States of America* 106 (36)*:* pp. 15308-15313.

Elisabeth Gasteiger, Christine Hoogland, Alexandre Gattiker, Severine Duvaud, Marc R Wilkins, Ron D Appel and Amos Bairoch (2005). Protein Identification and Analysis Tools on the ExPASy Server. In *The Proteomics Protocols Handbook.* ed. J.M. Walker. Humana Press

Alexandra M. Gehring, Julie E. Walker and Thomas J. Santangelo (2016). Transcription Regulation in Archaea. In *Journal of Bacteriology* 198 (14)*:* pp. 1906-1917*.*

Christian B. Gerhold, Duane D. Winkler, Kristina Lakomek, Florian U. Seifert, Sebastian Fenn, Brigitte Kessler, Gregor Witte, Karolin Luger and Karl-Peter Hopfner (2012). Structure of Actin-related protein 8 and its contribution to nucleosome binding. In *Nucleic Acids Research* 40 (21)*:* pp. 11036-11046*.*

Triantaffyllos Gkikopoulos, Pieta Schofield, Vijender Singh, Marina Pinskaya, Jane Mellor, Michaela Smolle, Jerry L. Workman, Geoffrey J. Barton and Tom Owen-Hughes (2011). A role for Snf2-related nucleosome-spacing enzymes in genome-wide nucleosome organization. In *Science* 333 (6050)*:* pp. 1758-1760.

Adriana Gonzalez-Sandoval and Susan M. Gasser (2016). On TADs and LADs: Spatial Control Over Gene Expression. In *Trends in Genetics* 32 (8)*: pp. 485-495.

Michael Richard Green and Joseph Sambrook (2012). Molecular Cloning: A Laboratory Manual, 4th edition. Cold Spring Harbor, New York: Cold Spring Harbor Laboratory Press

Meigang Gu and Charles M. Rice (2010). Three conformational snapshots of the hepatitis C virus NS3 helicase reveal a ratchet translocation mechanism. In *Proceedings of the National Academy of Sciences of the United States of America* 107 (2)*: pp. 521-528.

Taekjip Ha and Philip Tinnefeld (2012). Photophysics of fluorescent probes for single-molecule biophysics and super-resolution imaging. In *Annual Review of Physical Chemistry* 63*: pp. 595-617.

Caroline Haas (2013). Structural Analysis of Chromatin Remodeler by Electron Microscopy. Dissertation. Ludwig-Maximilians-Universität München, Fakultät für Chemie und Pharmazie, url: http://nbn-resolving.de/urn:nbn:de:bvb:19-164056.

Michael A. Hall, Alla Shundrovsky, Lu Bai, Robert M. Fulbright, John T. Lis and Michelle D. Wang (2009). High-resolution dynamic mapping of histone-DNA interactions in a nucleosome. In *Nature Structural & Molecular Biology* 16 (2)*: pp. 124-129.

Colin M. Hammond, Caroline B. Strømme, Hongda Huang, Dinshaw J. Patel and Anja Groth (2017). Histone chaperone networks shaping chromatin function. In *Nature Reviews Molecular Cell Biology* 18*: pp. 141-158.

Min Han and Michael Grunstein (1988). Nucleosome loss activates yeast downstream promoters in vivo. In *Cell* 55 (6)*: pp. 1137-1145.

Douglas Hanahan, Joel Jessee and Fredric R. Bloom (1991). Plasmid transformation of *Escherichia coli* and other bacteria. In *Methods in Enzymology* 204*: pp. 63-113.

Bryan T. Harada, William L. Hwang, Sebastian Deindl, Nilanjana Chatterjee, Blaine Bartholomew and Xiaowei Zhuang (2016). Stepwise nucleosome translocation by RSC remodeling complexes. In *eLife* 5. e10051, doi: 10.7554/eLife.10051.

Glenn Hauk, Jeffrey N. McKnight, Ilana M. Nodelman and Gregory D. Bowman (2010). The chromodomains of the Chd1 chromatin remodeler regulate DNA access to the ATPase motor. In *Molecular Cell* 39 (5)*: pp. 711-723.

Gregor Johann Heiss (2011). Single-Molecule Microscopy Study of Nano-Systems: From synthetic photo-switchable nano-devices to the dynamics of naturally occurring transcription factors. Dissertation. Ludwig-Maximilians-Universität München, Fakultät für Chemie und Pharmazie, url: http://nbn-resolving.de/urn:nbn:de:bvb:19-138640.

Emil Heitz (1928). Das Heterochromatin der Moose. In *Jahrbücher für wissenschaftliche Botanik* 69*: pp. 762-818.

Björn Hellenkamp, Sonja Schmid, Olga Doroshenko, Oleg Opanasyuk, Ralf Kühnemuth, Soheila Rezaei Adariani, Anders Barth, Victoria Birkedal, Mark E. Bowen, Hongtao Chen, Thorben Cordes, Tobias Eilert, Carel Fijen, Markus Götz, Giorgos Gouridis, Enrico Gratton, Taekjip Ha, Christian A. Hanke, Andreas Hartmann, Jelle Hendrix, Lasse L. Hildebrandt, Johannes Hohlbein, Christian G. Hübner, Eleni Kallis, Achillefs N. Kapanidis, Jae-Yeol Kim, Georg Krainer, Don C. Lamb, Nam Ki Lee, Edward A. Lemke, Brié Levesque, Marcia Levitus, James J. McCann, Nikolaus Naredi-Rainer, Daniel Nettels, Thuy Ngo, Ruoyi Qiu, Carlheinz Röcker, Hugo Sanabria, Michael Schlierf, Benjamin Schuler, Henning Seidel, Lisa Streit, Philip Tinnefeld, Swati Tyagi, Niels Vandenberk, Keith R. Weninger, Bettina Wünsch, Inna S. Yanez-Orozco, Jens Michaelis, Claus A.M. Seidel, Timothy D. Craggs and Thorsten Hugel (arXiv:1710.03807 [q-bio.QM]). Precision and accuracy of single-molecule FRET measurements - a worldwide benchmark study. In *arXiv:* 1710.03807 [q-bio.QM] (2017).[1]

Steven Henikoff and M. Mitchell Smith (2015). Histone variants and epigenetics. In *Cold Spring Harbor Perspectives in Biology* 7. a019364, doi: 10.1101/cshperspect.a019364.

Lasse L. Hildebrandt, Søren Preus and Victoria Birkedal (2015). Quantitative single molecule FRET efficiencies using TIRF microscopy. In *Faraday Discussions* 184*:* pp. 131-142.

Courtney Hodges, Lacramioara Bintu, Lucyna Lubkowska, Mikhail Kashlev and Carlos Bustamante (2009). Nucleosomal fluctuations govern the transcription dynamics of RNA polymerase II. In *Science* 325 (5940)*:* pp. 626-628.

Helen Hoffmeister, Andreas Fuchs, Fabian Erdel, Sophia Pinz, Regina Grobner-Ferreira, Astrid Bruckmann, Rainer Deutzmann, Uwe Schwartz, Rodrigo Maldonado, Claudia Huber, Anne-Sarah Dendorfer, Karsten Rippe and Gernot Längst (2017). CHD3 and CHD4 form distinct NuRD complexes with different yet overlapping functionality. In *Nucleic Acids Research* 45 (18)*:* pp. 10534-10554.

Cassandra J. Hogan, Sofia Aligianni, Mickaël Durand-Dubief, Jenna Persson, William R. Will, Judith Webster, Linda Wheeler, Christopher K. Mathews, Sarah Elderkin, David Oxley, Karl Ekwall and Patrick D. Varga-Weisz (2010). Fission yeast Iec1-Ino80-mediated nucleosome eviction regulates nucleotide and phosphate metabolism. In *Molecular and Cellular Biology* 30 (3)*:* pp. 657-674.

---

[1] now published in: Björn Hellenkamp, Sonja Schmid, Olga Doroshenko, Oleg Opanasyuk, Ralf Kühnemuth, Soheila Rezaei Adariani, Benjamin Ambrose, Mikayel Aznauryan, Anders Barth, Victoria Birkedal, Mark E. Bowen, Hongtao Chen, Thorben Cordes, Tobias Eilert, Carel Fijen, Christian Gebhardt, Markus Götz, Giorgos Gouridis, Enrico Gratton, Taekjip Ha, Pengyu Hao, Christian A. Hanke, Andreas Hartmann, Jelle Hendrix, Lasse L. Hildebrandt, Verena Hirschfeld, Johannes Hohlbein, Boyang Hua, Christian G. Hübner, Eleni Kallis, Achillefs N. Kapanidis, Jae-Yeol Kim, Georg Krainer, Don C. Lamb, Nam Ki Lee, Edward A. Lemke, Brié Levesque, Marcia Levitus, James J. McCann, Nikolaus Naredi-Rainer, Daniel Nettels, Thuy Ngo, Ruoyi Qiu, Nicole C. Robb, Carlheinz Röcker, Hugo Sanabria, Michael Schlierf, Tim Schröder, Benjamin Schuler, Henning Seidel, Lisa Streit, Johann Thurn, Philip Tinnefeld, Swati Tyagi, Niels Vandenberk, Andrés Manuel Vera, Keith R. Weninger, Bettina Wünsch, Inna S. Yanez-Orozco, Jens Michaelis, Claus A. M. Seidel, Timothy D. Craggs and Thorsten Hugel (2018). Precision and accuracy of single-molecule FRET measurements – a multi-laboratory benchmark study. In *Nature Methods* 15 (9): pp. 669-676.

Johannes Hohlbein, Timothy D. Craggs and Thorben Cordes (2014). Alternating-laser excitation: single-molecule FRET and beyond. In *Chemical Society Reviews* 43 (4)*:* pp. 1156-1171.

Jingjun Hong, Hanqiao Feng, Feng Wang, Anand Ranjan, Jianhong Chen, Jiansheng Jiang, Rodolfo Ghirlando, T. Sam Xiao, Carl Wu and Yawen Bai (2014). The catalytic subunit of the SWR1 remodeler is a histone chaperone for the H2A.Z-H2B dimer. In *Molecular Cell* 53 (3)*:* pp. 498-505.

Karl-Peter Hopfner, Christian-Benedikt Gerhold, Kristina Lakomek and Petra Wollmann (2012). Swi2/Snf2 remodelers: hybrid views on hybrid molecular machines. In *Current Opinion in Structural Biology* 22 (2)*:* pp. 225-233.

Karl-Peter Hopfner and Jens Michaelis (2007). Mechanisms of nucleic acid translocases: lessons from structural biology and single-molecule biophysics. In *Current Opinion in Structural Biology* 17 (1)*:* pp. 87-95.

Amanda L. Hughes and Oliver J. Rando (2014). Mechanisms underlying nucleosome positioning in vivo. In *Annual Review of Biophysics* 43*:* pp. 41-63.

Van A. Huynh, Philip J. Robinson and Daniela Rhodes (2005). A method for the *in vitro* reconstitution of a defined "30 nm" chromatin fibre containing stoichiometric amounts of the linker histone. In *Journal of Molecular Biology* 345 (5)*:* pp. 957-968.

Helen Hwang, Hajin Kim and Sua Myong (2011). Protein induced fluorescence enhancement as a single molecule assay with short distance sensitivity. In *Proceedings of the National Academy of Sciences of the United States of America* 108 (18)*:* pp. 7414-7418.

Helen Hwang and Sua Myong (2014). Protein induced fluorescence enhancement (PIFE) for probing protein-nucleic acid interactions. In *Chemical Society Reviews* 43 (4)*:* pp. 1221-1229.

William L. Hwang, Sebastian Deindl, Bryan T. Harada and Xiaowei Zhuang (2014). Histone H4 tail mediates allosteric regulation of nucleosome remodelling by linker DNA. In *Nature* 512 (7513)*:* pp. 213-217.

Doug Irvine, Craig Tuerk and Larry Gold (1991). SELEXION. Systematic evolution of ligands by exponential enrichment with integrated optimization by non-linear analysis. In *Journal of Molecular Biology* 222 (3)*:* pp. 739-761.

Wakana Iwasaki, Yuta Miya, Naoki Horikoshi, Akihisa Osakabe, Hiroyuki Taguchi, Hiroaki Tachiwana, Takehiko Shibata, Wataru Kagawa and Hitoshi Kurumizaka (2013). Contribution of histone N-terminal tails to the structure and stability of nucleosomes. In *FEBS Open Bio* 3*:* pp. 363-369.

An Jansen and Kevin J. Verstrepen (2011). Nucleosome positioning in *Saccharomyces cerevisiae*. In *Microbiology and Molecular Biology Reviews* 75 (2)*:* pp. 301-320.

Thomas Jenuwein and C. David Allis (2001). Translating the histone code. In *Science* 293 (5532)*:* pp. 1074-1080.

Cizhong Jiang and B. Franklin Pugh (2009a). A compiled and systematic reference map of nucleosome positions across the *Saccharomyces cerevisiae* genome. In *Genome Biology* 10. r109, doi: 10.1186/gb-2009-10-10-r109.

Cizhong Jiang and B. Franklin Pugh (2009b). Nucleosome positioning and gene regulation: advances through genomics. In *Nature Reviews Genetics* 10 (3)*: pp. 161-172.*

Jingji Jin, Yong Cai, Tingting Yao, Aaron J. Gottschalk, Laurence Florens, Selene K. Swanson, José L. Gutiérrez, Michael K. Coleman, Jerry L. Workman, Arcady Mushegian, Michael P. Washburn, Ronald C. Conaway and Joan W. Conaway (2005). A mammalian chromatin remodeling complex with similarities to the yeast INO80 complex. In *The Journal of Biological Chemistry* 280 (50)*: pp. 41207-41212.*

Zophonias O. Jónsson, Sudhakar Jha, James A. Wohlschlegel and Anindya Dutta (2004). Rvb1p/Rvb2p recruit Arp5p and assemble a functional Ino80 chromatin remodeling complex. In *Molecular Cell* 16 (3)*: pp. 465-477.*

Stanislav Kalinin, Thomas Peulen, Simon Sindbert, Paul J. Rothwell, Sylvia Berger, Tobias Restle, Roger S. Goody, Holger Gohlke and Claus A. Seidel (2012). A toolkit and benchmark study for FRET-restrained high-precision structural modeling. In *Nature Methods* 9 (12)*: pp. 1218-1225.*

Prabodh Kapoor, Mingming Chen, Duane D. Winkler, Karolin Luger and Xuetong Shen (2013). Evidence for monomeric actin function in INO80 chromatin remodeling. In *Nature Structural & Molecular Biology* 20 (4)*: pp. 426-432.*

Stefan R. Kassabov, Bei Zhang, Jim Persinger and Blaine Bartholomew (2003). SWI/SNF unwraps, slides, and rewraps the nucleosome. In *Molecular Cell* 11 (2)*: pp. 391-403.*

Daiki Kato, Akihisa Osakabe, Yasuhiro Arimura, Yuka Mizukami, Naoki Horikoshi, Kazumi Saikusa, Satoko Akashi, Yoshifumi Nishimura, Sam-Yong Park, Jumpei Nogami, Kazumitsu Maehara, Yasuyuki Ohkawa, Atsushi Matsumoto, Hidetoshi Kono, Rintaro Inoue, Masaaki Sugiyama and Hitoshi Kurumizaka (2017). Crystal structure of the overlapping dinucleosome composed of hexasome and octasome. In *Science* 356 (6334)*: pp. 205-208.*

Hidenori Kato, Hugo van Ingen, Bing-Rui Zhou, Hanqiao Feng, Michael Bustin, Lewis E. Kay and Yawen Bai (2011). Architecture of the high mobility group nucleosomal protein 2-nucleosome complex as revealed by methyl-based NMR. In *Proceedings of the National Academy of Sciences of the United States of America* 108 (30)*: pp. 12283-12288.*

Sinan Kilic, Suren Felekyan, Olga Doroshenko, Iuliia Boichenko, Mykola Dimura, Hayk Vardanyan, Louise C. Bryan, Gaurav Arya, Claus A. M. Seidel and Beat Fierz (2018). Single-molecule FRET reveals multiscale chromatin dynamics modulated by HP1α. In *Nature Communications* 9. Article number: 235.

Jessica L. Killian, Ming Li, Maxim Y. Sheinin and Michelle D. Wang (2012). Recent advances in single molecule studies of nucleosomes. In *Current Opinion in Structural Biology* 22 (1)*: pp. 80-87.*

Jongseong Kim, Jaehyoun Lee and Tae-Hee Lee (2015). Lysine Acetylation Facilitates Spontaneous DNA Dynamics in the Nucleosome. In *The Journal of Physical Chemistry B* 119 (48)*: pp. 15001-15005.

Henrike Klinker, Caroline Haas, Nadine Harrer, Peter B. Becker and Felix Mueller-Planitz (2014). Rapid purification of recombinant histones. In *PLoS One* 9 (8)*. e104029, doi: 10.1371/journal.pone.0104029.

Eva Klopf, Heiko A. Schmidt, Sandra Clauder-Münster, Lars M. Steinmetz and Christoph Schüller (2017). INO80 represses osmostress induced gene expression by resetting promoter proximal nucleosomes. In *Nucleic Acids Research* 45 (7)*: pp. 3752-3766.

Tetyana Klymenko, Bernadett Papp, Wolfgang Fischle, Thomas Kocher, Malgorzata Schelder, Cornelia Fritsch, Brigitte Wild, Matthias Wilm and Jürg Müller (2006). A Polycomb group protein complex with sequence-specific DNA-binding and selective methyl-lysine-binding activities. In *Genes & Development* 20 (9)*: pp. 1110-1122.

W. J. Koopmans, A. Brehm, C. Logie, T. Schmidt and J. van Noort (2007). Single-pair FRET microscopy reveals mononucleosome dynamics. In *Journal of Fluorescence* 17 (6)*: pp. 785-795.

W. J. Koopmans, R. Buning, T. Schmidt and J. van Noort (2009). spFRET using alternating excitation and FCS reveals progressive DNA unwrapping in nucleosomes. In *Biophysical Journal* 97 (1)*: pp. 195-204.

Philipp Korber and Slobodan Barbaric (2014). The yeast PHO5 promoter: from single locus to systems biology of a paradigm for gene regulation through chromatin. In *Nucleic Acids Research* 42 (17)*: pp. 10888-10902.

Philipp Korber and Wolfram Hörz (2004). In vitro assembly of the characteristic chromatin organization at the yeast PHO5 promoter by a replication-independent extract system. In *The Journal of Biological Chemistry* 279 (33)*: pp. 35113-35120.

Roger D. Kornberg (1974). Chromatin structure: a repeating unit of histones and DNA. In *Science* 184 (4139)*: pp. 868-871.

Roger D. Kornberg (1999). Eukaryotic transcriptional control. In *Trends in Cell Biology* 9 (12)*: pp. M46-M49.

Roger D. Kornberg (2007). The molecular basis of eukaryotic transcription. In *Proceedings of the National Academy of Sciences of the United States of America* 104 (32)*: pp. 12955-12961.

Nils Krietenstein, Megha Wal, Shinya Watanabe, Bongsoo Park, Craig L. Peterson, B. Franklin Pugh and Philipp Korber (2016). Genomic nucleosome organization reconstituted with pure proteins. In *Cell* 167 (3)*: pp. 709-721.

Katarzyna M. Krzemien, Maximilian Beckers, Salina Quack and Jens Michaelis (2017). Atomic force microscopy of chromatin arrays reveal non-monotonic salt dependence of array compaction in solution. In *PLoS One* 12 (3)*. e0173459, doi: 10.1371/journal.pone.0173459.

Volodymyr Kudryavtsev, Martin Sikor, Stanislav Kalinin, Dejana Mokranjac, Claus A. Seidel and Don C. Lamb (2012). Combining MFD and PIE for accurate single-pair Förster resonance energy transfer measurements. In *ChemPhysChem: a European Journal of Chemical Physics and Physical Chemistry* 13 (4)*: pp. 1060-1078.*

Olga I. Kulaeva, Fu-Kai Hsieh, Han-Wen Chang, Donal S. Luse and Vasily M. Studitsky (2013). Mechanism of transcription through a nucleosome by RNA polymerase II. In *Biochimica et Biophysica Acta* 1829 (1)*: pp. 76-83.*

Claudio A. Lademann, Jörg Renkawitz, Boris Pfander and Stefan Jentsch (2017). The INO80 complex removes H2A.Z to promote presynaptic filament formation during homologous recombination. In *Cell Reports* 19 (7)*: pp. 1294-1303.*

U. K. Laemmli (1970). Cleavage of structural proteins during the assembly of the head of bacteriophage T4. In *Nature* 227 (5259)*: pp. 680-685.*

Anne Lafon, Surayya Taranum, Frederico Pietrocola, Florent Dingli, Damarys Loew, Sandipan Brahma, Blaine Bartholomew and Manolis Papamichos-Chronakis (2015). INO80 Chromatin Remodeler Facilitates Release of RNA Polymerase II from Chromatin for Ubiquitin-Mediated Proteasomal Degradation. In *Molecular Cell* 60 (5)*: pp. 784-796.*

William K. M. Lai and B. Franklin Pugh (2017). Understanding nucleosome dynamics and their links to gene expression and DNA replication. In *Nature Reviews Molecular Cell Biology* 18 (9)*: pp. 548-562.*

Gernot Längst and Peter B. Becker (2001). ISWI induces nucleosome sliding on nicked DNA. In *Molecular Cell* 8 (5)*: pp. 1085-1092.*

Chrysa M. Latrick, Martin Marek, Khalid Ouararhni, Christophe Papin, Isabelle Stoll, Maria Ignatyeva, Arnaud Obri, Eric Ennifar, Stefan Dimitrov, Christophe Romier and Ali Hamiche (2016). Molecular basis and specificity of H2A.Z-H2B recognition and deposition by the histone chaperone YL1. In *Nature Structural & Molecular Biology* 23 (4)*: pp. 309-316.*

Ju Y. Lee, Sijie Wei and Tae-Hee Lee (2011). Effects of histone acetylation by Piccolo NuA4 on the structure of a nucleosome and the interactions between two nucleosomes. In *The Journal of Biological Chemistry* 286 (13)*: pp. 11099-11109.*

Jung-Shin Lee, Alexander S. Garrett, Kuangyu Yen, Yoh-Hei Takahashi, Deqing Hu, Jessica Jackson, Christopher Seidel, B. Franklin Pugh and Ali Shilatifard (2012). Codependency of H2B monoubiquitination and nucleosome reassembly on Chd1. In *Genes & Development* 26 (9)*: pp. 914-919.*

Nam K. Lee, Achillefs N. Kapanidis, You Wang, Xavier Michalet, Jayanta Mukhopadhyay, Richard H. Ebright and Shimon Weiss (2005). Accurate FRET measurements within single diffusing biomolecules using alternating-laser excitation. In *Biophysical Journal* 88 (4)*: pp. 2939-2953.*

John D. Leonard and Geeta J. Narlikar (2015). A nucleotide-driven switch regulates flanking DNA length sensing by a dimeric chromatin remodeler. In *Molecular Cell* 57 (5)*: pp. 850-859.*

Robert F. Levendosky, Anton Sabantsev, Sebastian Deindl and Gregory D. Bowman (2016). The Chd1 chromatin remodeler shifts hexasomes unidirectionally. In *eLife* 5. e21356, doi: 10.7554/eLife.21356.

Gu Li, Marcia Levitus, Carlos Bustamante and Jonathan Widom (2005). Rapid spontaneous accessibility of nucleosomal DNA. In *Nature Structural & Molecular Biology* 12 (1)*: pp. 46-53.

Gu Li and Jonathan Widom (2004). Nucleosomes facilitate their own invasion. In *Nature Structural & Molecular Biology* 11 (8)*: pp. 763-769.

Giuseppe Lia, Elise Praly, Helder Ferreira, Chris Stockdale, Yuk C. Tse-Dinh, David Dunlap, Vincent Croquette, David Bensimon and Tom Owen-Hughes (2006). Direct observation of DNA distortion by the RSC chromatin remodelling complex. In *Molecular Cell* 21 (3)*: pp. 417-425.

Xiaoping Liang, Shan Shan, Lu Pan, Jicheng Zhao, Anand Ranjan, Feng Wang, Zhuqiang Zhang, Yingzi Huang, Hanqiao Feng, Debbie Wei, Li Huang, Xuehui Liu, Qiang Zhong, Jizhong Lou, Guohong Li, Carl Wu and Zheng Zhou (2016). Structural basis of H2A.Z recognition by SRCAP chromatin-remodeling subunit YL1. In *Nature Structural & Molecular Biology* 23 (4)*: pp. 317-323.

Erez Lieberman-Aiden, Nynke L. van Berkum, Louise Williams, Maxim Imakaev, Tobias Ragoczy, Agnes Telling, Ido Amit, Bryan R. Lajoie, Peter J. Sabo, Michael O. Dorschner, Richard Sandstrom, Bradley Bernstein, M. A. Bender, Mark Groudine, Andreas Gnirke, John Stamatoyannopoulos, Leonid A. Mirny, Eric S. Lander and Job Dekker (2009). Comprehensive mapping of long-range interactions reveals folding principles of the human genome. In *Science* 326 (5950)*: pp. 289-293.

Corinna Lieleg, Philip Ketterer, Johannes Nuebler, Johanna Ludwigsen, Ulrich Gerland, Hendrik Dietz, Felix Mueller-Planitz and Philipp Korber (2015). Nucleosome spacing generated by ISWI and CHD1 remodelers is constant regardless of nucleosome density. In *Molecular and Cellular Biology* 35 (9)*: pp. 1588-1605.

Chia-Liang Lin, Yuriy Chaban, David M. Rees, Elizabeth A. McCormack, Lorraine Ocloo and Dale B. Wigley (2017). Functional characterization and architecture of recombinant yeast SWR1 histone exchange complex. In *Nucleic Acids Research* 45 (12)*: pp. 7249-7260.

Chih L. Liu, Tommy Kaplan, Minkyu Kim, Stephen Buratowski, Stuart L. Schreiber, Nir Friedman and Oliver J. Rando (2005). Single-nucleosome mapping of histone modifications in *S. cerevisiae*. In *PLoS Biology* 3 (10)*. e328, doi: 10.1371/journal.pbio.0030328.

Ning Liu, Craig L. Peterson and Jeffrey J. Hayes (2011). SWI/SNF- and RSC-catalyzed nucleosome mobilization requires internal DNA loop translocation within nucleosomes. In *Molecular and Cellular Biology* 31 (20)*: pp. 4165-4175.

Xiaoyu Liu, Meijing Li, Xian Xia, Xueming Li and Zhucheng Chen (2017). Mechanism of chromatin remodelling revealed by the Snf2-nucleosome structure. In *Nature* 544 (7651)*: pp. 440-445.

Yahli Lorch, Janice W. LaPointe and Roger D. Kornberg (1987). Nucleosomes inhibit the initiation of transcription but allow chain elongation with the displacement of histones. In *Cell* 49 (2)*: pp. 203-210.

Yahli Lorch, Barbara Maier-Davis and Roger D. Kornberg (2006). Chromatin remodeling by nucleosome disassembly *in vitro*. In *Proceedings of the National Academy of Sciences of the United States of America* 103 (9)*: pp. 3090-3093.

P. T. Lowary and J. Widom (1998). New DNA sequence rules for high affinity binding to histone octamer and sequence-directed nucleosome positioning. In *Journal of Molecular Biology* 276 (1)*: pp. 19-42.

Johanna Ludwigsen, Sabrina Pfennig, Ashish K. Singh, Christina Schindler, Nadine Harrer, Ignasi Forné, Martin Zacharias and Felix Mueller-Planitz (2017). Concerted regulation of ISWI by an autoinhibitory domain and the H4 N-terminal tail. In *eLife* 6. e21477, doi: 10.7554/eLife.21477.

Karolin Luger, Armin W. Mäder, Robin K. Richmond, David F. Sargent and Timothy J. Richmond (1997a). Crystal structure of the nucleosome core particle at 2.8 Å resolution. In *Nature* 389 (6648)*: pp. 251-260.

Karolin Luger, Thomas J. Rechsteiner, Andrew J. Flaus, Mary M. Waye and Timothy J. Richmond (1997b). Characterization of nucleosome core particles containing histone proteins made in bacteria. In *Journal of Molecular Biology* 272 (3)*: pp. 301-311.

Ed Luk, Anand Ranjan, Peter C. FitzGerald, Gaku Mizuguchi, Yingzi Huang, Debbie Wei and Carl Wu (2010). Stepwise histone replacement by SWR1 requires dual activation with histone H2A.Z and canonical nucleosome. In *Cell* 143 (5)*: pp. 725-736.

Kazuhiro Maeshima, Ryosuke Imai, Sachiko Tamura and Tadasu Nozaki (2014). Chromatin as dynamic 10-nm fibers. In *Chromosoma* 123 (3)*: pp. 225-237.

Ravindra D. Makde, Joseph R. England, Hemant P. Yennawar and Song Tan (2010). Structure of RCC1 chromatin factor bound to the nucleosome core particle. In *Nature* 467 (7315)*: pp. 562-566.

Zhuo Mao, Lu Pan, Weixiang Wang, Jian Sun, Shan Shan, Qiang Dong, Xiaoping Liang, Linchang Dai, Xioajun Ding, She Chen, Zhuqiang Zhang, Bing Zhu and Zheng Zhou (2014). Anp32e, a higher eukaryotic histone chaperone directs preferential recognition for H2A.Z. In *Cell Research* 24 (4)*: pp. 389-399.

Emmanuel Margeat, Achillefs N. Kapanidis, Philip Tinnefeld, You Wang, Jayanta Mukhopadhyay, Richard H. Ebright and Shimon Weiss (2006). Direct observation of abortive initiation and promoter escape within single immobilized transcription complexes. In *Biophysical Journal* 90 (4)*: pp. 1419-1431.

Francesca Mattiroli, Sudipta Bhattacharyya, Pamela N. Dyer, Alison E. White, Kathleen Sandman, Brett W. Burkhart, Kyle R. Byrne, Thomas Lee, Natalie G. Ahn, Thomas J. Santangelo, John N. Reeve and Karolin Luger (2017). Structure of histone-based chromatin in Archaea. In *Science* 357 (6351)*: pp. 609-612.

Travis N. Mavrich, Ilya P. Ioshikhes, Bryan J. Venters, Cizhong Jiang, Lynn P. Tomsho, Ji Qi, Stephan C. Schuster, Istvan Albert and B. Franklin Pugh (2008). A barrier nucleosome model for statistical positioning of nucleosomes throughout the yeast genome. In *Genome Research* 18 (7)*: pp. 1073-1083.

James D. McGhee and Gary Felsenfeld (1980). Nucleosome structure. In *Annual Review of Biochemistry* 49*: pp. 1115-1156.

Robert K. McGinty and Song Tan (2015). Nucleosome structure and function. In *Chemical Reviews* 115 (6)*: pp. 2255-2273.

Jeffrey N. McKnight, Katherine R. Jenkins, Ilana M. Nodelman, Thelma Escobar and Gregory D. Bowman (2011). Extranucleosomal DNA binding directs nucleosome sliding by Chd1. In *Molecular and Cellular Biology* 31 (23)*: pp. 4746-4759.

Shirley Mihardja, Andrew J. Spakowitz, Yongli Zhang and Carlos Bustamante (2006). Effect of force on mononucleosomal dynamics. In *Proceedings of the National Academy of Sciences of the United States of America* 103 (43)*: pp. 15871-15876.

Malcolm Moos, Jr., Nga Y. Nguyen and Teh-Yung Liu (1988). Reproducible high yield sequencing of proteins electrophoretically separated and transferred to an inert support. In *The Journal of Biological Chemistry* 263 (13)*: pp. 6005-6008.

Ashby J. Morrison, Jessica Highland, Nevan J. Krogan, Ayelet Arbel-Eden, Jack F. Greenblatt, James E. Haber and Xuetong Shen (2004). INO80 and γ-H2AX interaction links ATP-dependent chromatin remodeling to DNA damage repair. In *Cell* 119 (6)*: pp. 767-775.

Felix Mueller-Planitz, Henrike Klinker and Peter B. Becker (2013a). Nucleosome sliding mechanisms: new twists in a looped history. In *Nature Structural & Molecular Biology* 20 (9)*: pp. 1026-1032.

Felix Mueller-Planitz, Henrike Klinker, Johanna Ludwigsen and Peter B. Becker (2013b). The ATPase domain of ISWI is an autonomous nucleosome remodeling machine. In *Nature Structural & Molecular Biology* 20 (1)*: pp. 82-89.

Adam Muschielok and Jens Michaelis (2011). Application of the nano-positioning system to the analysis of fluorescence resonance energy transfer networks. In *The Journal of Physical Chemistry B* 115 (41)*: pp. 11927-11937.

Sua Myong, Michael M. Bruno, Anna M. Pyle and Taekjip Ha (2007). Spring-loaded mechanism of DNA unwinding by hepatitis C virus NS3 helicase. In *Science* 317 (5837)*: pp. 513-516.

Julia Nagy, Dina Grohmann, Alan C. Cheung, Sarah Schulz, Katherine Smollett, Finn Werner and Jens Michaelis (2015). Complete architecture of the archaeal RNA polymerase open complex from single-molecule FRET and NPS. In *Nature Communications* 6*. Article number: 6161.

Geeta J. Narlikar, Ramasubramanian Sundaramoorthy and Tom Owen-Hughes (2013). Mechanisms and functions of ATP-dependent chromatin-remodeling enzymes. In *Cell* 154 (3)*:* pp. 490-503.

Lenore Neigeborn and Marian Carlson (1984). Genes affecting the regulation of SUC2 gene expression by glucose repression in Saccharomyces cerevisiae. In *Genetics* 108 (4)*:* pp. 845-858.

Heinz Neumann, Susan M. Hancock, Ruth Buning, Andrew Routh, Lynda Chapman, Joanna Somers, Tom Owen-Hughes, John van Noort, Daniela Rhodes and Jason W. Chin (2009). A method for genetically installing site-specific acetylation in recombinant histones defines the effects of H3 K56 acetylation. In *Molecular Cell* 36 (1)*:* pp. 153-163.

Thuy T. Ngo and Taekjip Ha (2015). Nucleosomes undergo slow spontaneous gaping. In *Nucleic Acids Research* 43 (8)*:* pp. 3964-3971.

Thuy T. Ngo, Qiucen Zhang, Ruobo Zhou, Jaya G. Yodh and Taekjip Ha (2015). Asymmetric unwrapping of nucleosomes under tension directed by DNA local flexibility. In *Cell* 160 (6)*:* pp. 1135-1144.

Eyal Nir, Xavier Michalet, Kambiz M. Hamadani, Ted A. Laurence, Daniel Neuhauser, Yevgeniy Kovchegov and Shimon Weiss (2006). Shot-noise limited single-molecule FRET histograms: comparison between theory and experiments. In *The Journal of Physical Chemistry B* 110 (44)*:* pp. 22103-22124.

Ilana M. Nodelman, Franziska Bleichert, Ashok Patel, Ren Ren, Kyle C. Horvath, James M. Berger and Gregory D. Bowman (2017). Interdomain communication of the Chd1 chromatin remodeler across the DNA gyres of the nucleosome. In *Molecular Cell* 65 (3)*:* pp. 447-459. e6.

Elphège P. Nora, Job Dekker and Edith Heard (2013). Segmental folding of chromosomes: a basis for structural and regulatory chromosomal neighborhoods? In *Bioessays* 35 (9)*:* pp. 818-828.

Elphège P. Nora, Bryan R. Lajoie, Edda G. Schulz, Luca Giorgetti, Ikuhiro Okamoto, Nicolas Servant, Tristan Piolot, Nynke L. van Berkum, Johannes Meisig, John Sedat, Joost Gribnau, Emmanuel Barillot, Nils Blüthgen, Job Dekker and Edith Heard (2012). Spatial partitioning of the regulatory landscape of the X-inactivation centre. In *Nature* 485 (7398)*:* pp. 381-385.

Arnaud Obri, Khalid Ouararhni, Christophe Papin, Marie-Laure Diebold, Kiran Padmanabhan, Martin Marek, Isabelle Stoll, Ludovic Roy, Patrick T. Reilly, Tak W. Mak, Stefan Dimitrov, Christophe Romier and Ali Hamiche (2014). ANP32E is a histone chaperone that removes H2A.Z from chromatin. In *Nature* 505 (7485)*:* pp. 648-653.

Josefina Ocampo, Răzvan V. Chereji, Peter R. Eriksson and David J. Clark (2016). The ISW1 and CHD1 ATP-dependent chromatin remodelers compete to set nucleosome spacing *in vivo*. In *Nucleic Acids Research* 44 (10)*:* pp. 4625-4635.

Ada L. Olins and Donald E. Olins (1974). Spheroid chromatin units (v bodies). In *Science* 183 (4122)*:* pp. 330-332.

Donald E. Olins and Ada L. Olins (2003). Chromatin history: our view from the bridge. In *Nature Reviews Molecular Cell Biology* 4 (10)*: pp. 809-814.

Orkide Ordu, Alexandra Lusser and Nynke H. Dekker (2016). Recent insights from in vitro single-molecule studies into nucleosome structure and dynamics. In *Biophysical Reviews* 8 (Suppl 1)*: pp. 33-49.

Jason J. Otterstrom and Antoine M. van Oijen (2009). Nudging through a nucleosome. In *Science* 325 (5940)*: pp. 547-548.

P. Oudet, M. Gross-Bellard and P. Chambon (1975). Electron microscopic and biochemical evidence that chromatin structure is a repeating unit. In *Cell* 4 (4)*: pp. 281-300.

Manolis Papamichos-Chronakis and Craig L. Peterson (2008). The Ino80 chromatin-remodeling enzyme regulates replisome function and stability. In *Nature Structural & Molecular Biology* 15 (4)*: pp. 338-345.

Craig L. Peterson and Ira Herskowitz (1992). Characterization of the yeast SWI1, SWI2, and SWI3 genes, which encode a global activator of transcription. In *Cell* 68 (3)*: pp. 573-583.

Eric F. Pettersen, Thomas D. Goddard, Conrad C. Huang, Gregory S. Couch, Daniel M. Greenblatt, Elaine C. Meng and Thomas E. Ferrin (2004). UCSF Chimera – a visualization system for exploratory research and analysis. In *Journal of Computational Chemistry* 25 (13)*: pp. 1605-1612.

Evelyn Ploetz, Eitan Lerner, Florence Husada, Martin Roelfs, SangYoon Chung, Johannes Hohlbein, Shimon Weiss and Thorben Cordes (2016). Förster resonance energy transfer and protein-induced fluorescence enhancement as synergetic multi-scale molecular rulers. In *Scientific Reports* 6. Article number: 33257.

Jérôme Poli, Susan M. Gasser and Manolis Papamichos-Chronakis (2017). The INO80 remodeller in transcription, replication and repair. In *Philosophical Transactions of the Royal Society B* 372 (1731). 20160290, doi: 10.1098/rstb.2016.0290.

Jérôme Poli, Christian-Benedikt Gerhold, Alessandro Tosi, Nicole Hustedt, Andrew Seeber, Ragna Sack, Franz Herzog, Philippe Pasero, Kenji Shimada, Karl-Peter Hopfner and Susan M. Gasser (2016). Mec1, INO80, and the PAF1 complex cooperate to limit transcription replication conflicts through RNAPII removal during replication stress. In *Genes & Development* 30 (3)*: pp. 337-354.

Yupeng Qiu, Robert F. Levendosky, Srinivas Chakravarthy, Ashok Patel, Gregory D. Bowman and Sua Myong (2017). The Chd1 chromatin remodeler shifts nucleosomal DNA bidirectionally as a monomer. In *Molecular Cell* 68 (1)*: pp. 76-88.

Lisa R. Racki, Nariman Naber, Ed Pate, John Leonard, Roger Cooke and Geeta J. Narlikar (2014). The histone H4 tail regulates the conformation of the ATP-binding pocket in the SNF2h chromatin remodeling enzyme. In *Journal of Molecular Biology* 426 (10)*: pp. 2034-2044.

Lisa R. Racki, Janet G. Yang, Nariman Naber, Peretz D. Partensky, Ashley Acevedo, Thomas J. Purcell, Roger Cooke, Yifan Cheng and Geeta J. Narlikar (2009). The chromatin remodeller ACF acts as a dimeric motor to space nucleosomes. In *Nature* 462 (7276)*:* pp. 1016-1021.

Ryan M. Raisner, Paul D. Hartley, Marc D. Meneghini, Marie Z. Bao, Chih L. Liu, Stuart L. Schreiber, Oliver J. Rando and Hiten D. Madhani (2005). Histone variant H2A.Z marks the 5' ends of both active and inactive genes in euchromatin. In *Cell* 123 (2)*:* pp. 233-248.

Anand Ranjan, Gaku Mizuguchi, Peter C. FitzGerald, Debbie Wei, Feng Wang, Yingzi Huang, Ed Luk, Christopher L. Woodcock and Carl Wu (2013). Nucleosome free region dominates histone acetylation in targeting SWR1 to promoters for H2A.Z replacement. In *Cell* 154 (6)*:* pp. 1232-1245.

Anand Ranjan, Feng Wang, Gaku Mizuguchi, Debbie Wei, Yingzi Huang and Carl Wu (2015). H2A histone-fold and DNA elements in nucleosome activate SWR1-mediated H2A.Z replacement in budding yeast. In *eLife* 4. e06845, doi: 10.7554/eLife.06845.

Suhas S. Rao, Miriam H. Huntley, Neva C. Durand, Elena K. Stamenova, Ivan D. Bochkov, James T. Robinson, Adrian L. Sanborn, Ido Machol, Arina D. Omer, Eric S. Lander and Erez Lieberman Aiden (2014). A three-dimensional map of the human genome at kilobase resolution reveals principles of chromatin looping. In *Cell* 159 (7)*:* pp. 1665-1680.

Barbara P. Rattner, Timur Yusufzai and James T. Kadonaga (2009). HMGN proteins act in opposition to ATP-dependent chromatin remodeling factors to restrict nucleosome mobility. In *Molecular Cell* 34 (5)*:* pp. 620-626.

Sreerupa Ray and Anne Grove (2012). Interaction of *Saccharomyces cerevisiae* HMO2 domains with distorted DNA. In *Biochemistry* 51 (9)*:* pp. 1825-1835.

John N. Reeve (2003). Archaeal chromatin and transcription. In *Molecular Microbiology* 48 (3)*:* pp. 587-598.

Timothy J. Richmond and Curt A. Davey (2003). The structure of DNA in the nucleosome core. In *Nature* 423 (6936)*:* pp. 145-150.

Anjanabha Saha, Jacqueline Wittmeyer and Bradley R. Cairns (2005). Chromatin remodeling through directional DNA translocation from an internal nucleosomal site. In *Nature Structural & Molecular Biology* 12 (9)*:* pp. 747-755.

Thomas Schalch, Sylwia Duda, David F. Sargent and Timothy J. Richmond (2005). X-ray structure of a tetranucleosome and its implications for the chromatin fibre. In *Nature* 436 (7047)*:* pp. 138-141.

Caroline A. Schneider, Wayne S. Rasband and Kevin W. Eliceiri (2012). NIH Image to ImageJ: 25 years of image analysis. In *Nature Methods* 9 (7)*:* pp. 671-675.

Waldemar Schrimpf, Anders Barth, Jelle Hendrix and Don C. Lamb (2018). PAM: A Framework for Integrated Analysis of Imaging, Single-Molecule, and Ensemble Fluorescence Data. In *Biophysical Journal* 114 (7)*: pp. 1518-1528.*

Heidi L. Schubert, Jacqueline Wittmeyer, Margaret M. Kasten, Kaeda Hinata, David C. Rawling, Annie Héroux, Bradley R. Cairns and Christopher P. Hill (2013). Structure of an actin-related subcomplex of the SWI/SNF chromatin remodeler. In *Proceedings of the National Academy of Sciences of the United States of America* 110 (9)*: pp. 3345-3350.*

Ralf Schwanbeck, Hua Xiao and Carl Wu (2004). Spatial contacts and nucleosome step movements induced by the NURF chromatin remodeling complex. In *The Journal of Biological Chemistry* 279 (38)*: pp. 39933-39941.*

Marianne Schwarz, Kevin Schall, Eleni Kallis, Sebastian Eustermann, Mara Guariento, Manuela Moldt, Karl-Peter Hopfner and Jens Michaelis (2018). Single-molecule nucleosome remodeling by INO80 and effects of histone tails. In *FEBS Letters* 592 (3)*: pp. 318-331.*

Eran Segal, Yvonne Fondufe-Mittendorf, Lingyi Chen, AnnChristine Thåström, Yair Field, Irene K. Moore, Ji-Ping Wang and Jonathan Widom (2006). A genomic code for nucleosome positioning. In *Nature* 442 (7104)*: pp. 772-778.*

Eran Segal and Jonathan Widom (2009). What controls nucleosome positions? In *Trends in Genetics* 25 (8)*: pp. 335-343.*

Tom Sexton, Eitan Yaffe, Ephraim Kenigsberg, Frédéric Bantignies, Benjamin Leblanc, Michael Hoichman, Hugues Parrinello, Amos Tanay and Giacorno Cavalli (2012). Three-dimensional folding and functional organization principles of the Drosophila genome. In *Cell* 148 (3)*: pp. 458-472.*

Xuetong Shen, Gaku Mizuguchi, Ali Hamiche and Carl Wu (2000). A chromatin remodelling complex involved in transcription and DNA processing. In *Nature* 406 (6795)*: pp. 541-544.*

Xuetong Shen, Ryan Ranallo, Eugene Choi and Carl Wu (2003). Involvement of actin-related proteins in ATP-dependent chromatin remodeling. In *Molecular Cell* 12 (1)*: pp. 147-155.*

Kenji Shimada, Yukako Oma, Thomas Schleker, Kazuto Kugou, Kunihiro Ohta, Masahiko Harata and Susan M. Gasser (2008). Ino80 chromatin remodeling complex promotes recovery of stalled replication forks. In *Current Biology* 18 (8)*: pp. 566-575.*

Martin Sikor, Koyeli Mapa, Lena Voith von Voithenberg, Dejana Mokranjac and Don C. Lamb (2013). Real-time observation of the conformational dynamics of mitochondrial Hsp70 by spFRET. In *The EMBO Journal* 32 (11)*: pp. 1639-1649.*

Rajna Simic, Derek L. Lindstrom, Hien G. Tran, Kelli L. Roinick, Patrick J. Costa, Alexander D. Johnson, Grant A. Hartzog and Karen M. Arndt (2003). Chromatin remodeling protein Chd1 interacts with transcription elongation factors and localizes to transcribed genes. In *The EMBO Journal* 22 (8)*: pp. 1846-1856.*

Marek Simon, Justin A. North, John C. Shimko, Robert A. Forties, Michelle B. Ferdinand, Mridula Manohar, Meng Zhang, Richard Fishel, Jennifer J. Ottesen and Michael G. Poirier (2011). Histone fold modifications control nucleosome unwrapping and disassembly. In *Proceedings of the National Academy of Sciences of the United States of America* 108 (31)*: pp. 12711-12716.*

Martin R. Singleton, Mark S. Dillingham and Dale B. Wigley (2007). Structure and mechanism of helicases and nucleic acid translocases. In *Annual Review of Biochemistry* 76*: pp. 23-50.*

Kalyan K. Sinha, John D. Gross and Geeta J. Narlikar (2017). Distortion of histone octamer core promotes nucleosome mobilization by a chromatin remodeler. In *Science* 355 (6322)*.* eaaa3761, doi: 10.1126/science.aaa3761.

George Sirinakis, Cedric R. Clapier, Ying Gao, Ramya Viswanathan, Bradley R. Cairns and Yongli Zhang (2011). The RSC chromatin remodelling ATPase translocates DNA with high force and small step size. In *The EMBO Journal* 30 (12)*: pp. 2364-2372.*

Feng Song, Ping Chen, Dapeng Sun, Mingzhu Wang, Liping Dong, Dan Liang, Rui-Ming Xu, Ping Zhu and Guohong Li (2014). Cryo-EM study of the chromatin fiber reveals a double helix twisted by tetranucleosomal units. In *Science* 344 (6182)*: pp. 376-380.*

Elana M. Stennett, Monika A. Ciuba and Marcia Levitus (2014). Photophysical processes in single molecule organic fluorescent probes. In *Chemical Society Reviews* 43 (4)*: pp. 1057-1075.*

Elana M. Stennett, Monika A. Ciuba, Su Lin and Marcia Levitus (2015). Demystifying PIFE: the photophysics behind the Protein-Induced Fluorescence Enhancement phenomenon in Cy3. In *The Journal of Physical Chemistry Letters* 6 (10)*: pp. 1819-1823.*

Chris Stockdale, Andrew Flaus, Helder Ferreira and Tom Owen-Hughes (2006). Analysis of nucleosome repositioning by yeast ISWI and Chd1 chromatin remodeling complexes. In *The Journal of Biological Chemistry* 281 (24)*: pp. 16279-16288.*

Brian D. Strahl and C. David Allis (2000). The language of covalent histone modifications. In *Nature* 403 (6765)*: pp. 41-45.*

Tobias Straub (2003). Heterochromatin dynamics. In *PLoS Biology* 1 (1)*.* e14, doi: 10.1371/journal.pbio.0000014.

Lubert Stryer and Richard P. Haugland (1967). Energy transfer: a spectroscopic ruler. In *Proceedings of the National Academy of Sciences of the United States of America* 58 (2)*: pp. 719-726.*

F. William Studier and Barbara A. Moffatt (1986). Use of bacteriophage T7 RNA polymerase to direct selective high-level expression of cloned genes. In *Journal of Molecular Biology* 189 (1)*: pp. 113-130.*

F. William Studier, Alan H. Rosenberg, John J. Dunn and John W. Dubendorff (1990). Use of T7 RNA polymerase to direct expression of cloned genes. In *Methods in Enzymology* 185*: pp. 60-89.*

Ramasubramanian Sundaramoorthy, Amanda Hughes, Hassane El-Mkami, David Norman and Tom Owen-Hughes (bioRxiv: 10.1101/290874). Structure of the chromatin remodelling enzyme Chd1 bound to a ubiquitinylated nucleosome. In *bioRxiv* doi: 10.1101/290874 (2018).[2]

Ramasubramanian Sundaramoorthy, Amanda L. Hughes, Vijender Singh, Nicola Wiechens, Daniel P. Ryan, Hassane El-Mkami, Maxim Petoukhov, Dmitri I. Svergun, Barbara Treutlein, Salina Quack, Monika Fischer, Jens Michaelis, Bettina Böttcher, David G. Norman and Tom Owen-Hughes (2017). Structural reorganization of the chromatin remodeling enzyme Chd1 upon engagement with nucleosomes. In *eLife* 6. e22510, doi: 10.7554/eLife.22510.

Heather Szerlong, Kaeda Hinata, Ramya Viswanathan, Hediye Erdjument-Bromage, Paul Tempst and Bradley R. Cairns (2008). The HSA domain binds nuclear actin-related proteins to regulate chromatin-remodeling ATPases. In *Nature Structural & Molecular Biology* 15 (5)*:* pp. 469-476.

Paul B. Talbert and Steven Henikoff (2017). Histone variants on the move: substrates for chromatin dynamics. In *Nature Reviews Molecular Cell Biology* 18 (2)*:* pp. 115-126.

Song Tan and Curt A. Davey (2011). Nucleosome structural studies. In *Current Opinion in Structural Biology* 21 (1)*:* pp. 128-136.

Toma E. Tomov, Roman Tsukanov, Rula Masoud, Miran Liber, Noa Plavner and Eyal Nir (2012). Disentangling subpopulations in single-molecule FRET and ALEX experiments with photon distribution analysis. In *Biophysical Journal* 102 (5)*:* pp. 1163-1173.

Sharon E. Torigoe, Ashok Patel, Mai T. Khuong, Gregory D. Bowman and James T. Kadonaga (2013). ATP-dependent chromatin assembly is functionally distinct from chromatin remodeling. In *eLife* 2. e00863, doi: 10.7554/eLife.00863.

Alessandro Tosi (2013). Dissection of the Topology, Structure and Function of the INO80 Chromatin Remodeler. Dissertation. Ludwig-Maximilians-Universität München, Fakultät für Chemie und Pharmazie, url: http://nbn-resolving.de/urn:nbn:de:bvb:19-164074.

Alessandro Tosi, Caroline Haas, Franz Herzog, Andrea Gilmozzi, Otto Berninghausen, Charlotte Ungewickell, Christian B. Gerhold, Kristina Lakomek, Ruedi Aebersold, Roland Beckmann and Karl-Peter Hopfner (2013). Structure and subunit topology of the INO80 chromatin remodeler and its nucleosome complex. In *Cell* 154 (6)*:* pp. 1207-1219.

Katalin Tóth, Vera Böhm, Carolin Sellmann, Maria Danner, Janina Hanne, Marina Berg, Ina Barz, Alexander Gansen and Jörg Langowski (2013). Histone- and DNA sequence-dependent stability of nucleosomes studied by single-pair FRET. In *Cytometry. Part A. Journal of the International Society for Advancement of Cytometry* 83 (9)*:* pp. 839-846.

---

[2] now published in: Ramasubramanian Sundaramoorthy, Amanda L. Hughes, Hassane El-Mkami, David G. Norman, Helder Ferreira and Tom Owen-Hughes (2018). Structure of the chromatin remodelling enzyme Chd1 bound to a ubiquitinylated nucleosome. In *eLife* 7. e35720, doi: 10.7554/eLife.35720.

Michael Tramantano, Lu Sun, Christy Au, Daniel Labuz, Zhimin Liu, Mindy Chou, Chen Shen and Ed Luk (2016). Constitutive turnover of histone H2A.Z at yeast promoters requires the preinitiation complex. In *eLife* 5. e14243, doi: 10.7554/eLife.14243.

Andrew Travers (2014). Structural biology. The 30-nm fiber redux. In *Science* 344 (6182)*: pp. 370-372.*

Andrew Travers and Georgi Muskhelishvili (2005). Bacterial chromatin. In *Current Opinion in Genetics & Development* 15 (5)*: pp. 507-514.*

Andrew Travers and Georgi Muskhelishvili (2007). A common topology for bacterial and eukaryotic transcription initiation? In *EMBO Reports* 8 (2)*: pp. 147-151.*

Barbara Treutlein (2012). Mechanisms of eukaryotic gene expression on a single molecule level: From transcription initiation to nucleosome remodeling. Dissertation. Ludwig-Maximilians-Universität München, Fakultät für Chemie und Pharmazie, url: http://nbn-resolving.de/urn:nbn:de:bvb:19-154993.

Yasuo Tsunaka, Naoko Kajimura, Shin-ichi Tate and Kosuke Morikawa (2005). Alteration of the nucleosomal DNA path in the crystal structure of a human nucleosome core particle. In *Nucleic Acids Research* 33 (10)*: pp. 3424-3434.*

Maheshi Udugama, Abdellah Sabri and Blaine Bartholomew (2011). The INO80 ATP-dependent chromatin remodeling complex is a nucleosome spacing factor. In *Molecular and Cellular Biology* 31 (4)*: pp. 662-673.*

Jun Ueda, Akihito Harada, Takashi Urahama, Shinichi Machida, Kazumitsu Maehara, Masashi Hada, Yoshinori Makino, Jumpei Nogami, Naoki Horikoshi, Akihisa Osakabe, Hiroyuki Taguchi, Hiroki Tanaka, Hiroaki Tachiwana, Tatsuma Yao, Minami Yamada, Takashi Iwamoto, Ayako Isotani, Masahito Ikawa, Taro Tachibana, Yuki Okada, Hiroshi Kimura, Yasuyuki Ohkawa, Hitoshi Kurumizaka and Kazuo Yamagata (2017). Testis-Specific Histone Variant *H3t* Gene Is Essential for Entry into Spermatogenesis. In *Cell Reports* 18 (3)*: pp. 593-600.*

Andrea Újvári, Fu-Kai Hsieh, Susan W. Luse, Vasily M. Studitsky and Donal S. Luse (2008). Histone N-terminal tails interfere with nucleosome traversal by RNA polymerase II. In *The Journal of Biological Chemistry* 283 (47)*: pp. 32236-32243.*

Haico van Attikum, Olivier Fritsch, Barbara Hohn and Susan M. Gasser (2004). Recruitment of the INO80 complex by H2A phosphorylation links ATP-dependent chromatin remodeling with DNA double-strand break repair. In *Cell* 119 (6)*: pp. 777-788.*

Ivelina Vassileva, Iskra Yanakieva, Michaela Peycheva, Anastas Gospodinov and Boyka Anachkova (2014). The mammalian INO80 chromatin remodeling complex is required for replication stress recovery. In *Nucleic Acids Research* 42 (14)*: pp. 9074-9086.*

Dileep Vasudevan, Eugene Y. Chua and Curt A. Davey (2010). Crystal structures of nucleosome core particles containing the '601' strong positioning sequence. In *Journal of Molecular Biology* 403 (1)*: pp. 1-10.*

Feng Wang, Anand Ranjan, Debbie Wei and Carl Wu (2016). Comment on "A histone acetylation switch regulates H2A.Z deposition by the SWR-C remodeling enzyme". In *Science* 353 (6297)*: p. 358.

Shinya Watanabe and Craig L. Peterson (2016). Response to Comment on "A histone acetylation switch regulates H2A.Z deposition by the SWR-C remodeling enzyme". In *Science* 353 (6297)*: p. 358.

Shinya Watanabe, Marta Radman-Livaja, Oliver J. Rando and Craig L. Peterson (2013). A histone acetylation switch regulates H2A.Z deposition by the SWR-C remodeling enzyme. In *Science* 340 (6129)*: pp. 195-199.

Shinya Watanabe, Dongyan Tan, Mahadevan Lakshminarasimhan, Michael P. Washburn, Eun-Jin E. Hong, Thomas Walz and Craig L. Peterson (2015). Structural analyses of the chromatin remodelling enzymes INO80-C and SWR-C. In *Nature Communications* 6. Article number: 7108.

Cindy L. White, Robert K. Suto and Karolin Luger (2001). Structure of the yeast nucleosome core particle reveals fundamental changes in internucleosome interactions. In *The EMBO Journal* 20 (18)*: pp. 5207-5218.

Nicola Wiechens, Vijender Singh, Triantaffyllos Gkikopoulos, Pieta Schofield, Sonia Rocha and Tom Owen-Hughes (2016). The chromatin remodelling enzymes SNF2H and SNF2L position nucleosomes adjacent to CTCF and other transcription factors. In *PLoS Genetics* 12 (3). e1005940, doi: 10.1371/journal.pgen.1005940.

Dale B. Wigley and Gregory D. Bowman (2017). A glimpse into chromatin remodeling. In *Nature Structural & Molecular Biology* 24 (6)*: pp. 498-500.

Oliver Willhoft, Rohan Bythell-Douglas, Elizabeth A. McCormack and Dale B. Wigley (2016). Synergy and antagonism in regulation of recombinant human INO80 chromatin remodeling complex. In *Nucleic Acids Research* 44 (17)*: pp. 8179-8188.

Oliver Willhoft, Elizabeth A. McCormack, Ricardo J. Aramayo, Rohan Bythell-Douglas, Lorraine Ocloo, Xiaodong Zhang and Dale B. Wigley (2017). Crosstalk within a functional INO80 complex dimer regulates nucleosome sliding. In *eLife* 6. e25782, doi: 10.7554/eLife.25782.

Fred Winston and Marian Carlson (1992). Yeast SNF/SWI transcriptional activators and the SPT/SIN chromatin connection. In *Trends in Genetics* 8 (11)*: pp. 387-391.

C. L. Woodcock, L. L. Frado and J. B. Rattner (1984). The higher-order structure of chromatin: evidence for a helical ribbon arrangement. In *The Journal of Cell Biology* 99 (1)*: pp. 42-52.

Lijuan Yan, Li Wang, Yuanyuan Tian, Xian Xia and Zhucheng Chen (2016). Structure and regulation of the chromatin remodeller ISWI. In *Nature* 540 (7633)*: pp. 466-469.

Wei Yao, Sean L. Beckwith, Tina Zheng, Thomas Young, Van T. Dinh, Anand Ranjan and Ashby J. Morrison (2015). Assembly of the Arp5 (actin-related protein) subunit

involved in distinct INO80 chromatin remodeling activities. In *The Journal of Biological Chemistry* 290 (42)*: pp. 25700-25709.*

Kuangyu Yen, Vinesh Vinayachandran, Kiran Batta, R. Thomas Koerber and B. Franklin Pugh (2012). Genome-wide nucleosome specificity and directionality of chromatin remodelers. In *Cell* 149 (7)*: pp. 1461-1473.*

Kuangyu Yen, Vinesh Vinayachandran and B. Franklin Pugh (2013). SWR-C and INO80 chromatin remodelers recognize nucleosome-free regions near +1 nucleosomes. In *Cell* 154 (6)*: pp. 1246-1256.*

Guo-Cheng Yuan, Yuen-Jong Liu, Michael F. Dion, Michael D. Slack, Lani F. Wu, Steven J. Altschuler and Oliver J. Rando (2005). Genome-scale identification of nucleosome positions in *S. cerevisiae*. In *Science* 309 (5734)*: pp. 626-630.*

Helmut Zacharias (1995). Emil Heitz (1892-1965): chloroplasts, heterochromatin, and polytene chromosomes. In *Genetics* 141 (1)*: pp. 7-14.*

Yongli Zhang, Corey L. Smith, Anjanabha Saha, Stephan W. Grill, Shirley Mihardja, Steven B. Smith, Bradley R. Cairns, Craig L. Peterson and Carlos Bustamante (2006). DNA translocation and loop formation mechanism of chromatin remodeling by SWI/SNF and RSC. In *Molecular Cell* 24 (4)*: pp. 559-568.*

Zhenhai Zhang, Christian J. Wippo, Megha Wal, Elissa Ward, Philipp Korber and B. Franklin Pugh (2011). A packing mechanism for nucleosome organization reconstituted across a eukaryotic genome. In *Science* 332 (6032)*: pp. 977-980.*

Zhihui Zhang, Xuejuan Wang, Jiyu Xin, Zhenrui Ding, Sheng Liu, Qianglin Fang, Na Yang, Rui-min Xu and Gang Cai (2018). Architecture of SWI/SNF chromatin remodeling complex. In *Protein Cell*, doi: 10.1007/s13238-018-0524-9.

Coral Y. Zhou, Stephanie L. Johnson, Laura J. Lee, Adam D. Longhurst, Sean L. Beckwith, Matthew J. Johnson, Ashby J. Morrison and Geeta J. Narlikar (2018). The yeast INO80 complex operates as a tunable DNA length-sensitive switch to regulate nucleosome sliding. In *Molecular Cell* 69 (4)*: pp. 677-688.*

Coral Y. Zhou, Caitlin I. Stoddard, Jonathan B. Johnston, Michael J. Trnka, Ignacia Echeverria, Eugene Palovcak, Andrej Sali, Alma L. Burlingame, Yifan Cheng and Geeta J. Narlikar (2017). Regulation of Rvb1/Rvb2 by a domain within the INO80 chromatin remodeling complex implicates the yeast Rvbs as protein assembly chaperones. In *Cell Reports* 19 (10)*: pp. 2033-2044.*

Martin Zofall, Jim Persinger, Stefan R. Kassabov and Blaine Bartholomew (2006). Chromatin remodeling by ISW2 and SWI/SNF requires DNA translocation inside the nucleosome. In *Nature Structural & Molecular Biology* 13 (4)*: pp. 339-346.*

8. List of Figures

9. List of Tables

10. List of abbreviations

1,4-dithiothreitol	DTT
4-(2-hydroxyethyl)piperazine-1-ethanesulfonic acid	HEPES
Acceptor	A
Acousto-optical tunable filter	AOTF
Actin-related protein	Arp
Adenosine diphosphate	ADP
Adenosine triphosphate	ATP
All tailless	at
All-photon-burst-search	APBS
Alternating laser excitation-two-channel kernel-based density distribution estimator	
	ALEX-2CDE
Alternating-laser excitation	ALEX
Ammonium-Persulfat	APS
Apparent distance of donor and acceptor	r
ATPases associated with a variety of cellular activities	AAA^+ ATPases
ATP-dependent chromatin-assembly factor	ACF
Background corrected intensity	I
Base pairs	bp
Chaetomium thermophilum	Ct
Chromodomain helicase DNA binding protein 1	Chd1
Competitor DNA	crDNA
Correction factor for differences of donor and acceptor dye (γ-factor)	γ
Correction factor for direct excitation	δ
Correction factor for spectral crosstalk	α
Cryo-electron microscopy	cryoEM
Deoxyribonucleic acid	DNA
Dissociation constant	K_d
Donor	D
Drosophila melanogaster	Dm, D. melanogaster
Electron multiplying charge-coupled device	EM-CCD
Electrophoretic mobility shift assay	EMSA
Emission	em
Escherichia coli	E. coli
Ethylenediaminetetraacetic acid	EDTA
Excitation	ex
Förster radius	R_0
Förster resonance energy transfer	FRET

FRET efficiency	E
FRET-restrained positioning and screening	FPS
HAND-SANT-SLIDE	HSS
Helicase SANT associated domain	HSA-domain
Hidden-Markov-Model	HMM
High mobility group B	HMGB
High pressure liquid chromatography	HPLC
Homo sapiens	*Hs, H. sapiens*
Imitation switch	ISWI
INO eighty subunit	Ies
Isopropyl-β-D-1-thiogalactopyranoside	IPTG
Lysogeny broth	LB
Mean of a FRET efficiency distribution	E_μ
Mean of the FRET efficiency distribution	E_μ
Michaelis-Menten constant	K_M
Nano-Positioning System	NPS
Non-histone protein 10	Nhp10
Nuclear magnetic resonance	NMR
Nucleosome core particle	NCP
Nucleosome free region	NFR
Nucleotide	nt
Oligonucleotide- and oligosaccharide binding-fold	OB-fold
Optical density	OD
Orientation factor	κ^2
Polyacrylamide	PAA
Polyacrylamide gel electrophoresis	PAGE
Polyethylene glycol	PEG
Polymerase chain reaction	PCR
Probability distribution analysis	PDA
Protein induced fluorescence enhancement	PIFE
Pulsed interleaved excitation analysis with MATLAB	PAM
Pulsed interleaved excitation combined with multiparameter fluorescence detection	
	PIE-MFD
Remodels the structure of chromatin	RSC
RNA polymerase II	RNAPII
Room temperature	RT
RuvB-like	Rvb
Saccharomyces cerevisiae	*Sc, S. cerevisiae*
Schizosaccharomyces pombe	*Sp, S. pombe*

Silent information regulator	SIR
Single-molecule Förster resonance energy transfer	smFRET
Sodium dodecyl sulfate	SDS
Sodium dodecyl sulfate polyacrylamide gel electrophoresis	SDS-PAGE
Superfamily 2	SF2
Superhelical location	SHL
Switch/sucrose non-fermentable	SWI/SNF
Systematic evolution of ligands by exponential enrichment	SELEX
TATA-binding protein-associated factor 14	Taf14
Tetramethylethylendiamin	TEMED
Topologically associated domain	TAD
Total Internal Reflection Fluorescence	TIRF
Total Internal Reflection Fluorescence Microscopy	TIRFM
Transcriptional start site	TSS
Tris(hydroxymethyl)-aminomethane	Tris
Widom 601-sequence	601-seq
wild-type	wt

11. Acknowledgements

I want to thank my supervisors Prof. Dr. Karl-Peter Hopfner and Prof. Dr. Jens Michaelis for the privilege to work on this project during the past years. I am particularly thankful for the opportunity to work at the same time in both your laboratories at the Gene Center and Department of Biochemistry (LMU) and at the Institute of Biophysics (Ulm University), respectively. Thank you for trusting me with the responsibility to realize this project, which was firmly anchored in both your research groups and therefore enabled me to work with biochemical and biophysical methods in parallel. I very much appreciated your ideas and your advice that considerably contributed to shape this project, as well as your enthusiasm during discussions.

Thank you, Karl-Peter, for exciting me for structure-guided biochemistry and thank you, Jens, for constantly involving your FRET expertise when the smFRET data, as presented in this work, developed.

The biophysical work presented in this thesis was closely interconnected with the ongoing research on smFRET in the group of Prof. Dr. Jens Michaelis. I want to thank especially Monika Fischer, Eleni Kallis and Dr. Carlheinz Röcker for deliberately sharing their experience with smFRET experiments and for their recommendations on data analysis. Dr. Carlheinz Röcker assisted in Förster radius determination and Eleni Kallis assisted in data analysis of time correlated single photon counting multiparameter fluorescence detection datasets (section 5.2). Moreover, Dr. Mara Guariento helped with the realization of most nucleosome assemblies and the preparation of the respective nucleosomal DNA according to the procedures I had developed further (section 5.1.6). Her contribution was crucial as those nucleosomes were used for most smFRET experiments (section 5.2). Thank you very much for directly contributing to this work.

In the same way, special thanks are due to the "INO80 team" in the group of Prof. Dr. Karl-Peter Hopfner. Kevin Schall contributed to the understanding of the involvement of histone tails in INO80 mediated nucleosome remodeling. He provided the histone octamers for the smFRET measurements (section 5.2) and performed the electrophoretic mobility shift assays with INO80 on his own reconstituted nucleosomes (section 5.1.5, appendix 12.3). Dr. Sebastian Eustermann and Manuela Moldt provided the recombinantly expressed INO80 complex that I characterized when they established its purification (section 5.1.4). I then used their pure and functional INO80 samples for major parts of this work, especially the smFRET characterization of the

12. Appendix

12.1 Appendix related to section 4

Table 10. Supplementary table of the DNA sequences amplified to complement the DNA composition used for the nucleosome assembly as described in section 4.3.2. The 601-seq used for assembling the 220 bp 7N66 nucleosomes used for all assays is shown in Figure 12 instead. Table 10 is taken from Schwarz et al. (2018).

147 bp	ATTCATTAATGCAGCTGGCACGACAGGTTTCCCGACTGGAAA GCGGGCAGTGAGCGCAACGCAATTAATGTGAGTTAGCTCACT CATTAGGCACCCCAGGCTTTACACTTTATGCTTCCGGCTCGTA TGTTGTGTGGAATTGTGAGC	crDNA PCR product
200 bp	GGCCGCCCTGGAGAATCCCGGTGCCGAGGCCGCTCAATTGGT CGTAGCAAGCTCTAGCACCGCTTAAACGCACGTACGCGCTGT CCCCCGCGTTTTAACCGCCAAGGGGATTACTCCCTAGTCTCCA GGCACGTGTCAGATATATACATCCTGTGCATGTGTTGAACAGC GACTCGGGTTATGTGATGGACCCTATACGC	200bp-601 NotI digestion product

Table 11. Supplementary table of the protein sequences of wild-type and all tailless histones. Histone purification is described in section 4.2.2. The globular domains are highlighted in grey. All tailless constructs are from Kevin Schall, Gene Center and Department of Biochemistry, LMU Munich. Table 11 is taken from Schwarz et al. (2018).

| *hs*H2A	MSGRGKQGGKARAKAKTRSSRAGLQFPVGRVHRLLRKGNYAERVGAGAPVY LAAVLEYLTAEILELAGNAARDNKKTRIIPRHLQLAIRNDEELNKLLGKVTIAQ GGVLPNIQAVLLPKKTESHHKAKGK
*hs*H2B	MPEPAKSAPAPKKGSKKAVTKAQKKDGKKRKRSRKESYSVYVYKVLKQVHP DTGISSKAMGIMNSFVNDIFERIAGEASRLAHYNKRSTITSREIQTAVRLLLPGE LAKHAVSEGTKAVTKYTSSK
*hs*H3.2	MARTKQTARKSTGGKAPRKQLATKAARKSAPATGGVKKPHRYRPGTVALREI RRYQKSTELLIRKLPFQRLVREIAQDFKTDLRFQSSAVMALQEASEAYLVGLFE DTNLCAIHAKRVTIMPKDIQLARRIRGERA
*hs*H4	MSGRGKGGKGLGKGGAKRHRKVLRDNIQGITKPAIRRLARRGGVKRISGLIYE ETRGVLKVFLENVIRDAVTYTEHAKRKTVTAMDVVYALKRQGRTLYGFGG

12.2 Appendix related to section 5.1
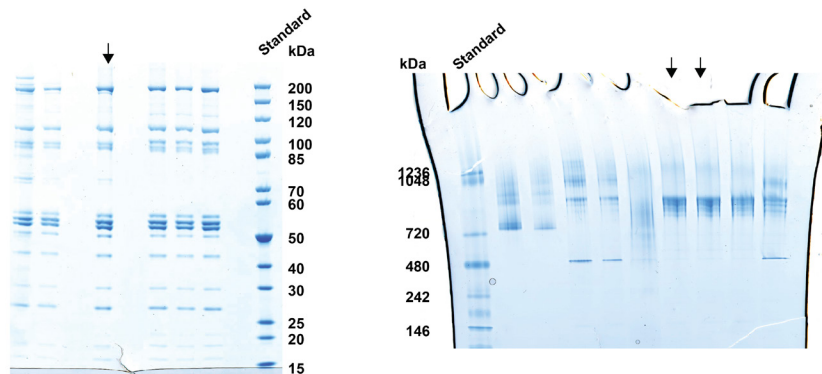
Figure 23. Supplementary figure of uncropped gels from Figure 4.

Left panel: uncropped SDS-PAGE as in Figure 4 b. Right panel: uncropped native PAGE as in Figure 4 d. Lanes shown in Figure 4 b or d are indicated by an arrow.
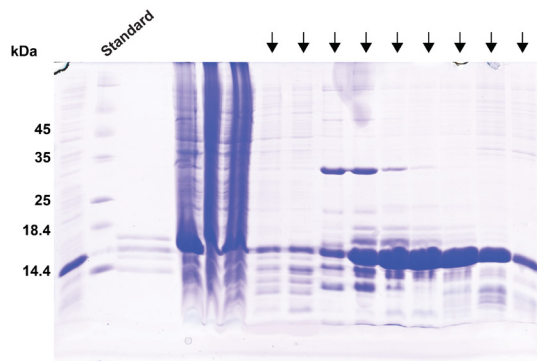

Figure 24. Supplementary figure of an uncropped gel from Figure 5.

Uncropped SDS-PAGE as in Figure 5 c. Lanes shown in Figure 5 c are indicated by an arrow.
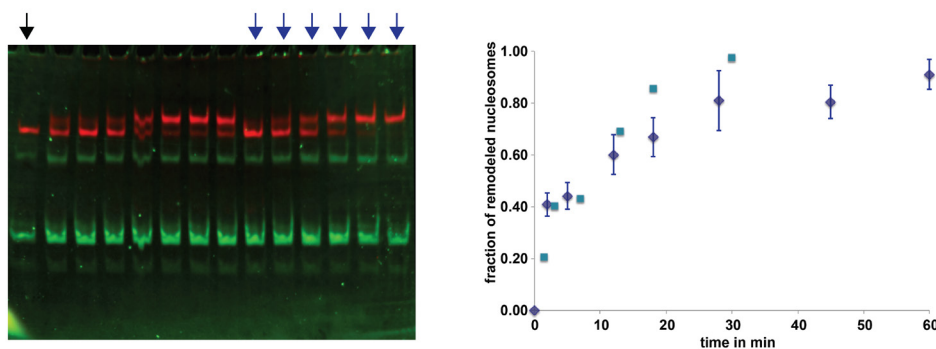

Figure 25. Supplementary figure on INO80 nucleosome sliding related to Figure 6 and Figure 8.

Left panel: Uncropped native PAGE of 7N66 nucleosome remodeling by INO80 in the presence of competitor DNA (147 bp crDNA) in false colors (fluorescence readout). Lanes shown in Figure 6 d, e are indicated by an arrow. Right Panel: Direct comparison of the quantification of the fraction of remodeled nucleosomes as shown in Figure 6 d, e (in the presence of an INO80 specific nanobody, light blue) compared to the quantification of remodeling over time shown in Figure 8 (dark blue, with error bars). Minor deviations apparent in this direct comparison may partly reflect the systematic differences in quantification when different fluorescence readout equipment has been used (section 4.1.4; Typhoon scanner, Figure 8, vs. ChemiDocMP system, Figure 6) or are due to different amounts of crDNA in the respective nucleosome preparation.
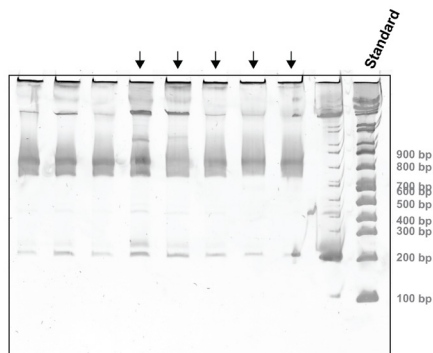
Figure 26. Supplementary figure of an uncropped gel from Figure 10.

Uncropped native PAGE after SybrGold staining (atLF construct) as shown in Figure 10 b. Lanes shown in Figure 10 b are indicated by an arrow.
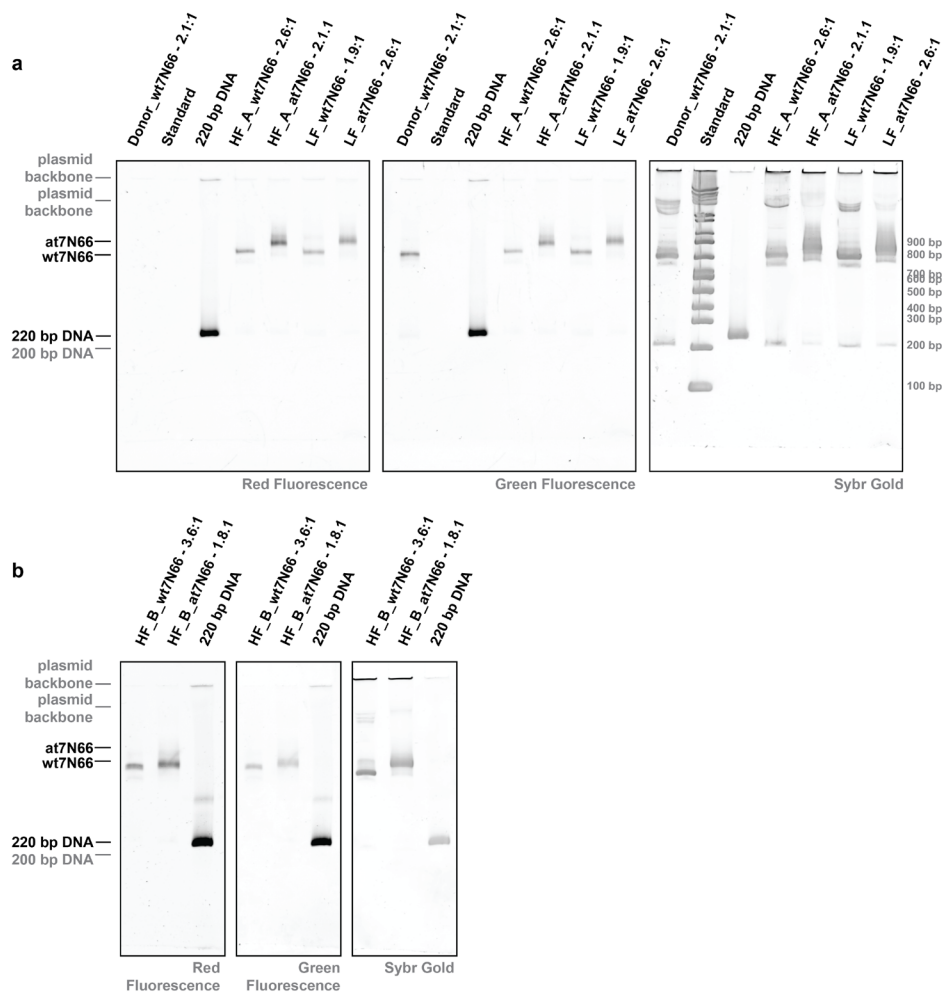
Figure 27. Supplementary figure of assembled nucleosomes for smFRET experiments; related to Figure 10.

Native PAGE (6%) of independent nucleosome assemblies for each of the six nucleosome constructs wtHF_A, atHF_A, wtLF, atLF, wtDonor in (a) and wtHF_B, atHF_B (b) used for smFRET measurements or Förster radius determination in case of wtDonor; separate single channel fluorescence readouts are shown (left and middle panel, respectively). Image of the same gel after SybrGold staining in the right panel.

Fluorescence imaging: ChemiDocMP. Annotation as in Figure 10. Dr. Mara Guariento, Institute of Biophysics, Ulm University, helped with the realization of most nucleosome assemblies presented here.

Figure 28. Supplementary figure comparing end-positioned and repositioned all tailless nucleosome constructs, related to Figure 11.

(a) Native PAGE (fluorescence readouts for the acceptor fluorophore, red, or for the donor fluorophore, green) of atLF compared to the repositio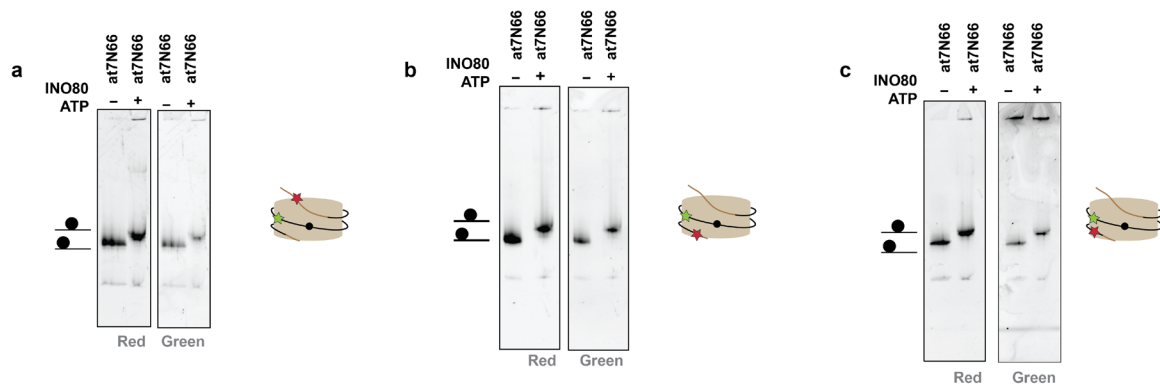ned atLF nucleosome. (b) atHF_A (educt) compared to the repositioned at_HFA nucleosome (product); representation as in (a). (c) atHF_B (educt) compared to the repositioned atHF_B nucleosome (product); representation as in (a). Figure 28 is adapted from Schwarz et al. (2018).

12.3 Appendix related to section 5.2
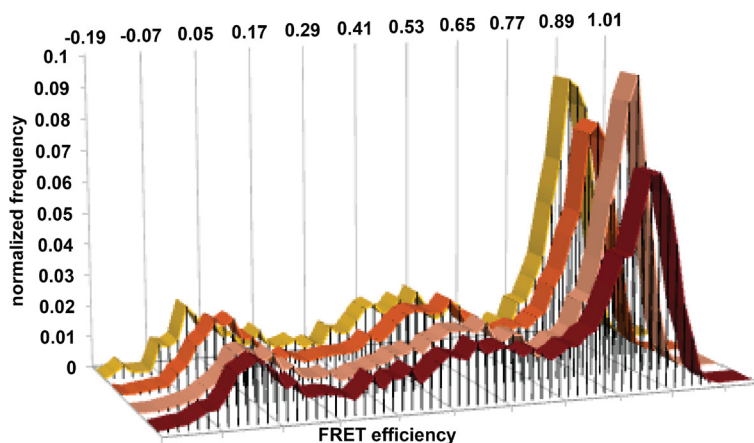
Figure 29. Supplementary figure on the confocal spectroscopy based assessment of wtLF nucleosome remodeling related to Figure 13.

FRET efficiency histogram of wtLF after applying the standard repositioning protocol (dark red histogram, same as in Figure 13 e) or after nucleosome remodeling with more stringent conditions. These are 200 nM INO80 (after 40 min incubation, light red histogram) or 180 nM INO80 (after 70 min incubation, orange histogram, and after 150 min incubation, yellow histogram), protocol in 4.6.2. The high FRET efficiency population that characterizes INO80 nucleosome sliding is comparable in these conditions.

Table 12. Supplementary table of Gaussian fit results for FRET efficiency histograms in Figure 13.
Mean FRET efficiencies highlighted in blue have been converted to the mean distance of donor and acceptor dye positions as described in section 4.7. *A*: area fraction, *E*: mean FRET efficiency, *σ*: standard deviation.

fit results	A_1	E_1	σ_1	A_2	E_2	σ_2	A_3	E_3	σ_3	construct
blue, TIRFM	1.00	0.48	0.06							wtLF
red, TIRFM	0.45	0.50	0.20	0.52	0.85	0.07	0.04	0.09	0.02	wtLF
blue, CS	0.21	0.22	0.19	0.69	0.50	0.08	0.09	0.74	0.15	wtLF
red, CS	0.13	0.01	0.06	0.46	0.54	0.23	0.41	0.86	0.06	wtLF
blue, TIRFM	0.95	0.80	0.04	0.05	0.09	0.02				wtHF_A
red, TIRFM	0.71	0.75	0.10	0.29	0.11	0.05				wtHF_A
blue, CS	0.06	0.06	0.12	0.34	0.74	0.12	0.60	0.81	0.05	wtHF_A
red, CS	0.63	0.10	0.09	0.08	0.39	0.12	0.29	0.69	0.11	wtHF_A
blue, TIRFM	0.47	0.96	0.03	0.23	0.09	0.03	0.30	0.89	0.13	wtHF_B
red, TIRFM	0.64	0.68	0.09	0.29	0.13	0.05	0.06	0.97	0.02	wtHF_B
blue, CS	0.21	0.05	0.08	0.45	0.82	0.10	0.34	0.93	0.04	wtHF_B
red, CS	0.07	-0.02	0.04	0.81	0.12	0.10	0.12	0.62	0.19	wtHF_B
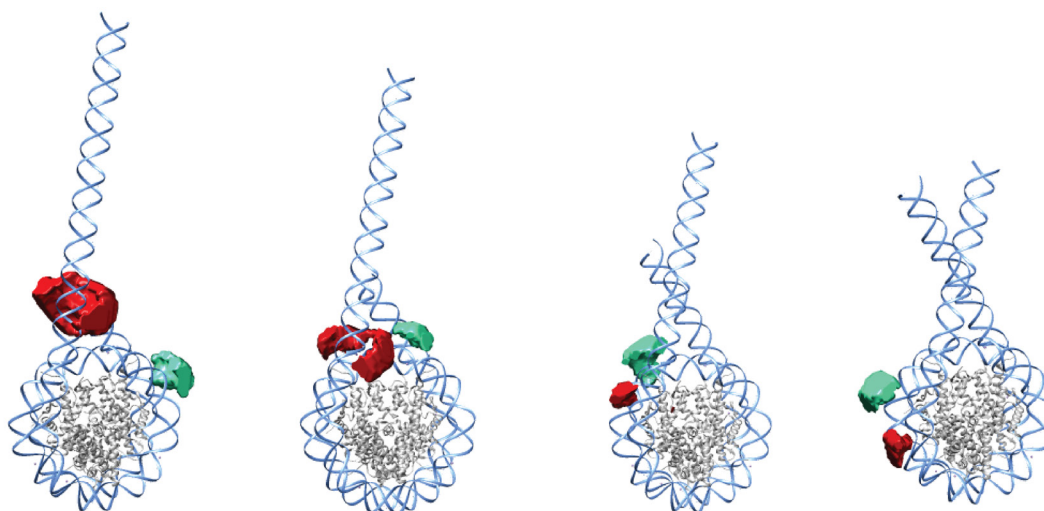
Figure 30. Supplementary figure showing the model for the 7N66 nucleosome (educt) and successive repositioned states by 10 bp (17N56, 27N46, 37N36) with accessible dye volumes for the LF construct.
The NCP structure is taken from the protein data bank (3LZ0, Vasudevan et al. (2010)). The DNA overhang has been modeled as described in section 4.8.1. The octamer moiety is depicted in grey and the DNA is depicted in light blue. The accessible volume of the acceptor is shown in red and the accessible volume of the donor is shown in green. The accessible dye volumes have been calculated with the Nano-positioning System (NPS) software developed by Muschielok and Michaelis (2011); the improved software used here is described in Dörfler et al. (2017) and Eilert et al. (2017). Parameters are listed in section 4.8.1. The modeled accessible volumes are priors, that is, they do not include experimental data.

Table 13. Supplementary table of Gaussian fit results for FRET efficiency histograms in Figure 15.
Mean FRET efficiencies highlighted in blue have been converted to the mean distance of donor and acceptor dye positions as described in section 4.7. *A*: area fraction, *E*: mean FRET efficiency, *σ*: standard deviation.

fit results	A_1	E_1	σ_1	A_2	E_2	σ_2	A_3	E_3	σ_3	
dark green, CS	0.17	0.16	0.14	0.76	0.50	0.11	0.07	0.85	0.10	wtLF
light green, CS	0.15	0.12	0.12	0.04	0.86	0.09	0.80	0.49	0.12	wtLF
dark green, TIRFM	1.00	0.45	0.09							wtLF
brown, TIRFM	0.55	0.43	0.09	0.45	0.85	0.05				wtLF
dark green, TIRFM	0.05	0.10	0.02	0.95	0.79	0.05				wtHF_A
brown, TIRFM	0.73	0.77	0.09	0.27	0.11	0.05				wtHF_A

Table 14. Supplementary table of Gaussian fit results for FRET efficiency histograms in Figure 16.
Mean FRET efficiencies highlighted in blue have been converted to the mean distance of donor and acceptor dye positions as described in section 4.7. *A*: area fraction, *E*: mean FRET efficiency, *σ*: standard deviation.

fit results	A_1	E_1	σ_1	A_2	E_2	σ_2	A_3	E_3	σ_3	
dark green, CS	0.28	0.09	0.08	0.22	0.29	0.09	0.51	0.52	0.15	atLF
light green, CS	0.17	0.57	0.07	0.68	0.40	0.22	0.15	0.08	0.08	atLF
dark green, TIRFM	0.57	0.48	0.10	0.30	0.22	0.09	0.13	0.09	0.03	atLF
brown, TIRFM	0.50	0.40	0.21	0.39	0.87	0.06	0.11	0.11	0.04	atLF
blue, CS	0.24	0.45	0.34	0.15	0.70	0.08	0.61	0.81	0.07	atHF_A
light green, CS	0.12	0.58	0.08	0.71	0.79	0.08	0.17	0.28	0.28	atHF_A
dark green, TIRFM	0.90	0.75	0.07	0.10	0.10	0.04				atHF_A
brown, TIRFM	0.33	0.77	0.07	0.46	0.64	0.15	0.21	0.12	0.05	atHF_A

Table 15. Supplementary table of Gaussian fit results for FRET efficiency histograms in Figure 17.
Mean FRET efficiencies highlighted in blue have been converted to the mean distance of donor and acceptor dye positions as described in section 4.7. *A*: area fraction, *E*: mean FRET efficiency, *σ*: standard deviation.

fit results	A_1	E_1	σ_1	A_2	E_2	σ_2	A_3	E_3	σ_3	
blue, TIRFM	1.00	0.37	0.07							atLF
red, TIRFM	0.46	0.48	0.28	0.39	0.87	0.06	0.15	0.11	0.04	atLF
blue, CS	0.15	0.04	0.09	0.80	0.35	0.11	0.05	0.80	0.12	atLF
red, CS	0.14	0.04	0.09	0.42	0.62	0.19	0.44	0.85	0.05	atLF
blue, TIRFM	0.93	0.81	0.04	0.07	0.09	0.02				atHF_A
red, TIRFM	0.42	0.57	0.06	0.31	0.11	0.04	0.27	0.77	0.07	atHF_A
blue, CS	0.08	0.05	0.10	0.29	0.63	0.16	0.63	0.78	0.08	atHF_A
red, CS	0.73	0.08	0.07	0.18	0.21	0.28	0.09	0.75	0.11	atHF_A
blue, CS	0.27	0.03	0.06	0.29	0.66	0.24	0.45	0.93	0.06	atHF_B
red, CS	0.80	0.06	0.07	0.19	0.27	0.32	0.01	0.91	0.05	atHF_B

Table 16. Supplementary table of Gaussian fit results for FRET efficiency histograms in Figure 21.
A: area fraction, *E*: mean FRET efficiency, *σ*: standard deviation.

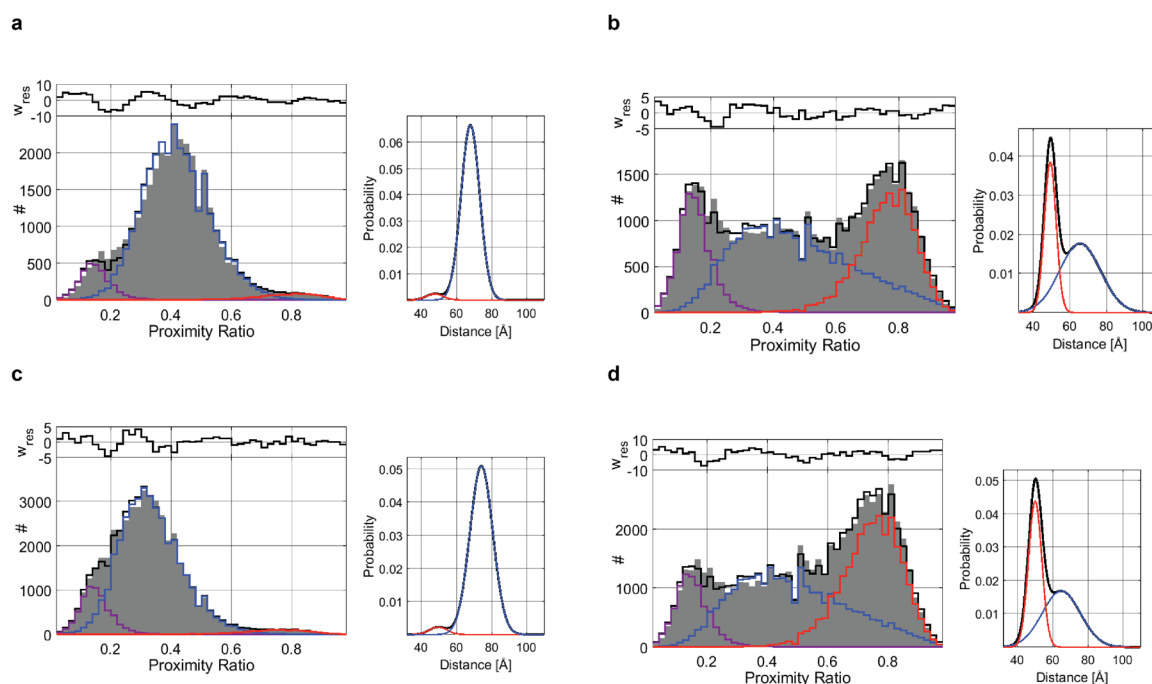| fit results	A_1	E_1	σ_1	A_2	E_2	σ_2	A_3	E_3	σ_3	
a	0.42	0.84	0.07	0.14	0.09	0.02	0.44	0.39	0.14	wtLF
b	0.64	0.86	0.03	0.28	0.55	0.29	0.08	0.08	0.03	wtLF
c	0.31	0.79	0.12	0.16	0.08	0.03	0.53	0.31	0.08	wtLF

Figure 31. Supplementary figure for the probability distribution analysis fits of the confocal spectroscopy data (wtLF and atLF) presented in Figure 13 and in Figure 17.
(a) PDA fit for wtLF (data from Figure 13 e, blue histogram). (b) PDA fit for wtLF after remodeling with INO80 (data from Figure 13 e, dark red histogram). (c) PDA fit for atLF (data from Figure 17 c, blue histogram). (d) PDA fit for atLF after remodeling with INO80 (data from Figure 17 c, dark red histogram). Fits have been performed by Eleni Kallis, Institute of Biophysics, Ulm University.
Figure 31 is taken from Schwarz et al. (2018).

Table 17. Supplementary table of fit results of probability distribution analysis as depicted in Figure 31.
CS denotes confocal spectroscopy. *A*: area fraction, *R*: mean inter-dye distance, *σ*: standard deviation.

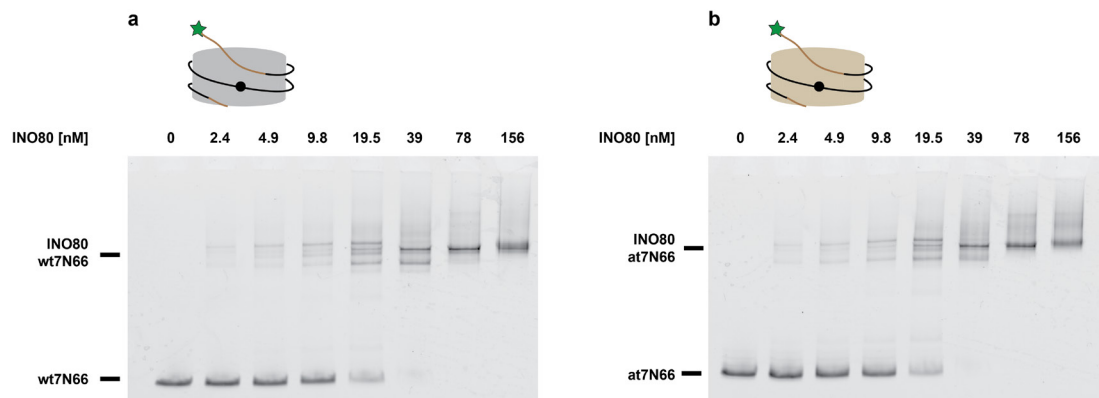| fit results	A_1	R_1 [Å]	σ_1 [Å]	A_2	R_2 [Å]	σ_2 [Å]	A_3	R_3 [Å]	σ_3 [Å]	construct
a, CS	0.09	241	7	0.88	68	5	0.03	48	5	wtLF
b, CS	0.18	241	7	0.5	66	11	0.32	49	3	wtLF
c, CS	0.14	241	7	0.84	74	7	0.03	50	5	atLF
d, CS	0.13	241	7	0.46	65	11	0.42	50	4	atLF

Figure 32. Supplementary figure showing electrophoretic mobility shift assays on (a) wild-type and (b) all tailless 7N66 nucleosomes.

EMSAs have been performed as technical triplicates by Kevin Schall, Gene Center and Department of Biochemistry, LMU Munich. The quantification is shown in Figure 9. Figure 32 is adapted from Schwarz et al. (2018).
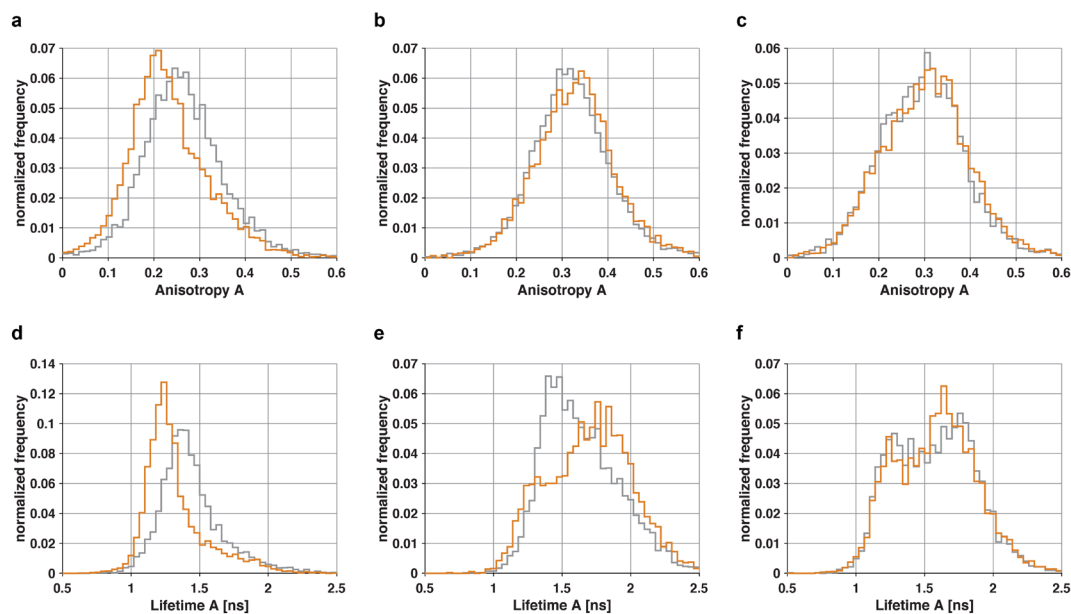

Figure 33. Supplementary figure showing the anisotropy and lifetime histograms of the acceptor dye as depicted in Figure 18, as a direct comparison between wild-type (grey) and all tailless (brown) nucleosomes.

(a, b, c) Anisotropy histograms of nucleosomes (a), of nucleosomes in the presence of 156 nM INO80 and 2 mM ADP (b) and of nucleosomes after remodeling by INO80 (c). (d, e, f) Lifetime histograms of nucleosomes (d), of nucleosomes in the presence of 156 nM INO80 and 2 mM ADP (e) and of nucleosomes after remodeling by INO80 (f).

12.4 Supplementary references

The following references have been cited in the appendix.

Thilo Dörfler, Tobias Eilert, Carlheinz Röcker, Julia Nagy and Jens Michaelis (2017). Structural Information from Single-molecule FRET Experiments Using the Fast Nano-positioning System. In *Journal of Visualized Experiments* 120. e54782, doi: 10.3791/54782.

Tobias Eilert, Maximilian Beckers, Florian Drechsler and Jens Michaelis (2017). Fast-NPS-A Markov Chain Monte Carlo-based analysis tool to obtain structural information from single-molecule FRET measurements. In *Computer Physics Communications* 219 pp. 377-389.

Adam Muschielok and Jens Michaelis (2011). Application of the nano-positioning system to the analysis of fluorescence resonance energy transfer networks. In *The Journal of Physical Chemistry B* 115 (41)*: pp. 11927-11937.

Marianne Schwarz, Kevin Schall, Eleni Kallis, Sebastian Eustermann, Mara Guariento, Manuela Moldt, Karl-Peter Hopfner and Jens Michaelis (2018). Single-molecule nucleosome remodeling by INO80 and effects of histone tails. In *FEBS Letters* 592 (3)*: pp. 318-331.

Dileep Vasudevan, Eugene Y. Chua and Curt A. Davey (2010). Crystal structures of nucleosome core particles containing the '601' strong positioning sequence. In *Journal of Molecular Biology* 403 (1)*: pp. 1-10.